NASA/CR—2005-213963

Computational Simulation of Damage Propagation in Three-Dimensional Woven Composites

Dade Huang and Levon Minnetyan
Clarkson University, Potsdam, New York

October 2005

The NASA STI Program Office . . . in Profile

Since its founding, NASA has been dedicated to the advancement of aeronautics and space science. The NASA Scientific and Technical Information (STI) Program Office plays a key part in helping NASA maintain this important role.

The NASA STI Program Office is operated by Langley Research Center, the Lead Center for NASA's scientific and technical information. The NASA STI Program Office provides access to the NASA STI Database, the largest collection of aeronautical and space science STI in the world. The Program Office is also NASA's institutional mechanism for disseminating the results of its research and development activities. These results are published by NASA in the NASA STI Report Series, which includes the following report types:

- TECHNICAL PUBLICATION. Reports of completed research or a major significant phase of research that present the results of NASA programs and include extensive data or theoretical analysis. Includes compilations of significant scientific and technical data and information deemed to be of continuing reference value. NASA's counterpart of peer-reviewed formal professional papers but has less stringent limitations on manuscript length and extent of graphic presentations.

- TECHNICAL MEMORANDUM. Scientific and technical findings that are preliminary or of specialized interest, e.g., quick release reports, working papers, and bibliographies that contain minimal annotation. Does not contain extensive analysis.

- CONTRACTOR REPORT. Scientific and technical findings by NASA-sponsored contractors and grantees.

- CONFERENCE PUBLICATION. Collected papers from scientific and technical conferences, symposia, seminars, or other meetings sponsored or cosponsored by NASA.

- SPECIAL PUBLICATION. Scientific, technical, or historical information from NASA programs, projects, and missions, often concerned with subjects having substantial public interest.

- TECHNICAL TRANSLATION. English-language translations of foreign scientific and technical material pertinent to NASA's mission.

Specialized services that complement the STI Program Office's diverse offerings include creating custom thesauri, building customized databases, organizing and publishing research results . . . even providing videos.

For more information about the NASA STI Program Office, see the following:

- Access the NASA STI Program Home Page at ***http://www.sti.nasa.gov***

- E-mail your question via the Internet to help@sti.nasa.gov

- Fax your question to the NASA Access Help Desk at 301–621–0134

- Telephone the NASA Access Help Desk at 301–621–0390

- Write to:
  NASA Access Help Desk
  NASA Center for AeroSpace Information
  7121 Standard Drive
  Hanover, MD 21076

NASA/CR—2005-213963

Computational Simulation of Damage Propagation in Three-Dimensional Woven Composites

Dade Huang and Levon Minnetyan
Clarkson University, Potsdam, New York

Prepared under Grant NAG3–1101

National Aeronautics and
Space Administration

Glenn Research Center

October 2005

This work was sponsored by the Low Emissions Alternative Power Project of the Vehicle Systems Program at the NASA Glenn Research Center.

Available from

NASA Center for Aerospace Information
7121 Standard Drive
Hanover, MD 21076

National Technical Information Service
5285 Port Royal Road
Springfield, VA 22100

Available electronically at http://gltrs.grc.nasa.gov

CONTENTS

ABSTRACT

Three-dimensional (3D) woven composites have demonstrated multi-directional properties and improved transverse strength, impact resistance and shear characteristics. The objective of this research is to develop a new model for predicting the elastic constants, hygrothermal effects, thermomechanical response, and stress limits of 3D woven composites; and to develop a computational tool to facilitate the evaluation of 3D woven composite structures with regard to damage tolerance and durability. Fiber orientations of weave and braid patterns are defined with reference to composite structural coordinates. Orthotropic ply properties and stress limits computed via micromechanics are transformed to composite structural coordinates and integrated to obtain the 3D properties. The various stages of degradation, from damage initiation to collapse of structures, in the 3D woven structures are simulated for the first time. Three dimensional woven composite specimens with various woven patterns under different loading conditions, such as tension, compression, bending, and shear are simulated in the validation process of this research. Damage initiation, growth, accumulation, and propagation to fracture are included in these simulations.

Chapter 1

Introduction

1.1 Three Dimensional Composites

Three-dimensional composites are reinforced with three dimensional textile preforms which are fully integrated continuous-fiber assemblies with multi-axial in-plane and out-of-plane fiber orientations. These composites exhibit several distinct advantages which are not realized in traditional laminates. First, because of the out-of-plane orientation of some fibers, three-dimensional composites provide enhanced stiffness and strength in the thickness direction. Second, the fully integrated nature of fiber arrangement in three-dimensional preforms eliminates the inter-laminar surfaces characteristic of laminated composites. Third, the technology of textile preforming provides the unique opportunity of near-net-shape design and manufacturing of composite components and, hence, minimizes the need for cutting and joining the parts. The potential of reducing manufacturing costs for special applications is high.

Three-dimensional textile preforms can be categorized according to their manufacturing technique. These include braiding, weaving, knitting and stitching.

Braiding preforms are formed with three basic techniques, namely two-step, four-step and multi-step braiding. In the case of two step braiding (Florentine 1992), the axial yarns are stationary and the braider yarns move among the axial yarns. In four-step braiding, all yarn carriers change their positions in the braiding process and do not maintain a straight configuration. Multi-step braiding (Kostar and Chou 1994) is an extension to the four-step braiding. By allowing for both individual controls of a given track/column and the insertion of axial yarns, the range of attainable braid architecture is greatly broadened in multi-step braiding.

In woven preforms, there are two major categories. The first is the angle-interlock multi-layer weaving technique which requires interlacing the yarns in three dimensions. The warp yarn in this three-dimensional construction penetrates several weft layers in the thickness direction, and therefore the preform structure is highly integrated. The second is the orthogonal wovens, for which the yarns assume three mutually perpendicular orientations in either a Cartesian coordinate system or a cylindrical coordinate system. The yarns in the Cartesian weave are not wavy, and as a result, matrix rich regions often appear in these composites.

The process of stitching is mainly based upon an existing technology for converting two-dimensional preforms to three-dimensional ones. This process is relatively simple. The basic needs include a sewing machine, needle and stitching thread. Major concerns of the stitching operation include depth of penetration of the stitching yarns and, hence, the thickness of two-dimensional preforms that can be stitch-bonded, as well as the degree of sacrifice of the in-plane properties due to the damage to in-plane yarns.

Three-dimensional knitted fabrics can be produced by either a weft knitting or warp knitting process. The technique of knitting is particularly desirable for producing preforms with complex shapes because the variability of the geometric forms is almost unlimited. The large extensibility and conformability of the preforms enable them to be designed and manufactured for reinforcing composites subject to complex loading conditions. The versatility of knitted preforms offers a new dimension in textile structural composite technology.

Even though three-dimensional (3-D) composites have attracted much interest due to their unique mechanical properties, such as enhanced transverse moduli and strength, and improved shear resistance and impact damage tolerance, the actual use of the 3-D composite material in engineering design poses many problems. The main problem comes from the complex geometry of 3-D composites. The fiber geometry is so complex that the geometric modeling itself is very difficult, much less accurate stress distributions. For example, in plain weave textile composites, there are many fiber tows (warp and fill) interlacing each other. There can be nesting of the fiber tows of one layer in adjacent layers. The existence of matrix pockets adds to the complexity of the geometry. In fact, many research papers have been devoted just to modeling the geometry of 3-D composites (Pierce 1987, Pastore and Ko 1990, Du and Chou 1991).

The inherent geometric complexity of 3-D composites makes a detailed stress analysis very formidable. Most analytical and numerical techniques are merely used to predict the stiffness properties of 3-D composites. There are few models that have been developed for detailed stress analysis (Woo and Whitcomb 1994, Yoshino et al 1981, Kriz 1989, Pastore et al 1993) and the strength prediction of textile composites. To date, there is no information in the existing literature on simulating the entire procedure of damage propagation of 3-D composites. Some of the earlier works for predicting elastic constants, damage propagation, and strength of woven and braided composites are highlighted below.

1.2 Stiffness Properties of Three Dimensional Composites

The stiffness averaging method which was developed by Kregers et al (1978, 1979) is widely used to predict the deformation characteristics of a composite with three-dimensional reinforcement from the known mechanical properties of its components. The basic idea behind stiffness averaging method is to treat the fibers and matrix as a set of composite rods having various spatial orientations. The local stiffness tensor for each of these rods is calculated and rotated in space to fit the global composite axes. The global stiffness tensors of all the composite rods are then superimposed with respect to their relative volume fraction to form the composite stiffness tensor. This approach is also called the Fabric Geometry Model (Pastore and Gowayed, 1994) or Orientation Averaging Method. The stiffness of the individual directions of reinforcement are averaged in accordance with the following expressions:

$$A_{jklm} = \frac{1}{V} \sum_{i=1}^{N} V_i \, A_{jklm}^{(i)}$$

$$V = \sum_{i=1}^{N} V_i$$

Where A_{jklm} are the components of the stiffness tensor of the three-dimensionally reinforced composite: V_i is the calculated volume of the *i-th* direction of reinforcement; N is the number of discrete directions of reinforcement, $N \geq 1$.

Ko (1986) presented a geometric model for three-dimensional braid composite using the concept of average cosine to evaluate the tensile strength and modulus of a three-dimensional braid composite. The three-dimensional braid composite was divided into a series of unit cells and the yarn segment was idealized as straight in a unit cell as shown in Figure 1.1.

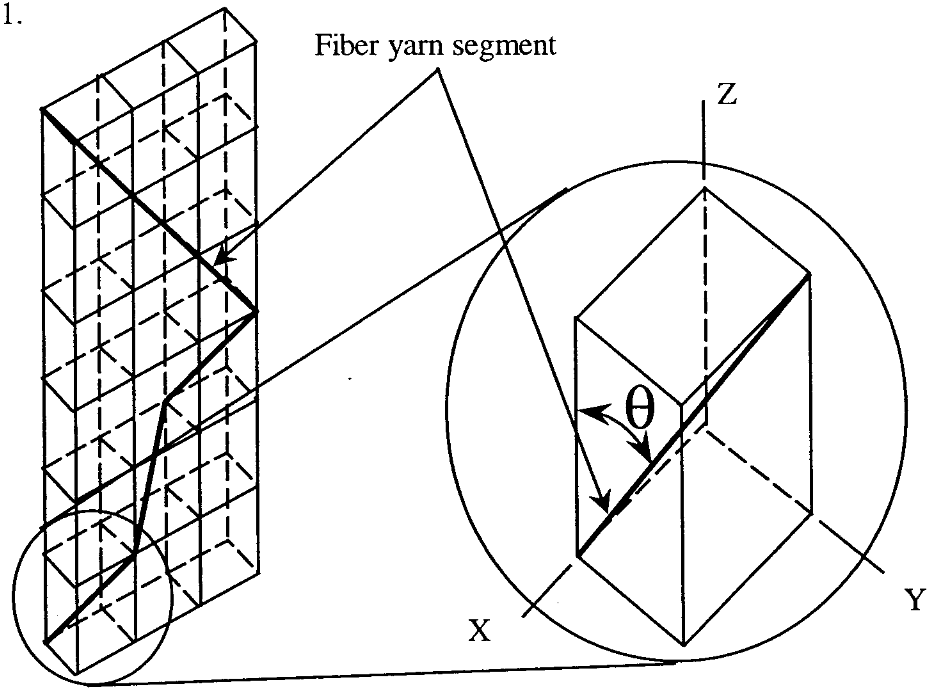

Figure 1.1 Idealized fiber yarn segment in unit cell of 3D braid composites

To obtain an average representation of yarn orientation, the average cosine of yarn angles was used:

$$\cos\bar{\theta} = ND_y / D_f$$

Where N = number of yarns in the fabric, D_y = yarn linear density, D_f = fabric linear density. The predicted composite tensile strength and modulus in the longitudinal direction based on the average angle of yarn, in general, were within 20% of the experimental results.

To facilitate the description of complex geometry of 3-D composites, the concept of unit cell structure has been used by many investigators. A unit cell is a representative volume element small enough to reflect the structural details, yet large enough to represent the overall response of the composite. When unit cells are repeated, they will reconstruct the entire structural geometry.

Yang et al. (1986) presented a "Fiber Inclination Model" to predict the elastic properties of 3-D textile structural composites. The unit cell of a composite was treated as an assemblage of inclined unidirectional laminate. For a 3-D braided composite, the orientation of the yarns in the braided preform is controlled by the three orthogonal motions. Therefore, the resultant preform is a continuous interwoven structure composed of yarns oriented in various directions. An idealized unit cell structure is constructed based upon the fiber bundles oriented in four body diagonal direction in a rectangular parallelepiped which is shown schematically in figure 1.2, the unit cell is considered as an assemblage of four inclined unidirectional laminae, and each unidirectional laminae is characterized by a unique fiber orientation and all the laminae have the same thickness and fiber volume fraction of each lamina is assumed to be the same as that of the composite. The laminate approximation of the unit cell structure is shown schematically in figure 1.3. The properties of each lamina can be obtained from the classical laminated plate theory, the composite properties can be obtained from these lamina properties based on the stiffness averaging approach.

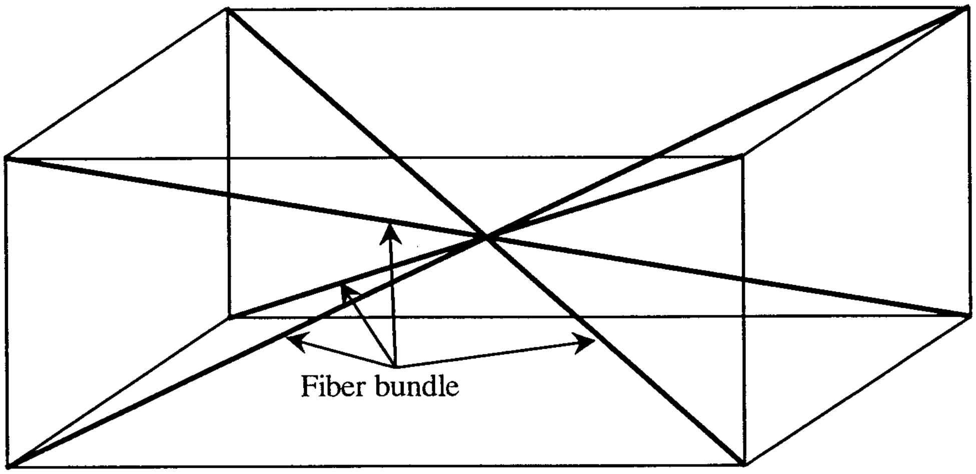

Figure 1.2 The unit cell structure of a 3-D braided structural composites with yarns moving in three orthogonal directions

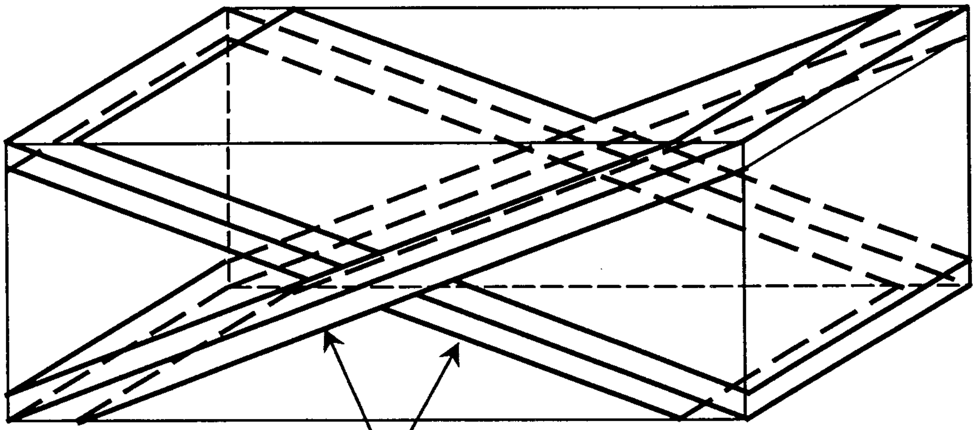

Figure 1.3 The unit cell of the "Fiber Inclination Model" composed of four unidirectional laminae

Whitney et al. (1989) extended the Fiber Inclination Model to predict the in-plane elastic properties of 3-D angle-interlock textile structural composites. In the case of angle-interlock geometry, the unit cell is inherently more complex. Since there are no repeatable units in the thickness direction, the unit cell essentially occupied the entire preform thickness. Also, the yarns can occupy any number of positions within the unit cell. Yarns in warp and weft directions may occupy positions which are horizontal or inclined in the thickness direction. To account for varying bundle positions, the authors divided the unit cell into micro-cells that are repeated to reconstruct the entire unit cell, and the calculations are made on a generic unit cell with micro-cells. Crimping of fibers at the corners of the cell and the intersection of fibers at the unit cell center are ignored.

Stiffness averaging method was also used to predict elastic constants of two-step braided composites by Byun et al. (1991). The architecture of this material was investigated by identifying the geometric and braiding process parameters which include the linear density ratio between axial and braider yarns, the aspect ratio of axial yarn and the aspect ratio of braider yarn. The predicted results of axial tensile modulus shows reasonably good agreements with test results, however, shear moduli show a lack of agreement between prediction and measurement.

All the aforementioned models are based on the concept of averaging stiffness. Ma et al. (1990) developed another methodology based on an energy approach to evaluate elastic stiffness of 3-D braided textile structural composites. Three types of elastic strain energies in the composite rods were taken into account. These included the strain energies due to bending, extension, and compression over the region of fiber contact. Closed form expressions for axial elastic moduli and Poisson's ratio were derived as functions of fiber volume fraction and fiber orientations. Numerical results show that the axial elastic moduli are sensitive to the geometrical braiding pattern. The moduli increase as the yarn orientation angle decreases, that is, the fiber becomes more aligned with the tensile axis.

Fiber bundle orientations are the essential geometrical properties for determining mechanical behavior. For the sake of simplicity, the geometry of 3-D composites have been represented by idealization rather than reality by most researchers. Most models have dealt with perfectly regular structures. The fibers are assumed to be straight inside a unit cell. However, real composites are highly irregular, and waviness of fibers is unavoidable. The angles between axial tows and braiders change in an irregular way. In order to take account of these irregularities, Cox and Dadkhah (1995) promoted a more practical approach to characterize the geometrical inconsistencies of typical triaxially braided composites. Out-of-plane misalignments were taken into account by introducing a cumulative probability distribution (CPD) for the misalignment angle ξ. Typical CPDs can be fit quite well by a symmetric normal distribution $F_\xi(\xi)$ with corresponding density function $f_\xi(\xi) = dF_\xi / d\xi$ given by

$$f_\xi(\xi) = \frac{1}{\sigma_\xi\sqrt{2\pi}} \exp\left(-\xi^2 / 2\sigma_\xi^2\right).$$

The standard deviation σ_ξ can be determined experimentally. The Young's modulus E_x can be determined by

$$< E_x > = \left\{ \int_{-\infty}^{\infty} \frac{f_\xi(\xi) d\xi}{\overline{E}_x} \right\}^{-1}$$

Where $\overline{E}_x(\xi)$ is Young's modulus for a unidirectional composite under a load oriented at angle ξ to the fiber direction X. $\overline{E}_x(\xi)$ can be expressed by

$$\frac{1}{\overline{E}_x(\xi)} = \frac{\cos^4 \xi}{E_x} + \cos^2 \xi \sin^2 \xi \left(\frac{1}{G_{xy}} - \frac{2\upsilon_{xy}}{E_x} \right) + \frac{\sin^4 \xi}{E_y}$$

1.3 Stress and Strength Analysis of Three Dimensional Composites

Strength of 3-D composites is more difficult to predict than stiffness. This section summarizes work done on predicting the strength, fracture, and damage tolerance behavior of 3-D composites.

Ishikawa and Chou (1983) developed a 2-D fiber undulation model based on classical lamination theory which considered the undulation in the fill yarn direction but neglected the undulation in the warp yarns of woven composites. They modeled nonlinear shear response of both the fill yarns and the interstitial matrix along with the effects of transverse cracking of the warp yarns to predict the knee in the stress-strain response of woven composites. Kriz (1985) used a generalized plane strain finite element model which assumed a linear undulation path for the fill and warp yarns to study the effect of transverse cracking on the stiffness and internal stresses of a glass/epoxy plain weave composite.

Stanton and Kipp (1985) developed a nonlinear constitutive model for plain weave carbon-carbon composites which accounted for the differences in tension and compression response, warp-fill crossover damage and multiaxial stress interactions using a simple interaction formula along with experimental stress-strain data for all six components under tension and compression loading. Jortner (1986) developed a 2-D mechanistic model which modeled the undulations of the fill yarns but neglected the undulations of warp yarns. He used a stress-averaging scheme which accounted for the nonlinear shear response of the fill yarns and the transverse cracking of the warp yarns to analyze plain weave carbon-carbon composites.

Ko and Pastore (1985) used a fabric geometry model to define the yarn orientations in a three-dimensional braided composite. They used the yarn orientations to first estimate the strength of the fabric preform and then compute composite strength using a simple rule of mixtures. Ko (1989) also used the fabric geometry model together with a maximum strain energy criterion to predict yarn failures and ultimate strength of a 3-D braided composite.

Dow and Ramnath (1987) modeled woven fabric composites using a simple geometry model that assumed a linear undulation path for the fill and warp yarns. They computed constituent fiber and matrix stresses from local yarn stresses which were calculated using an iso-strain assumption and predicted failure based on the average stresses in the fiber and the matrix along with a maximum stress criterion. Dow and Ramnath (1987) used the fabric geometry model together with a simple linear yarn bending model and an iso-strain assumption to compute average fiber and matrix stresses which were used to predict local yarn failure and strength for 2-D triaxial braided composites.

Naik (1994 & 1995) developed a micromechanics analysis technique for the prediction of failure initiation, damage progression, and strength of 2-D woven and braided composite materials. The yarn architecture was discretely modeled using sinusoidal undulations at yarn crossovers. Overall thermal and mechanical properties were calculated based on an iso-strain assumption. This analysis technique included the effects of nonlinear shear response and nonlinear material response due to the accumulation of damage in the yarns and the interstitial matrix and also the effects of yarn bending and the geometrically nonlinear effects of yarn straightening/wrinkling during axial tension/compression loading. Parametric studies were also performed on the woven and braided architectures to investigate the effects of yarn size, yarn spacing, yarn crimp, braid angle, and overall fiber volume fraction on the strength properties of the textile composite.

Three-dimensional finite element models (FEM) have also been used for the prediction of nonlinear material properties (Bhandarker et al 1991) and the modeling of damage (Blackketter 1993) of plain weave composites. The 3-D FEMs are highly computer intensive and also require considerable time and effort for model generation. Foye (1993) developed homogenized replacement finite elements and analyzed sub-cells within the repeating unit cell to overcome these limitations. However, he had to manually calculate the orientations of the different yarn directions, yarn interfacial planes and volume fractions, for each element in the 3-D model. FEM is, therefore, not well suited for performing parametric studies to investigate the sensitivity of composite strength properties to fabric architecture parameters.

Compared with the regular finite element analysis, a global/local finite element method which was developed by Sun and Mao (1988 & 1990) is more efficient to analyze textile composites. The global/local finite element method was based on the regular finite element method in conjunction with three basic steps, i.e. the global analysis, the local analysis and the refined global analysis. In the first two steps, a coarse finite element mesh was used to analyze the entire structure to obtain the nodal displacements which were subsequently used as displacement boundary conditions for local regions of interest. These local regions with the prescribed boundary conditions were then analyzed with refined meshes to obtain more accurate stresses. In the third step, a new global displacement distribution based on the results of the previous two steps was assumed for the analysis, from which much improved solutions for both stresses and displacements were produced.

Woo and Whitcomb (1994 & 1996) utilized global/local finite elements to analyze textile composites. A relatively crude global mesh was used to obtain the overall response of the structure and refined local meshes were used in the region of interest where rapid stress change may occur. The homogenized engineering properties could be used in the crude global mesh away from the free boundary and transitional regions. In the local meshes, the details of the coarse microstructure of textile composites(e.g., the individual tows and matrix pockets) could be modeled discretely. In the transitional range of microstructure, however, discrete modeling may not be practical even with supercomputers due to the huge computer memory and CPU requirements. Use of homogenized material properties is also usually inappropriate. In this range, special macro finite elements can be used. The macroelements employ a number of subdomains or subelements to account for the microstructural details inside individual elements. Whitcomb et al. (1994) discussed two types of macroelements. The elements described in these references are based on single or multiple assumed displacement fields.

The global/local method with local refinement assumes that the region which requires further mesh refinement can be localized. If the solution behavior is complicated everywhere, the correction by the global/local iteration does not necessarily reflect the nature of the true solution accurately. For example, if the solution behavior is complicated everywhere and only some portion of the global domain is refined in the local mesh, the global/local iteration may do more harm than good in solving the problem. A solution to this problem is using an engineering global/local analysis. In this procedure, the initial coarse global solution is assumed to be close enough for the purpose at hand. That is, no global/local iteration is employed. The local problem is solved only once with boundary displacements from the coarse global solution.

Chapter 2

Analytical Characterization of Three Dimensional Woven Composites

Composite materials reinforced with woven fabric preforms are being considered for potential structural application in the aircraft and automotive industries. Fabric-reinforced textile composites potentially have better out-of-plane stiffness, strength and toughness properties than conventional laminates. However, the architecture of a textile composite is complex and, therefore, the parameters controlling its mechanical properties are numerous. Mechanical testing to characterize all the effects of textile architecture could be an economically unrealistic proposition. In order to facilitate the design of fabric-reinforced composite structures, it is crucial to develop experimentally verified analytical models for the prediction of both the uniaxial and multiaxial stiffness and strength properties.

2.1 Woven Patterns

Xu et al. (1994) provided complete statements of the rather complex sequencing of through-the-thickness yarns. Figure 2.1 shows the three typical types of weave in woven composites, namely, (a) layer to layer, (b) through the thickness angle interlock, (c) orthogonal interlock weaves.

In woven composites, the stuffers and fillers alternate in layers through the thickness. The stuffers and fillers form a coarse 0°/90° array shown in figure 2.1 for most woven composites. Nevertheless, the proposed method allows the arbitrary orientation of stuffers and fillers in the X-Y plane. The through the thickness reinforcement, or warp weavers, may be oriented in any direction with reference to the 3D composite coordinate axes. Stitched composites may be modeled by weaver or stitch fibers that are oriented perpendicular to the X-Y plane and parallel to the Z-axis of the composite.

2.2 Fiber Arrangement

Complete understanding of arrangement of fibers, including stuffer, filler, and warp weaver fibers, is essential to predict the engineering properties accurately. Woven composites are typically composed of n_s layers of stuffers and n_s+1 layers of fillers through the thickness as shown in Figure 2.2.

In order to estimate the elastic properties of 3-D woven composites, an approach based on modified laminate theory and orientation average is used. First of all, composites are divided into plies so that every ply contains either stuffer or filler fibers as shown in Figure 2.3. Since the weaver fibers go through the entire thickness, each ply must contain some weaver fibers for woven composites.

For orientation averaging, a three-dimensional fiber arrangement can be considered as composed of two types of structures, the baseline structure formed by fibers in X-Y plane direction, such as stuffer fibers and filler fibers, and the interwoven or braided structure composed of warp weaver fibers which penetrate the thickness of composites. Therefore each ply contains two types of domains, the primary domains which consist of baseline fibers, and the weaver domains which consist of weaver fibers, the occupying volume fractions of these domains are denoted by f_p and f_w respectively. Each domain is characterized by an orientation along which the fibers within it are presumed to lie. All of the fibers in the primary domains are assumed to be parallel to X-Y plane and each ply can consist of the primary fibers in the same direction. Warp weaver fibers are always assumed to be piecewise straight and their orientations are defined by the directional angles to the X,Y,Z axes.

Let $[E^{(\alpha)}]$ denote the stiffness matrix for domain α. Based on orientation averaging method, the composite stiffness matrix $[E_C]$ of 3-D woven composite can be predicted by the following equation:

$$[E_C] = \sum_{\alpha} f_\alpha \left[\tilde{E}^{(\alpha)}\right] \tag{2-1}$$

Where $[\tilde{E}^{(\alpha)}]$ denotes $[E^{(\alpha)}]$ transformed from domain α material coordinate system into the composite coordinate system and f_α denotes volume fraction of domain α.

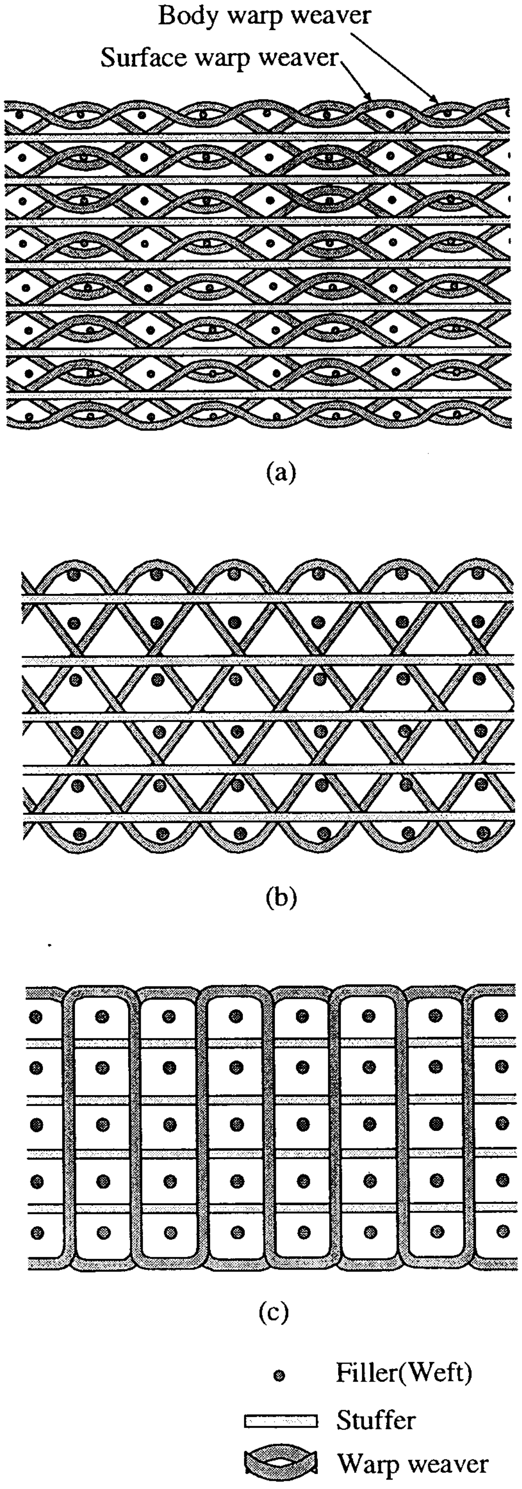

Figure 2.1 Schematics of (a) layer-to-layer angle interlock, (b) through-the- thickness angle interlock, and (c) orthogonal interlock weaves.

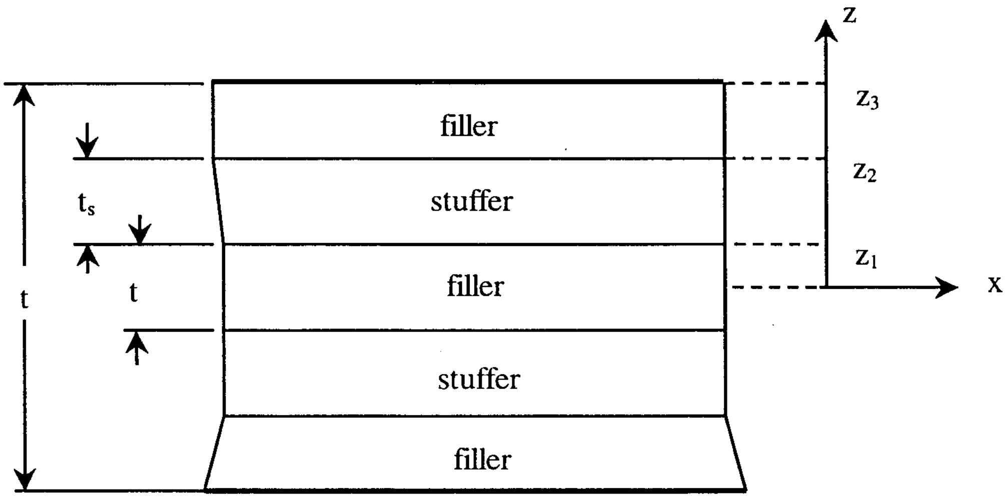

Figure 2.2 Representative layer sequence of fillers and stuffers through the thickness, with the layer thickness t_f and t_s defined. For the case shown, $n_s = 2$.

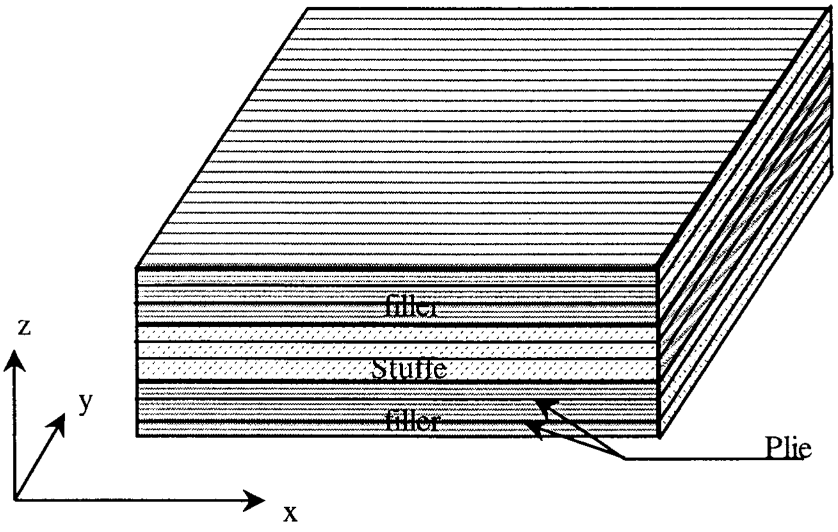

Figure 2.3 Schematic of ply division in 3D woven composites

2.3 Three Dimensional Hygrothermoelastic Properties

The first step in the computation of composite properties for any fiber configuration is the evaluation of the local orthotropic properties of a unidirectional composite ply. From composite mechanics (Jones, 1975), the compliance (inverse stiffness) matrix in material axes for each orthotropic ply written in terms of the engineering constants is

$$\left[\overline{E}_{\alpha}\right]^{-1} = \begin{bmatrix} \frac{1}{E_{11}} & -\frac{\upsilon_{21}}{E_{22}} & -\frac{\upsilon_{31}}{E_{33}} & 0 & 0 & 0 \\ -\frac{\upsilon_{12}}{E_{11}} & \frac{1}{E_{22}} & -\frac{\upsilon_{32}}{E_{33}} & 0 & 0 & 0 \\ -\frac{\upsilon_{13}}{E_{11}} & -\frac{\upsilon_{23}}{E_{22}} & \frac{1}{E_{33}} & 0 & 0 & 0 \\ 0 & 0 & 0 & \frac{1}{G_{23}} & 0 & 0 \\ 0 & 0 & 0 & 0 & \frac{1}{G_{31}} & 0 \\ 0 & 0 & 0 & 0 & 0 & \frac{1}{G_{12}} \end{bmatrix} \tag{2-2}$$

Total ply stiffness properties of a composite layer containing one primary in-plane fiber orientation and N_w weaver orientations can be obtained from combination of the primary domain and weaver domain properties according to their volume fractions. Note that it is possible for a ply to have multiple weaver domains, but only one primary domain is considered. Therefore the stiffness matrix for the *ith* layer containing the primary and weaver domains may be written as:

$$\left[\overline{E}_i\right] = f_p\left[\overline{R}_i^{\,p}\right]^T\left[\overline{E}_i^{\,p}\right]\left[\overline{R}_i^{\,p}\right] + \sum_{j=1}^{N_w} f_{w_j}\left[\overline{R}_i^{\,w_j}\right]^T\left[\overline{E}_i^{\,w_j}\right]\left[\overline{R}_i^{\,w_j}\right] \tag{2-3}$$

where

$\overline{E}_i$ is the three dimensional lamina stiffness matrix of *ith* ply.

$\overline{R}_i^p$ is the two dimensional coordinate transformation matrix from primary domain material axes to composite structural axes. If the angle between material axes and structural axes is θ, $\overline{R}_i^p$ can be expressed by

$$\overline{R}_i^p = \begin{bmatrix} \cos^2\theta & \sin^2\theta & 0 & 0 & 0 & 2\cos\theta\sin\theta \\ \sin^2\theta & \cos^2\theta & 0 & 0 & 0 & -2\cos\theta\sin\theta \\ 0 & 0 & 1 & 0 & 0 & 0 \\ 0 & 0 & 0 & \cos\theta & -\sin\theta & 0 \\ 0 & 0 & 0 & \sin\theta & \cos\theta & 0 \\ -\cos\theta\sin\theta & \cos\theta\sin\theta & 0 & 0 & 0 & \cos^2\theta-\sin^2\theta \end{bmatrix}$$

f_p is the primary domain volume fraction

N_w is the number of weaver domains, each weaver domain consists of weaver fibers in the same direction. If weavers contain fibers in different directions, they should be grouped into different weaver domains.

$\overline{R}_i^{w_j}$ is the three dimensional coordinate transformation matrix from *jth* weaver domain material axes to composite structural axes. Since directions of weavers are arbitrary, three dimensional coordinate transformation matrix is used here. If the direction cosines between the weaver local axes and structural axes are l_1, m_1, …, n_3, $\overline{R}_i^{w_j}$ can be written as (Lekhnitskii 1977),

$$\overline{R}_i^{w_i} = \begin{bmatrix} l_1^2 & m_1^2 & n_1^2 & l_1 m_1 & m_1 n_1 & n_1 l_1 \\ l_2^2 & m_2^2 & n_2^2 & l_2 m_2 & m_2 n_2 & n_2 l_2 \\ l_3^2 & m_3^2 & n_3^2 & l_3 m_3 & m_3 n_3 & n_3 l_3 \\ 2l_1 l_2 & 2m_1 m_2 & 2n_1 n_2 & (l_1 m_2 + l_2 m_1) & (m_1 n_2 + m_2 n_1) & (n_1 l_2 + n_2 l_1) \\ 2l_2 l_3 & 2m_2 m_3 & 2n_2 n_3 & (l_2 m_3 + l_3 m_2) & (m_2 n_3 + m_3 n_2) & (n_2 l_3 + n_3 l_2) \\ 2l_3 l_1 & 2m_3 m_1 & 2n_3 n_1 & (l_3 m_1 + l_1 m_3) & (m_3 n_1 + m_1 n_3) & (n_3 l_1 + n_1 l_3) \end{bmatrix}$$

f_{w_i} is the *jth* weaver domain volume fraction

Note: $f_p + \sum_{j=1}^{N_w} f_{w_i} = 1$

$\overline{E}_i^{w_i}$ is the stiffness matrix in the local coordinate system of *jth* weaver in *ith* ply. Before damage occurs, $\overline{E}_i^{w_i}$ should be same for each *i* since we assume every layer to have the same weaver arrangement. But after damage, every layer may have its own property degradation which could be different between layers, therefore degraded $\overline{E}_i^{w_i}$ could be different for different *i*.

In order to differentiate three dimensional properties from two dimensional properties which are discussed in the next section, an overbar is added to three dimensional stiffness matrices and coordinate transformation matrices, such as $[\overline{E}_i]$ and $[\overline{R}_i]$.

The averaged properties of the entire composite laminate can be obtained by summing up all the layer properties and the properties due to interply distortion energy (Murthy and Chamis 1986). The interply distortion energy terms represent the stiffening effects of changes in the primary fiber orientation angles between adjacent layers. Therefore the composite laminate stiffness matrix is written as:

$$\left[\overline{E}_C\right] = \frac{1}{t_C}\left[\sum_{i=1}^{N_l}\left(z_{i+1} - z_i\right)\left[\overline{E}_i\right] + \sum_{j=1}^{N_l-1} H_j\left[\overline{S}_j\right]\right] \tag{2-4}$$

where

$\overline{E}_C$ is the three dimensional stiffness matrix of entire composite.

t_C is the thickness of the entire composite.

N_l is the number of plies of the entire composite.

z_i is the distance from reference plane to the bottom of *ith* ply.

H_j is the interply layer distortion energy coefficient.

$\overline{S}_j$ is generated from the following equation (Murthy and Chamis, 1986):

$$\left[\overline{S}_j\right] = \begin{bmatrix} A^2 & -A^2 & 0 & 0 & 0 & -AB \\ -A^2 & A^2 & 0 & 0 & 0 & AB \\ 0 & 0 & 0 & 0 & 0 & 0 \\ 0 & 0 & 0 & 0 & 0 & 0 \\ 0 & 0 & 0 & 0 & 0 & 0 \\ -AB & AB & 0 & 0 & 0 & B^2 \end{bmatrix} \tag{2-5}$$

$A = \sin 2\theta_{j+1} - \sin 2\theta_j$

$B = \cos 2\theta_{j+1} - \cos 2\theta_j$

θ_j is the fiber angle of *jth* ply from material axes to composite structural axes.

Thermal and hygral coefficients of expansion about the composite structural axes can be obtained from the following equations:

$$\{\overline{\alpha}_C\} = \frac{1}{t_C}\left[\overline{E}_C\right]^{-1}\sum_{i=1}^{N_l}\left(z_{i+1} - z_i\right)\left[f_p\left[\overline{R}_i^p\right]^T\left[\overline{E}_i^p\right]\left[\overline{R}_i^p\right]\{\overline{\alpha}_i^p\} + \sum_{j=1}^{N_w} f_{w_j}\left[\overline{R}_i^{w_j}\right]^T\left[\overline{E}_i^{w_j}\right]\left[\overline{R}_i^{w_j}\right]\{\overline{\alpha}_i^{w_j}\}\right] \tag{2-6}$$

$$\{\overline{\beta}_C\} = \frac{1}{t_C}\left[\overline{E}_C\right]^{-1}\sum_{i=1}^{N_l}\left(z_{i+1} - z_i\right)\left[f_p\left[\overline{R}_i^p\right]^T\left[\overline{E}_i^p\right]\left[\overline{R}_i^p\right]\{\overline{\beta}_i^p\} + \sum_{j=1}^{N_w} f_{w_j}\left[\overline{R}_i^{w_j}\right]^T\left[\overline{E}_i^{w_j}\right]\left[\overline{R}_i^{w_j}\right]\{\overline{\beta}_i^{w_j}\}\right] \tag{2-7}$$

Where $\{\overline{\alpha}_C\},\{\overline{\beta}_C\}$ are thermal and moisture coefficients of expansion about the composite structural axes.

$$\{\overline{\alpha}_C\} = \left\{\alpha_{C_{11}}, \alpha_{C_{22}}, \alpha_{C_{33}}, \alpha_{C_{23}}, \alpha_{C_{13}}, \alpha_{C_{12}}\right\} \tag{2-8}$$

$$\{\overline{\beta}_C\} = \left\{\beta_{C_{11}}, \beta_{C_{22}}, \beta_{C_{33}}, \beta_{C_{23}}, \beta_{C_{13}}, \beta_{C_{12}}\right\} \tag{2-9}$$

2.4 Two Dimensional Hygrothermoelastic Properties

In most cases computational evaluation of composite structures is carried out by using plate and shell finite elements. Therefore, the composite properties need be expressed as two-dimensional plate stiffness with membrane and bending degrees of freedom. The resultant forces and moments in terms of the middle surface extensional strain and curvatures can be expressed as:

$$\begin{Bmatrix} \{N\} \\ \{M\} \end{Bmatrix} = \begin{bmatrix} [A] & [B] \\ [B] & [D] \end{bmatrix}\begin{Bmatrix} \{\varepsilon\} \\ \{\kappa\} \end{Bmatrix} - \begin{Bmatrix} \{N_T\} \\ \{M_T\} \end{Bmatrix} - \begin{Bmatrix} \{N_M\} \\ \{M_M\} \end{Bmatrix} \tag{2-10}$$

where

$\{N\}=\left\{N_x, N_y, N_{xy}\right\}^T$

$\{M\}=\left\{M_x, M_y, M_{xy}\right\}^T$

$\{\varepsilon\}=\left\{\varepsilon_x, \varepsilon_y, \varepsilon_{xy}\right\}$ is the reference plane membrane strains.

$\{\kappa\}=\left\{\kappa_x, \kappa_y, \kappa_{xy}\right\}$ is the reference plane curvatures.

$\left\{N_T\right\}$, $\left\{N_M\right\}$ is the resultant forces due to temperature and moisture change.

$\left\{M_T\right\},\left\{M_M\right\}$ is the resultant moments due to temperature and moisture change.

For a three-dimensionally reinforced laminate containing layers of primary and woven fiber reinforcement domains, the resultant forces due to external load can be obtained from the following equation:

$$\begin{aligned}\left\{N_\varepsilon\right\} &= \sum_{i=1}^{N_l}\int_{z_{i-1}}^{z_i}\left\{\sigma_i\right\}dz \\ &= \sum_{i=1}^{N_l}\int_{z_{i-1}}^{z_i}\left[E_i\right]\left(\{\varepsilon\}+z\{\kappa\}\right)dz \\ &= \sum_{i=1}^{N_l}\int_{z_{i-1}}^{z_i}\left[f_p\left[R_i^p\right]^T\left[E_i^p\right]\left[R_i^p\right]+\sum_{j=1}^{N_w} f_{w_i}\left[\widetilde{E}_i^{w_i}\right]\right]\left(\{\varepsilon\}+z\{\kappa\}\right)dz \\ &= \left[A'\right]\{\varepsilon\}+\left[B'\right]\{\kappa\}\end{aligned} \tag{2-11}$$

where

$$\left[E_i\right]=f_p\left[R_i^p\right]^T\left[E_i^p\right]\left[R_i^p\right]+\sum_{j=1}^{N_w} f_{w_i}\left[\widetilde{E}_i^{w_i}\right] \tag{2-12}$$

$$[A'] = \sum_{i=1}^{N_l} (z_i - z_{i-1}) \left[f_p [R_i^p]^T [E_i^p][R_i^p] + \sum_{j=1}^{N_w} f_{w_j} [\tilde{E}_i^{w_j}] \right]$$

$$[B'] = \frac{1}{2} \sum_{i=1}^{N_l} (z_i^2 - z_{i-1}^2) \left[f_p [R_i^p]^T [E_i^p][R_i^p] + \sum_{j=1}^{N_w} f_{w_j} [\tilde{E}_i^{w_j}] \right]$$

and E_i is the two dimensional lamina stiffness matrix of *ith* ply.

E_i^p is the two dimensional lamina stiffness of primary domain of *ith* ply in local axes.

$$[E_i^p] = \begin{bmatrix} \dfrac{1}{E_{11}} & -\dfrac{\upsilon_{21}}{E_{22}} & 0 \\ -\dfrac{\upsilon_{12}}{E_{11}} & \dfrac{1}{E_{22}} & 0 \\ 0 & 0 & \dfrac{1}{G_{12}} \end{bmatrix}$$

R_i^p is the two dimensional coordinate transformation matrix of primary domain.

$$[R_i^p] = \begin{bmatrix} \cos^2\theta_i & \sin^2\theta_i & \frac{1}{2}\sin 2\theta_i \\ \sin^2\theta_i & \cos^2\theta_i & -\frac{1}{2}\sin 2\theta_i \\ -\sin 2\theta_i & \sin 2\theta_i & \cos 2\theta_i \end{bmatrix}$$

$\tilde{E}_i^{w_j}$ is the two dimensional stiffness of weaver domain in structural axes. It can be obtained by extracting relevant terms, which correspond to σ_{11}, σ_{22}, σ_{12}, from the three dimensional stiffness matrix that can be generated by the following transformation:

$$[\overline{R}_i^{w_j}]^T [\overline{E}_i^{w_j}][\overline{R}_i^{w_j}]$$

Superimposing the stiffness contributions due to interply layer distortion energy:

$$
\begin{aligned}
[A] &= [A'] + \sum_{j=1}^{N_l-1} H_j \left[S_j\right] \\
&= \sum_{i=1}^{N_l} \left(z_i - z_{i-1}\right) \left[f_p \left[R_i^p\right]^T \left[E_i^p\right] \left[R_i^p\right] + \sum_{j=1}^{N_w} f_{w_j} \left[\tilde{E}_i^{w_j}\right] \right] + \sum_{j=1}^{N_l-1} H_j \left[S_j\right]
\end{aligned}
\tag{2-13}
$$

$$
\begin{aligned}
[B] &= [B'] + \sum_{j=1}^{N_l-1} z'_j H_j \left[S_j\right] \\
&= \frac{1}{2} \sum_{i=1}^{N_l} \left(z_i^2 - z_{i-1}^2\right) \left[f_p \left[R_i^p\right]^T \left[E_i^p\right] \left[R_i^p\right] + \sum_{j=1}^{N_w} f_{w_j} \left[\tilde{E}_i^{w_j}\right] \right] + \sum_{j=1}^{N_l-1} z'_j H_j \left[S_j\right]
\end{aligned}
\tag{2-14}
$$

where z'_j is the distance from the interply layer to the composite reference plane (mid-thickness).

Similarly,

$$
\begin{aligned}
\left\{M_\varepsilon\right\} &= \sum_{i=1}^{N_l} \int_{z_{i-1}}^{z_i} \left\{\sigma_i\right\} z \, dz \\
&= \sum_{i=1}^{N_l} \int_{z_{i-1}}^{z_i} \left[E_i\right] \left(\{\varepsilon\} + z\{\kappa\}\right) z \, dz \\
&= \sum_{i=1}^{N_l} \int_{z_{i-1}}^{z_i} \left[f_p \left[R_i^p\right]^T \left[E_i^p\right] \left[R_i^p\right] + \sum_{j=1}^{N_w} f_{w_j} \left[\tilde{E}_i^{w_j}\right] \right] \left(\{\varepsilon\} + z\{\kappa\}\right) z \, dz \\
&= [B']\{\varepsilon\} + [D']\{\kappa\}
\end{aligned}
\tag{2-15}
$$

where

$$
[D'] = \frac{1}{3} \sum_{i=1}^{N_l} \left(z_i^3 - z_{i-1}^3\right) \left[f_p \left[R_i^p\right]^T \left[E_i^p\right] \left[R_i^p\right] + \sum_{j=1}^{N_w} f_{w_j} \left[\tilde{E}_i^{w_j}\right] \right]
$$

Superimposing the stiffness due to interply layer distortion:

$$
\begin{aligned}
[D] &= [D'] + \frac{1}{2}\sum_{j=1}^{N_l-1} z_j'^2 H_j \left[S_j\right] \\
&= \frac{1}{3}\sum_{i=1}^{N_l}\left(z_i^3 - z_{i-1}^3\right)\left[f_p\left[R_i^p\right]^T\left[E_i^p\right]\left[R_i^p\right] + \sum_{j=1}^{N_w} f_{w_j}\left[\tilde{E}_i^{w_j}\right]\right] + \frac{1}{2}\sum_{j=1}^{N_l-1} z_j'^2 H_j \left[S_j\right]
\end{aligned}
$$

(2-16)

For the primary domain, the thermal forces are

$$
\left\{N_{T_i}^p\right\} = \int_{z_{i-1}}^{z_i} \left[E_i^p\right]\Delta T\left\{\alpha_i^p\right\}dz = (z_i - z_{i-1})\Delta T\left[E_i^p\right]\left\{\alpha_i^p\right\} \qquad (2\text{-}17)
$$

For the *jth* weaver domain, the thermal forces are

$$
\left\{N_{T_i}^{w_j}\right\} = \int_{z_{i-1}}^{z_i} \left[E_i^{w_j}\right]\Delta T\left\{\alpha_i^{w_j}\right\}dz = (z_i - z_{i-1})\Delta T\left[E_i^{w_j}\right]\left\{\alpha_i^{w_j}\right\} \qquad (2\text{-}18)
$$

Transforming $N_{T_i}^p$ and $N_{T_i}^{w_j}$ to global axes, and then averaging them in terms of the weight of their volume fraction to get resultant force for *ith* ply in global coordinate system due to temperature change:

$$
\begin{aligned}
\left\{N_{T_i}\right\} &= f_p\left[R_i^p\right]\left\{N_{T_i}^p\right\} + \sum_{j=1}^{N_w} f_{w_j}\left[R_i^{w_j}\right]\left\{N_{T_i}^{w_j}\right\} \\
&= \Delta T_i\left(z_i - z_{i-1}\right)\left\{ f_p\left[R_i^p\right]\left[E_i^p\right]\left\{\alpha_i^p\right\} + \sum_{j=1}^{N_w} f_{w_j}\left[R_i^{w_j}\right]\left[E_i^{w_j}\right]\left\{\alpha_i^{w_j}\right\}\right\}
\end{aligned}
$$

(2-19)

Summing up the N_{T_i} for all plies to get the resultant thermal force for entire composite structure:

$$
\begin{aligned}
\{N_T\} &= \sum_{i=1}^{N_l} \{N_{T_i}\} \\
&= \sum_{i=1}^{N_l} \left[\Delta T_i \left(z_i - z_{i-1}\right) \left\{ f_p \left[R_i^p\right]\left[E_i^p\right]\left\{\alpha_i^p\right\} + \sum_{j=1}^{N_w} f_{w_j} \left[R_i^{w_j}\right]\left[E_i^{w_j}\right]\left\{\alpha_i^{w_j}\right\} \right\} \right]
\end{aligned}
$$

(2-20)

Similarly, $\{N_M\}, \{M_T\}$ and $\{M_M\}$ can be generated by:

$$\{N_M\} = \sum_{i=1}^{N_l} \left[\Delta M_i \left(z_i - z_{i-1}\right) \left\{ f_p \left[R_i^p\right]\left[E_i^p\right]\left\{\beta_i^p\right\} + \sum_{j=1}^{N_w} f_{w_j} \left[R_i^{w_j}\right]\left[E_i^{w_j}\right]\left\{\beta_i^{w_j}\right\} \right\} \right] \tag{2-21}$$

$$\{M_T\} = \frac{1}{2} \sum_{i=1}^{N_l} \left[\Delta T_i \left(z_i^2 - z_{i-1}^2\right) \left\{ f_p \left[R_i^p\right]\left[E_i^p\right]\left\{\alpha_i^p\right\} + \sum_{j=1}^{N_w} f_{w_j} \left[R_i^{w_j}\right]\left[E_i^{w_j}\right]\left\{\alpha_i^{w_j}\right\} \right\} \right] \tag{2-22}$$

$$\{M_M\} = \frac{1}{2} \sum_{i=1}^{N_l} \left[\Delta M_i \left(z_i^2 - z_{i-1}^2\right) \left\{ f_p \left[R_i^p\right]\left[E_i^p\right]\left\{\beta_i^p\right\} + \sum_{j=1}^{N_w} f_{w_j} \left[R_i^{w_j}\right]\left[E_i^{w_j}\right]\left\{\beta_i^{w_j}\right\} \right\} \right] \tag{2-23}$$

2.5 Stresses in the primary domain and in the weaver domain

In order to perform damage propagation simulation, one needs to evaluate the stresses in stuffer, filler, and weaver fibers and matrices. For most composite structures, the first step for stress analysis is the assembly of a finite element model using the stiffness properties given in the previous section. After finite element analysis, the resultant forces and moments are obtained for each node. From equation (2-10), we can write:

$$\begin{Bmatrix} \{\varepsilon\} \\ \{\kappa\} \end{Bmatrix} = \begin{bmatrix} [A] & [B] \\ [B] & [D] \end{bmatrix}^{-1} \left\{ \begin{Bmatrix} \{N\} \\ \{M\} \end{Bmatrix} + \begin{Bmatrix} \{N_T\} \\ \{M_T\} \end{Bmatrix} + \begin{Bmatrix} \{N_M\} \\ \{M_M\} \end{Bmatrix} \right\} \tag{2-24}$$

The strains and stresses in global axes for a specific ply—the *ith* ply can be obtained from the following equations:

$$\begin{aligned} \{\varepsilon_i\} &= \{\varepsilon\} - z\{\kappa\} \\ &= [A]^{-1}\{\{N\} + \{N_T\} + \{N_M\} - [B]\{\kappa\}\} - z\{\kappa\} \end{aligned} \tag{2-25}$$

$$\{\sigma_i\} = [E_i]\left(\{\varepsilon_i\} - \Delta T_i\{\alpha_i\} - \Delta M_i\{\beta_i\}\right) \tag{2-26}$$

where

$$\{\varepsilon_i\} = \{\varepsilon_{11}^{(i)}, \varepsilon_{22}^{(i)}, \varepsilon_{12}^{(i)}\}$$

$$\{\sigma_i\} = \{\sigma_{11}^{(i)}, \sigma_{22}^{(i)}, \sigma_{12}^{(i)}\}$$

the other stress components $\sigma_{13}^{(i)}, \sigma_{23}^{(i)}, \sigma_{33}^{(i)}$ can be obtained from the transverse shear resultants Q_{13}, Q_{23} and the transverse pressures P_u, P_l by the following equation (Vladimir, 1975):

$$\begin{Bmatrix} \sigma_{13}^{(i)} \\ \sigma_{23}^{(i)} \\ \sigma_{33}^{(i)} \end{Bmatrix} = \begin{Bmatrix} \dfrac{1.5\mathrm{Q}_{13}}{t_c}\left(1 - \dfrac{4z_i^{\,2}}{t_c^2}\right) \\ \dfrac{1.5\mathrm{Q}_{13}}{t_c}\left(1 - \dfrac{4z_i^{\,2}}{t_c^2}\right) \\ \dfrac{P_u + P_l}{2} + 1.5(P_u - P_l)\left(\dfrac{z_i}{t_c} - \dfrac{16z_i^3}{3t_c^3}\right) \end{Bmatrix} \tag{2-27}$$

Stresses in the primary and weaver domains are computed from the corresponding strains using the appropriate stress-strain relations. Since the primary domain is in the same plane as the ply, it has the same strain components as the ply, that is

$$\{\varepsilon_i^p\} = [R_i^p]\{\varepsilon_i\} \tag{2-28}$$

and the primary domain stresses are computed from:

$$\begin{aligned}\{\sigma_i^p\} &= [E_i^p][R_i^p][A]^{-1}(\{N\} + \{N_T\} + \{N_M\} - [B]\{\kappa\}) \\ &\quad - [E_i^p](\Delta T_i\{\alpha_i^p\} + \Delta M_i\{\beta_i^p\} + z[R_i^p]\{\kappa\})\end{aligned} \tag{2-29}$$

Since the weaver is not in the same plane as the ply, one needs to transform the three dimensional strain components of the ply to the weaver axes to obtain the weaver strains. Weaver domain stresses can be computed from the weaver strains.

The three dimensional stress-strain-temperature-moisture relationship can be expressed as:

$$\{\bar{\sigma}_i\} = [\bar{E}_i](\{\bar{\varepsilon}_i\} - \Delta T_i\{\bar{\alpha}_i\} - \Delta M_i\{\bar{\beta}_i\}) \tag{2-30}$$

where

$$\{\bar{\sigma}_i\} = \{\sigma_{11}^{(i)}, \sigma_{22}^{(i)}, \sigma_{33}^{(i)}, \sigma_{23}^{(i)}, \sigma_{13}^{(i)}, \sigma_{12}^{(i)}\}^T$$

$$\{\bar{\varepsilon}_i\} = \{\varepsilon_{11}^{(i)}, \varepsilon_{22}^{(i)}, \varepsilon_{33}^{(i)}, \varepsilon_{23}^{(i)}, \varepsilon_{13}^{(i)}, \varepsilon_{12}^{(i)}\}^T$$

From (2-25) and (2-27), we computed $\varepsilon_{11}^{(i)}, \varepsilon_{22}^{(i)}, \varepsilon_{12}^{(i)}, \sigma_{13}^{(i)}, \sigma_{23}^{(i)}, \sigma_{33}^{(i)}$. Now, in terms of (2-30), we may find the other three strain components $\varepsilon_{13}^{(i)}, \varepsilon_{23}^{(i)}, \varepsilon_{33}^{(i)}$. Transferring the strains $\{\bar{\varepsilon}_i\}$ to weaver axes we obtain the weaver strains in local material coordinates:

$$\left\{\bar{\varepsilon}_i^{w_j}\right\}=\left[\bar{R}_i^{w_j}\right]\left\{\bar{\varepsilon}_i\right\} \tag{2-31}$$

Then the weaver stresses can be expressed as:

$$\left\{\sigma_i^{w_j}\right\}=\left[E_i^{w_j}\right]\left(\left\{\varepsilon_i^{w_j}\right\}-\Delta T_i\left\{\alpha_i^{w_j}\right\}-\Delta M_i\left\{\beta_i^{w_j}\right\}\right) \tag{2-32}$$

2.6 The Influence of Fiber Waviness

In woven 3-D composites, nominally straight in-plane yarns, stuffers and fillers, are often much more wavy than those in conventional laminates because of the existence of weaver fibers. The most important effect of tow waviness on elastic properties is to reduce the axial stiffness of a tow. Since the microstructure of a woven composite is highly complex and the waviness of fibers is random rather than possessing a single characteristic wavelength or amplitude, it is not currently practical to model the actual tow geometry. Idealization is mandatory. For simplicity, a composite unit cell with wavy fibers shown in figure 3.4 is analyzed in this section.

To simulate the fiber configuration, the following form of waviness is assumed,

$$y=\frac{4C}{l^2}\left(lx-x^2\right) \tag{2-33}$$

Where l is the half-wavelength and C is the amplitude of waviness. Therefore, the length of yarn $S(l,C)$ can be expressed by

$$S(l,C)=\int_0^l \sqrt{1+y'^2}\,dx$$
$$=\frac{1}{2}\sqrt{l^2+16C^2}+\frac{1}{16}\frac{L^2}{C}\left[\ln\left(\sqrt{1+\frac{16C^2}{l^2}}+\frac{4C}{l}\right)-\ln\left(\sqrt{1+\frac{16C^2}{l^2}}-\frac{4C}{l}\right)\right] \tag{2-34}$$

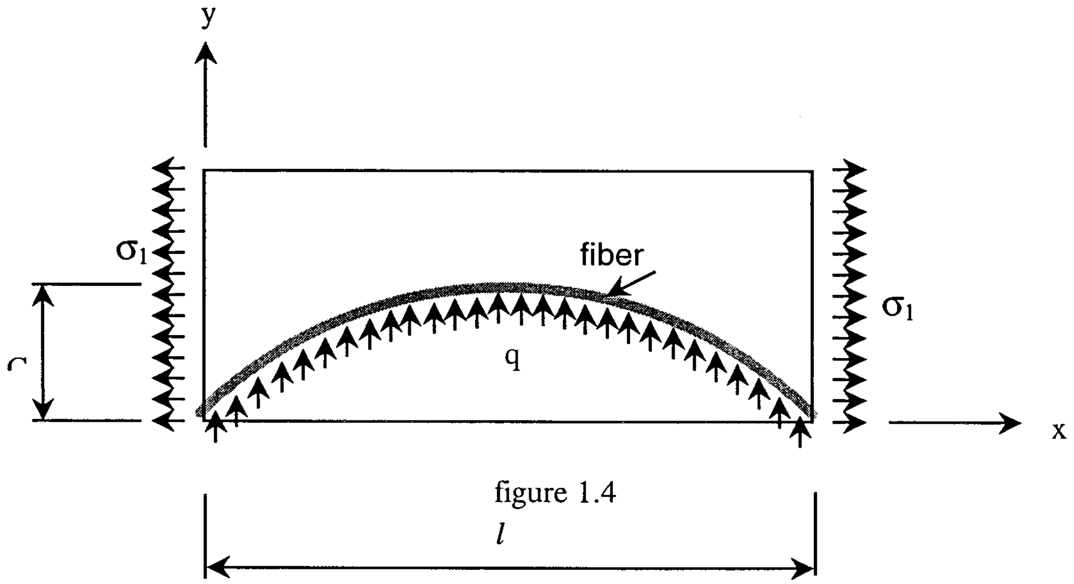

Figure 2.4 Wavy tow model for analyzing the influence of fiber waviness on longitudinal stiffness of unidirectional composites

Supposing that the composite unit sustains axial tensile load σ_l as shown in figure 2.4, the extension of the unit in the X direction is caused by two parts: one is due to fiber axial extension under axial tensile load, and the second is due to the reduction of fiber waviness, i.e. the fiber will become more straight under the axial tensile load, and therefore, additional extension will occur to the composite unit. Since the first component has been widely studied in the literature, this section is focused on the second component--the extension due to the reduction of fiber waviness. Fiber axial extension is not taken into account when considering the second component contributing to composite extension. Therefore, it is reasonable to assume that the length of fiber yarn remains unchanged, i.e. $S(l,C)$ is constant when analyzing the second component of extension. When the fiber waviness reduces, the amplitude C decreases and the wavelength increases.

Since $S(l,C)$ is constant, one may write

$$S(l,C)=\frac{\partial S}{\partial l}\delta l+\frac{\delta S}{\delta C}\delta C=0$$

Therefore the change in composite length becomes:

$$\delta l=-\left(\frac{\partial S}{\partial C}\Big/\frac{\partial S}{\partial l}\right)\delta C=-F(l,C)\delta C \qquad \text{(2-35)}$$

Where

$$F(l,C)=\frac{\dfrac{\sqrt{l^2+16C^2}}{2C}+\dfrac{16C}{\sqrt{l^2+16C^2}}-\dfrac{l^2}{16C^2}\left[\ln\left(\sqrt{1+\dfrac{16C^2}{l^2}}+\dfrac{4C}{l}\right)-\ln\left(\sqrt{1+\dfrac{16C^2}{C^2}}+\dfrac{4C}{l}\right)\right]}{\dfrac{1}{2}\sqrt{1+\dfrac{16C^2}{l^2}}-\dfrac{l}{8C+\sqrt{l^2+C^2}}-\dfrac{4C^2}{l\sqrt{l^2+16C^2}}+\dfrac{l}{8C}\left[\ln\left(\dfrac{4C}{l}+\sqrt{1+\dfrac{16C}{l^2}}\right)-\ln\left(\sqrt{1+\dfrac{16C^2}{C^2}}-\dfrac{4C}{l}\right)\right]} \qquad \text{(2-36)}$$

Assuming the original length of the composite unit is l_0, after the axial load is applied, the length increases to l, then extension of the unit can be expressed by

$$l-l_0=\frac{\sigma_1}{E_{11}^0}l_0+\delta l \qquad \text{(2-37)}$$

Where E_{11}^0 is the composite longitudinal modulus based on orientation averaging method. $\frac{\sigma_1}{E_{11}^0} l_0$ is the extension due to fiber axial extension, δl is the extension due to reduction of fiber waviness.

When the composite unit cell is subjected to tensile load $T_C = \sigma_1 A_C$, the fiber bundle is subjected a tensile force $T_f = \sigma_f A_f$. Since the fiber bundle is not straight, there must be balancing reaction q as shown in figure 2.4 to counteract the vertical component of T_f. According to equilibrium equation, q can be written as

$$q = -\sigma_f A_f \frac{d^2 y}{d^2 x} = \frac{8C}{l^2} \sigma_f A_f \tag{2-38}$$

Where σ_f is the longitudinal stress in the fiber and A_f is the cross section area of the fiber.

The compressive stress in the composite unit cell in Y direction due to q can be expressed by $\sigma_2 = \frac{q}{T} = E_{22}^0 \varepsilon_2 = E_{22}^0 \frac{\delta y}{y} = -E_{22}^0 \frac{\delta C}{C}$ (2-39)

where σ_2 is transverse stress due to q, ε is transverse strain due to q, T is the thickness of the composite, and E_{22}^0 is transverse modulus of the composite.

Substituting q from (2-39) to (2-38), we obtain

$$\frac{8C}{l^2} \sigma_f A_f = -\frac{E_{22}^0 T \delta C}{C} \tag{2-40}$$

and

$$\delta C = -\frac{8C^2\sigma_f A_f}{E_{22}^0 l^2 T} \tag{2-41}$$

Assuming the composite and the fiber bundle have the same strain in the X direction,

$$\sigma_f = \frac{E_f}{E_{11}^0}\sigma_0$$

If fiber volume fraction is denoted as V_f , then

$$A_f = A_0 V_f = CTV_f \tag{2-42}$$

Therefore, (2-34) can be rewritten as

$$\delta C = -\frac{8C^3 E_f \sigma_0 V_f}{E_{11}^0 E_{22}^0 l^2} \tag{2-43}$$

Effective strain ε_1 can be expressed as

$$\begin{aligned}\varepsilon_1 &= \frac{l-l_0}{l_0}\\ &= \frac{1}{l}\left(\frac{\sigma_1}{E_{11}^0}l + F(l,C)\delta C\right)\\ &= \frac{1}{l}\left(\frac{\sigma_1}{E_{11}^0}l + \frac{8C^3 E_f \sigma_1 L_0 V_f F(l,C)}{E_{11}^0 E_{22}^0 l^2}\right)\end{aligned} \tag{2-44}$$

Therefore

$$E_{11} = \frac{\sigma_1}{\varepsilon_1} = KE_{11}^0 \tag{2-45}$$

where K is a knockdown factor of longitudinal modulus for the composite,

$$K = \frac{1}{1 + \frac{8C^3 E_f V_f F(l,C)}{E_{22}^0 l^3}} \tag{2-46}$$

Equation (2-46) can be used to estimate the waviness knockdown factor for misoriented unidirectional composite segments with axially loaded wavy tows. The value of K is less than one and depends on the ratios of C/l and E_f / E_{22}^0. The larger the C/l and/or E_f / E_{22}^0, the smaller the K.

Chapter 3

Prediction of 3-D Woven and Braided Composite Properties

This chapter outlines a preliminary implementation of the 3-D composite mechanics module. Elastic properties and stress limits of three-dimensionally reinforced fiber composites are evaluated. Fiber orientations of weave and braid patterns are defined with reference to composite structural coordinates. Orthotropic ply properties and stress limits computed via micromechanics are transformed to composite structural coordinates and integrated to obtain the 3-D properties. Various composites and fiber reinforcement patterns are considered. Results are compared with experimental data from the literature.

3.1 Methodology

A composite mechanics module was implemented to compute the elastic properties and stress limits of general 3D fiber composites. The implementation uses micromechanics modules to evaluate intraply hybrid composite properties. The intraply properties are computed separately for each fiber orientation present in the 3D braided/woven composite. The assembly of 3D braided composite properties is accomplished by rotating for each braid the stress-strain relations from the local coordinate axis of the braid into the structural coordinate system of the 3D composite via tensor transformations. The local coordinate axis of a braid is taken with the x axis along the fiber direction of the braid. For each braid orientation, the computational module input file is modified to define the direction of the braid x axis by inputting the angles made by the braid axis with the three global composite structural coordinates. Unless the local x axis is in the global z direction, the local y axis of the braid is determined in the direction of the cross product of the global z axis and the local x axis. If the local x-axis is in the global z direction, the local y axis is taken to be in the direction of the cross product of the local x axis by the global x axis. The local z axis is determined by taking the cross product of local x and local y directions. Components of the unit vectors of braid local coordinates written with respect to the composite structural coordinates define the coefficients of the braid orientation matrix, see chapter 2 for details.

The properties of each braid are transformed to the structural directions as described in the previous chapter, multiplied by the ratio of fibers in that braid to the total composite fibers, and superimposed onto the 3D composite properties. When the contribution of each braid is added, composite structural properties are obtained. Fiber volume ratios may be different for each braid orientation as specified by different material cards in the input file. Also, different fibers may be selected for different braids and laminae. Results indicate the implemented method is consistent with published results [Cox and Dadkhah, 1995]. There remain some differences between the computed elastic properties and experimental data. These may be attributed to the effect of residual stresses from the curing process as well as the waviness of fibers.

The fundamental distinction of the present method is that the augmented composite mechanics code is also able to compute the 3D composite stress limits by accumulating the contribution of each braid/weave/ply to each composite strength component via tensor transformations of local strengths in the absolute value. The stress limits in the composite structural coordinates corresponding to first ply failure (FPF) are written in general as:

$$\{S_{C\pm}\}=\sum_{j=1}^{N_w} f_{w_j}\left[Abs\left(R_{w_j}\right)\right]^T\{S_{w_i\pm}\}$$

Where $S_{C\pm}$ are the positive or negative stress limits in the composite structural coordinate directions; $S_{w_i\pm}$ are the stress limits in the local coordinate system of each braid or ply; and $\left[Abs\left(R_{w_j}\right)\right]$ is the property rotation matrix taken in absolute value. In composite strength computations, the fiber and matrix contributions are considered separately to enable the representation of matrix damage that degrades the composite properties prior to fracture. Each of the three composite normal stress limits are computed in both tension and compression. At the stage of matrix damage initiation, tensile stress limits consider the contribution of all components except for fiber tensile strength. On the other hand, in computing the composite tensile fracture strengths, only the contribution of fiber strengths are considered. Compressive normal stress limits are also computed both with reference to matrix crushing as well as with regard to fiber fracture. Similarly, shear strengths with reference to the three global structural axes are obtained by the accumulation of absolute tensor transformations of braid shear strengths as well as the relevant normal strength contributions. In the computation of shear strengths, the appropriate normal strength components are the compressive strength in the braid longitudinal directions and tensile strengths in the braid transverse directions. For each one of the eleven specimens considered, the computed elastic properties and the composite stress limits are tabulated in Appendix B. The computed components of strength the names of which end with the letter "f" correspond to the stress limits for fiber fracture at the absence of matrix degradation in the composite. On the other hand, strength components that are assigned names ending with the letter "m" indicate the matrix damage initiation stresses. Any general 3D composite structure with arbitrary fiber orientations can be analyzed for stress limits as well as composite elastic properties. For the woven composite examples considered in this chapter, the x axis is taken in the direction of the stuffer fibers, the y axis is taken in the direction of the filler fibers, and the z axis is taken in the normal direction. Warp fibers are in various different directions depending on the specimen considered.

3.2 Results and Discussion

The developed method was tested by simulating an experimental study on eleven woven composite structures (Cox and Dadkhah 1995). Of the eleven specimens five were lightly compacted with fiber volume ratio of approximately 0.35 whereas the remaining six were heavily compacted with fiber volume ratios of approximately 0.60. The specimens were designated as indicated and described in Table 3.1.

Table 3.1 Designation of Woven Composite Types

SYMBOL	DESCRIPTION
LL	Lightly Compacted Layer-to-layer Angle Interlock
LT	Lightly Compacted Through-the-thickness Angle Interlock
LO	Lightly Compacted Through-the-thickness Orthogonal Interlock
HL	Heavily Compacted Layer-to-layer Angle Interlock
HT	Heavily Compacted Through-the-thickness Angle Interlock
HO	Heavily Compacted Through-the-thickness Orthogonal Interlock

Table 3.2 shows the fiber volume ratios for the different tows of each specimen. Appendix A shows the properties of fibers and matrices which were used in this simulation. The stuffer and filler fibers were made of AS graphite for all specimens. The LL and LT woven composite types each contained two specimens of which one had warp weaver fibers made of graphite and the other had warp weaver fibers made of glass. All fibers were made of graphite for the heavily compacted composites. Each type of heavily compacted weave pattern had two specimens with different ratios of the stuffer/filler/warp weaver fiber ratios.

The implemented composite mechanics module was able to predict 3D composite properties and stress limits consistently. The computed results for all eleven specimens are presented in tabular form in Appendix B. The present results are compared with those computed by Cox and Dadkhah and those obtained from experiments. In the majority of cases the new module evaluated the 3D stiffness properties closer to experimental measurements compared to the orientation averaging method reported by Cox and Dadkhah. However, in the direction of filler yarns, stiffness computations by the extended code, as well as those computed by Cox and Dadkhah (1995), were considerably higher than the experimentally measured values. Composite stress limits based on fiber strength and matrix strength computed by the composite mechanics code were always able to provide upper and lower bounds, respectively, to the experimental failure strengths.

The availability of the present 3D composite analysis method enables the assessment of damage tolerance, as well as structural response evaluation of braided and woven composites. However, the developed methods can be further improved by quantifying the effects of tow waviness on composite structural response and stress limits. Also, the alternative formulation proposed in the previous chapter that preserves the spatial configurations of individual stuffer and filler tows may be more appropriate for composites subjected to bending.

Table 3.2 Fiber Volume Fraction of Specimens Considered

	Specimen Thickness	Nominal Volume Fractions			Total Fiber Volume Fraction [e]	Fraction by Volume of all Fibers Lying in Stuffers , Fillers, Wrap Weavers [f]		
Composite	(cm)[a]	V_s[b]	V_f[c]	V_w[d]	V	f_s	f_f	f_w
l-L-1	1.26	0.14	0.15	0.07	0.35±0.03	0.385	0.418	0.197
l-L-2	1.24	0.14	0.20	0.05	0.370±0.005[g] 0.066±0.004[h]	0.347	0.502	0.151
l-T-1	1.02	0.16	0.21	0.05	0.466±0.003	0.381	0.504	0.115
l-T-2	0.97	0.18	0.22	0.04	0.408±0.020[g] 0.044±0.004[h]	0.406	0.497	0.097
l-O	0.88	0.18	0.25	0.04	0.483±0.010	0.387	0.524	0.090
h-L-1	0.561	0.38	0.22	0.05	0.620±0.008	0.587	0.340	0.073
h-L-2	0.625	0.33	0.21	0.025	0.557±0.015	0.580	0.375	0.045
h-T-1	0.573	0.37	0.22	0.065	0.613±0.003	0.571	0.331	0.098
h-T-2	0.577	0.36	0.23	0.035	0.592±0.014	0.571	0.369	0.059
h-O-1	0.579	0.37	0.22	0.045	0.619±0.008	0.586	0.340	0.073
h-O-2	0.587	0.35	0.23	0.065	0.593±0.014	0.545	0.353	0.102

- [a] in direction normal to wrap and weft direction
- [b] V_s = volume of fraction of stuffer (straight wrap) twos
- [c] V_f = volume of fraction of filler (weft) tows
- [d] V_w = volume fraction of wrap weaver (3D warp) tows
- [e] measured by acid digestion
- [f] determined from weaver's specification
- [g] graphite fibers
- [h] glass fibers

Chapter 4

Damage Propagation in 3-D Woven Composite Structures

The design evaluation of composite structures requires an assessment of their safety and durability under service loads and possible overload conditions. The ability of designing composites with numerous possible fiber orientation patterns, choices of constituent material combinations, tow/ply drops and hybridizations, render a large number of possible design parameters that may be varied for an optimal design. The multiplicity of composite design options presents a logistical problem, prolonging the design and certification process and adding to the cost of the final product. It is difficult to evaluate composite structures due to the complexities in predicting their overall congruity and performance, especially when structural degradation and damage propagation take place. The predictions of damage initiation, damage growth, and propagation of fracture are important in evaluating the load carrying capacity, damage tolerance, safety, and reliability of composite structures. Quantification of the structural fracture resistance is also fundamental for evaluating the durability/life of composite structures. The most effective way to obtain this quantification is through integrated computer codes that couple composite mechanics with structural analysis and damage progression modeling.

An important feature of computational simulation is the assessment of damage stability or damage tolerance of a structure under loading. At any stage of damage progression, if there is a high level of structural resistance to damage progression under the service loading, the structure is stable with regard to fracture. The corresponding state of structural damage is referred to as stable damage. On the other hand, if damage progression does not encounter significant structural resistance, it corresponds to an unstable damage state. Unstable damage progression is characterized by very large increases in the amount of damage due to small increases in loading. Whereas during stable damage progression the amount of increase in damage is consistent with the increase in loading.

Internal damage in composites is often initiated as cracking due to normal stresses transverse to fiber orientation. Further degradation is in the form of additional cracking, delaminations, and fiber fractures that may lead to structural fracture. Because of the numerous possibilities with material combinations, composite geometry, fiber orientations, and loading conditions, it is essential to have an effective computational capability to predict the behavior of composite structures for any loading, geometry, composite material combinations, and boundary conditions. The predictions of damage initiation, growth, accumulation, and propagation to fracture are important in evaluating the load carrying capacity and reliability of composite structures. Quantification of the structural fracture resistance is also required to evaluate the durability/life of composite structures.

The behavior of laminated composite structures under various loading condition is studied in Minnetyan et al. (1990-1995). The proposed research will extend the scope of a computational tool that has been developed to examine the progressive damage response of conventional laminated fiber composites to the evaluation of 3-D woven composite structures. This integrated computational tool can effectively be broken into three main modules:

1. A micromechanics and macromechanics module of 3D composites.
2. A structural analysis module.
3. A damage progression tracking module.

Details of the first module are discussed in the previous chapter. This chapter discusses the second and third modules.

4.1 Structural Analysis Module

The main tool of the structural analysis module is the finite element method. After the micromechanics analysis module generates the elastic properties for 3-D woven composite, a finite element analysis module is called to analyze the entire structural response based on the composite properties. In general, the type of finite element model used depends on the complexity of the structure and the availability of computer resources. There are two possible choices for the analysis of composite structures. One is using anisotropic 3-D solid elements (such as hexahedral or brick elements) that accept the computed 3-D composite properties directly. However, the modeling of a practical composite structure with three dimensional finite elements requires huge computer memory and CPU time and it is usually impractical for analyzing real structures. The second option is to use anisotropic shell elements that use the composite plate/shell element properties obtained in the previous chapter. Anisotropic plate or shell elements represent through-the-thickness properties of the three-dimensional composite and therefore are much more efficient compared to three dimensional elements. Therefore, implementation is focused on the use of plate/shell elements in the finite element analysis module. The finite element module accepts the 3-D woven composite force-deformation relations predicted by the composite macromechanics module, and carries out a stress analysis to generate the generalized stresses Nx, Ny, Nxy, Mx, My, Mxy for each node. The generalized stresses are supplied back to the composite mechanics module for the computation of local stresses in the primary and weaver domains and failure analysis.

4.2 Failure Criteria

Progressive damage and fracture simulations will be carried out by imposing failure criteria locally within each micromechanics subvolume. Micromechanics subvolumes will be obtained by subdividing each micromechanics volume into regions with characteristic fiber configuration. Within each subvolume local coordinate orientation in the material directions will be identified. At each individual load step, the stuffer, filler, and weaver stresses and strains obtained through 3D woven composite microstress analysis are to be checked according to distinct failure criteria. The first twelve failure modes are associated with the positive and negative limits of the six local stress components in the material direction as follows:

$$S_{\ell 11C} < \sigma_{\ell 11} < S_{\ell 11T}$$

$$S_{\ell 22C} < \sigma_{\ell 22} < S_{\ell 22T}$$

$$S_{\ell 33C} < \sigma_{\ell 33} < S_{\ell 33T}$$

$$S_{\ell 12(-)} < \sigma_{\ell 12} < S_{\ell 12(+)}$$

$$S_{\ell 23(-)} < \sigma_{\ell 23} < S_{\ell 23(+)}$$

$$S_{\ell 13(-)} < \sigma_{\ell 13} < S_{\ell 13(+)}$$

The thirteenth failure mode is a combined stress failure criterion, or modified distortion energy (MDE) failure criterion which is obtained by modifying the usual distortion energy failure criterion. The modification takes into account the significant differences in the stress limits of the longitudinal and transverse directions of an orthotropic composite ply. Each component of ply stress is normalized with respect to its limiting strength. No relationship is assumed between normal and shear strengths. The MDE failure criterion has been demonstrated to be a good predictor of combined stress failure in composites. It may be considered as a variation of the Tsai-Hill theory (Tsai 1968, Hill 1950). The MDE failure criterion (Chamis 1969) can be expressed as:

$$\left(\frac{\sigma_{\ell 11\alpha}}{S_{\ell 11\alpha}}\right)^2 + \left(\frac{\sigma_{\ell 22\beta}}{S_{\ell 22\beta}}\right)^2 - K_{\ell 12\alpha\beta}\frac{\sigma_{\ell 11\alpha}}{S_{\ell 11\alpha}}\frac{\sigma_{l22\beta}}{S_{l22\beta}} + \left(\frac{\sigma_{\ell 12S}}{S_{\ell 12S}}\right)^2 < 1$$

where α and β indicate tensile or compressive stresses, $S_{\ell 11\alpha}$ is the local longitudinal strength in tension or compression, $S_{\ell 22\alpha}$ is the transverse strength in tension or compression, and the directional interaction factor is defined as:

$$K_{\ell 12\alpha\beta} = K'_{\ell 12\alpha\beta} \frac{(1+4\upsilon_{12}-\upsilon_{13})E_{22}+(1-\upsilon_{23})E_{11}}{\left[E_{11}E_{22}(2+\upsilon_{12}+\upsilon_{13})(2+\upsilon_{21}+\upsilon_{23})\right]^{1/2}}$$

where $K'_{\ell 12\alpha\beta}$ is a theory-experiment correlation factor.

The directional interaction factor reduces to unity for homogeneous isotropic materials.

4.3 Simulation of Damage Progression

After each finite element stress analysis, failure criteria will be used to evaluate possible failure at each primary and weaver domain of each ply at each node of the composite structure. Once the damage at each node is assessed, a damage index will be created to record the damage information for each damaged node. The damage index will contain the node number, the ply number, and the list of damage criteria that have become activated. When a new failure occurs at certain stuffer, filler, or weaver domain, the damage index will be updated correspondingly. The properties of each domain will be degraded according to their damage index.

If there is no damage after a load increment, the structure will be considered to be in equilibrium and an additional load increment will be applied. Figure 4.1 shows a schematic of damage tracking, expressed in terms of a load-displacement relationship. Point 1 represents the last equilibrium state before initial damage. When the structure is loaded by an additional load increment to point 2, ply failure criteria indicate damage initiation. The composite properties affected by the damage are degraded, the computational model is reconstituted with updated finite element mesh and material properties, and the structure is reanalyzed under the same load increment to reach point 3. However, at point 3, composite ply criteria indicate additional damage. Accordingly, structural properties are further degraded and analysis is repeated under the same load increment to reach point 4. There is no further damage at point 4 and the structure is now considered to be in equilibrium with the external loads. Since the structure is now in equilibrium, a new load increment is applied to reach point 5. At this point, the process of checking the failure criteria, updating the finite element mesh, and updating the material properties is repeated with possible damage growth and propagation.

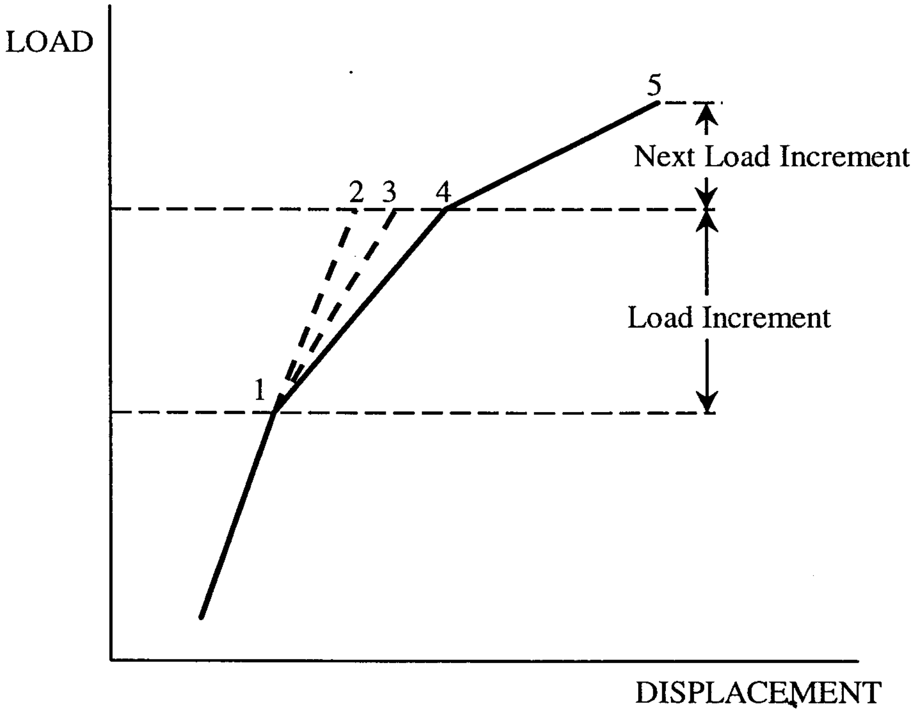

Figure 4.1 Schematic of damage tracking of woven composites

The damage progression module keeps a detailed account of composite degradation for the entire structure and also acts as the master executive module that directs the composite mechanics module to perform micromechanics, macromechanics, laminate analysis and synthesis functions. The damage progression module also calls the finite element analysis module with thick shell analysis capability to model laminated composites for global structural response. A schematic of the simulation cycle is shown in Figure 4.2.

4.4 Damage Energy Release Rate

The measure of global fracture toughness is defined as a Damage Energy Release Rate (DERR) that is equal to the incremental amount of damage energy expanded for the creation of unit damage volume in the composite structure. The magnitude of the DERR varies during progressive degradation of the composite structure under loading, reflecting the changes in the fracture toughness of the composite. Computation of DERR during progressive fracture is needed in order to evaluate the composite fracture toughness and the degree of imminence of failure.

The DERR is computed as the ratio of incremental damage energy to the corresponding incremental damage volume that is generated.

$$DERR = \frac{Damage\,Energy}{Damage\,Volume}$$

Damage energy can be computed as follows:

$$Damage\,Energy = \sum_i \sum_j \left(0.5 S_j^2 / E_j\right) V_i$$

Where S_j is a local composite strength, E_j is modulus corresponding to S_j, V_i is the volume of damage. The traverse of a local minimum value by the DERR during the progression of fracture typically precedes a very high rate of damage propagation and generally predicts the imminence of total failure. Typically, at the stage of damage initiation, there is a high rate of energy release that dissipates a significant portion of the strain energy stored in the composite structure before the onset of initial damage. After the first burst of energy release, DERR usually drops down to a lower level, indicating the significant reduction in fracture stability of the damaged composite under the applied loading. The DERR usually reaches its peak value as global failure occurs.

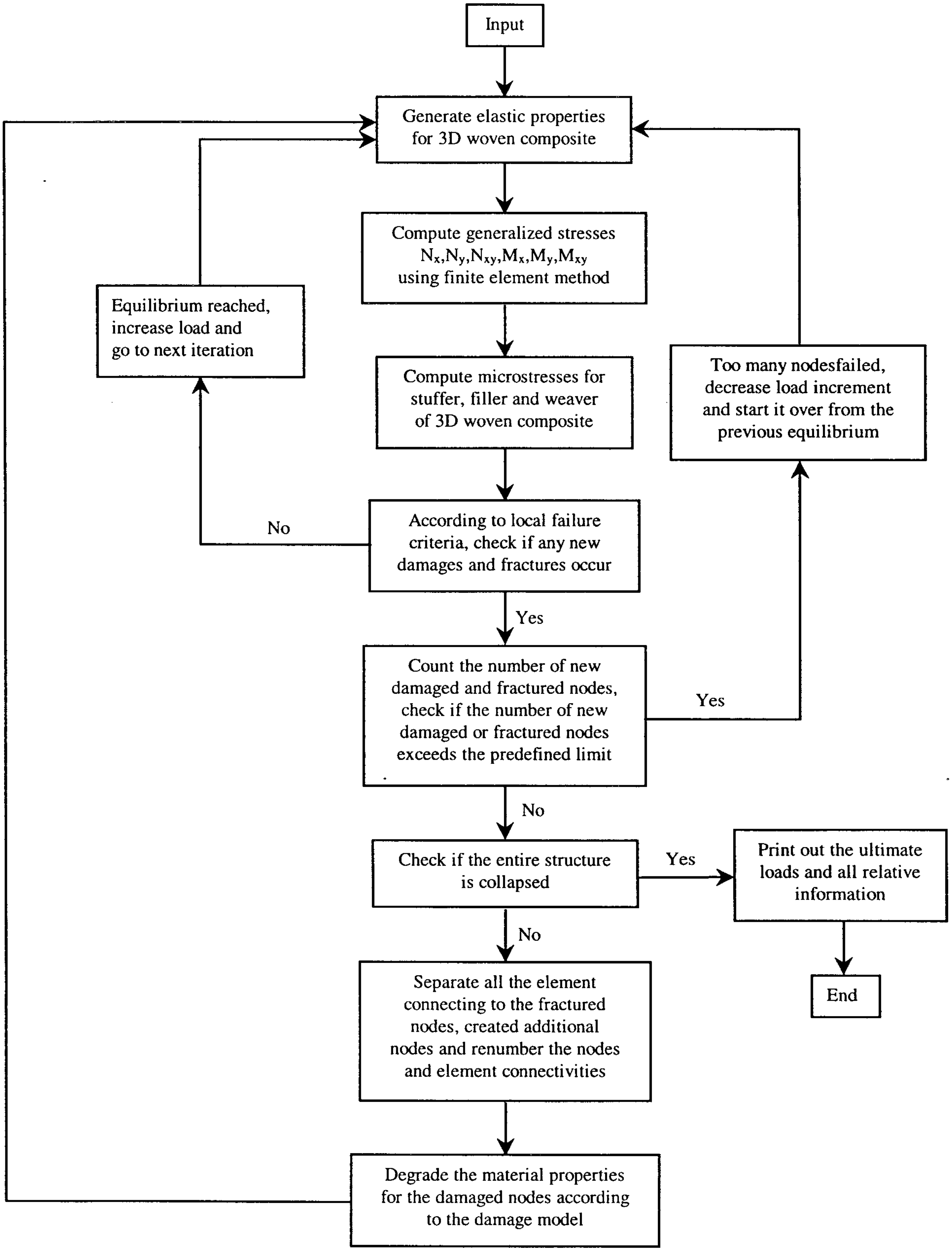

Figure 4.2 Flow chart of integrated computer code for simulating damage propagation of 3D woven composites

Chapter 5

DAMAGE PROGRESSION IN CARBON-FIBER PLASTIC I-BEAMS

5.1 Introduction

For a rational design, it is necessary to quantify the defect and damage tolerance of a candidate structure. The assessment of damage tolerance requires a capability to simulate the progressive damage and fracture characteristics of structures under loading. Critical components of a structure are required to remain safe and to be able to function under loading after experiencing some damage. The cause of damage may be an accident, defect, or unexpected overloading. Damage tolerance of a structure is quantified by the residual strength; that is, the additional load carrying ability after damage. Composite structures are well suited for design with emphasis on damage tolerance because continuous fiber composites have the ability to arrest cracks and prevent self-similar crack propagation. For most fiber reinforcement configurations, cracks and other stress concentrators do not have as important an influence on composites as they do for homogeneous materials. Another important factor is the multiplicity of design options for composites. The ability of designing composites with numerous possible fiber orientation patterns, choices of constituent material combinations, ply drops, and hybridizations render a large number of possible design parameters that may be varied for an optimal design.

Graphite/epoxy composites are used in various retrofit and original construction projects, as well as other structural applications such as aircraft structures, automotive vehicles, pressurized containers, special purpose enclosure structures, and so on. In most applications it is important to achieve low weight, high strength, adequate stiffness, and safety when composite structures are required to withstand significant loads. In the current study, discussion is focused on composite beams formed into a structural shape subject to three-point bending. Damage initiation, growth, accumulation, propagation to fracture, and buckling stability are evaluated. The damage initiation load and the maximum structural fracture load or the buckling instability load are quantified for three different laminate configurations.

Design considerations with regard to the progressive fracture of composite structures require an evaluation of damage initiation and propagation mechanisms under expected service loading. Concerns for safety and survivability of critical components require a quantification of the structural fracture resistance under sustained loads. A significant design parameter with regard to composite damage tolerance is the laminate configuration. In general, quasi-isotropic laminates yield better damage tolerance. However, in many cases, a quasi-isotropic laminate may not be the most efficient with regard to structural strength and performance when there is no damage. For a rational design process, it is necessary to quantify the structural damage tolerance for a candidate design. Damage initiation and progression characteristics are much more complex for laminated fiber composites compared to homogeneous or orthotropic materials. The structural fracture process of a laminated composite depends on many parameters such as laminate configuration, fiber volume ratio, constituent stiffness/strength/hygrothermal parameters, and the fabrication process. Recent developments in computational simulation technology have made it possible to evaluate the details of progressive damage and fracture in composite structures. Computational simulation enables assessment of the damage initiation and propagation loads. A damage energy release rate is evaluated globally during simulation by computing the work done by the applied loads per unit damage created. The damage energy release rate is used to quantify the structural damage tolerance at different stages of degradation. The influence of local defects or flaws, through-the-thickness cracks, and effects of the fabrication process in terms of residual stresses can be taken into account.

Laminated composite design practice has been based on extensive testing with attempts to apply formal fracture mechanics concepts to interpret test results. In certain cases, interpretation of composite test data via fracture mechanics has been satisfactory. However, in most cases, fracture mechanics methods have significantly mispredicted the strength of fiber composites. Reconciliation of test results with fracture mechanics has required significant modifications of effective fracture toughness and the calibrations of specific, laminate configuration dependent, effective stress concentration field parameters. Additionally, required adjustments of fracture mechanics parameters have had to be reassessed with every change in constituent and laminate characteristics. The complete evaluation of laminated composite fracture requires an assessment of ply and subply level damage/fracture processes.

The present approach bypasses traditional fracture mechanics to provide an alternative evaluation method, conveying to the design engineer a detailed description of damage initiation, growth, accumulation, and propagation that would take place in the process of ultimate fracture of a fiber composite structure. Results show in detail the damage progression sequence and structural fracture resistance during different degradation stages. This study demonstrates that computational simulation, with the use of established material modeling and finite element modules, adequately tracks the damage growth and subsequent propagation to fracture for carbon-fiber reinforced plastic (CFRP) composite I-beams subjected to three point bending.

5.2 Methodology

An integrated computer code has been developed to simulate damage initiation, damage growth, and fracture in composite structures under various loading and environmental conditions (Chamis et al. 1996). Computational simulation has been used for the investigation of the effects of composite degradation on structural response (Minnetyan et al. 1991), composite structures' global fracture toughness (Minnetyan et al. 1990), the effect of the hygrothermal environment on durability (Minnetyan et al. 1992b), damage progression in composite shells subjected to internal pressure (Minnetyan et al. 1992a), damage of composite cylinders subjected to mechanical loads as well as internal pressure

(Gotsis et al. 1996), the behavior of discontinuously stiffened composite panels under compressive loading (Minnetyan et al. 1995), and damage propagation in thick composite shells under external pressure (Minnetyan and Chamis, 1997). The present paper examines damage and fracture progression in CFRP I-beams with three different layups.

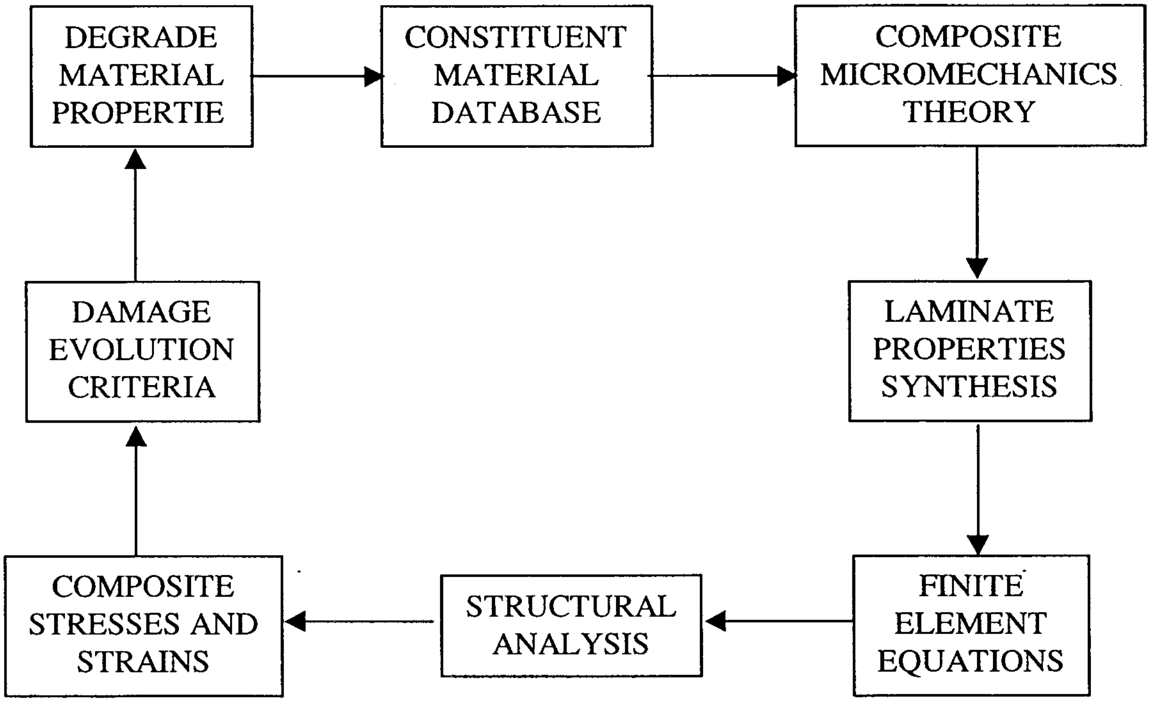

Figure 5.1 Computational Simulation Cycle

The developed computer method consists of an integrated code with three modules: (1) composite mechanics; (2) finite element analysis; and (3) damage progression modeling. The overall evaluation of composite structural durability is carried out in the damage progression module that keeps track of composite degradation for the entire structure. The damage progression module relies on a composite mechanics code (Murthy and Chamis, 1986) for composite micromechanics, macromechanics, and laminate analysis, and calls a finite element analysis module that uses anisotropic thick shell elements to model laminated composites.

Figure 5.1 shows a schematic of the computational simulation cycle. The composite mechanics module is called before and after each finite element analysis. Prior to each finite element analysis, the composite mechanics module computes the composite properties from the fiber and matrix constituent characteristics and the composite layup. The finite element analysis module accepts the composite properties that are computed by the composite mechanics code at each node and performs the analysis at each load increment. After an incremental finite element analysis, the computed generalized nodal force resultants and deformations are supplied to the composite analysis module that evaluates the nature and amount of local damage, if any, in the plies of the composite laminate. Individual ply failure modes are assessed by using failure criteria associated with the negative and positive limits of the six ply-stress components in the material directions. In addition to the failure criteria based on stress limits, interply delamination due to relative rotation of the plies and a modified distortion energy (MDE) failure criterion that takes into account combined stresses are considered (Murthy and Chamis, 1986). Depending on the dominant term in the MDE failure criterion, fiber failure and/or matrix failure is assigned.

If the dominant term in the MDE failure criterion is ply longitudinal tensile or compressive stress, both fiber and matrix failures are simulated, and the ply stiffness is lowered to a negligible value. On the other hand, if the dominant term in the MDE criterion does not correspond to a longitudinal tensile or compressive failure mode, only the matrix stiffness is reduced for the damaged ply, and the fiber stiffness is retained. A ply that sustains matrix damage is able to carry longitudinal tensile stresses but would fracture

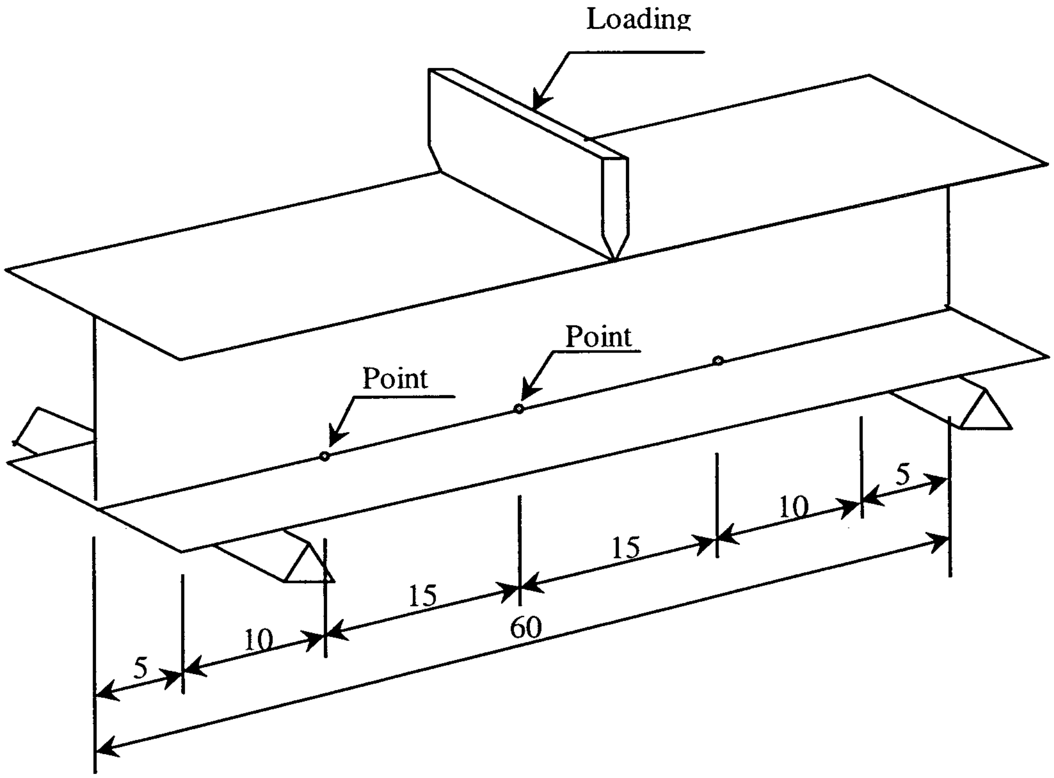

Figure 5.2a CFRP I-Beam and Loading

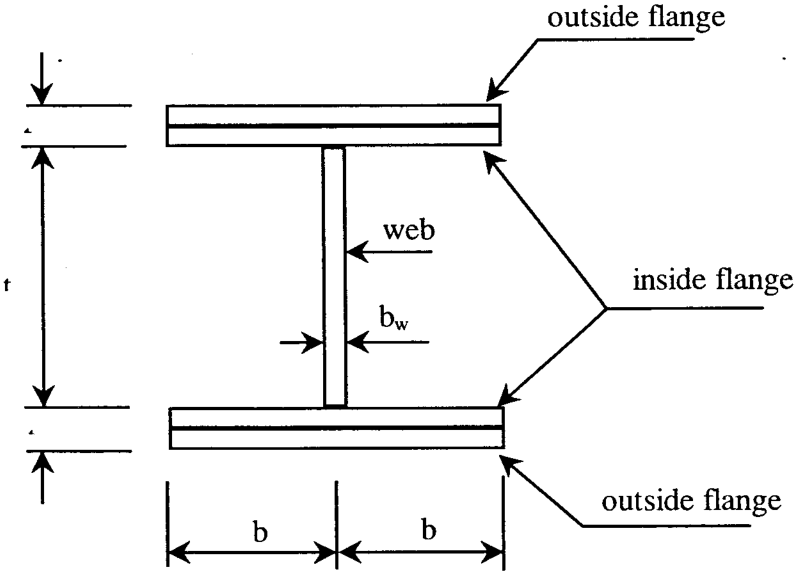

Figure 5.2b Cross Section of CFRP I-Beam

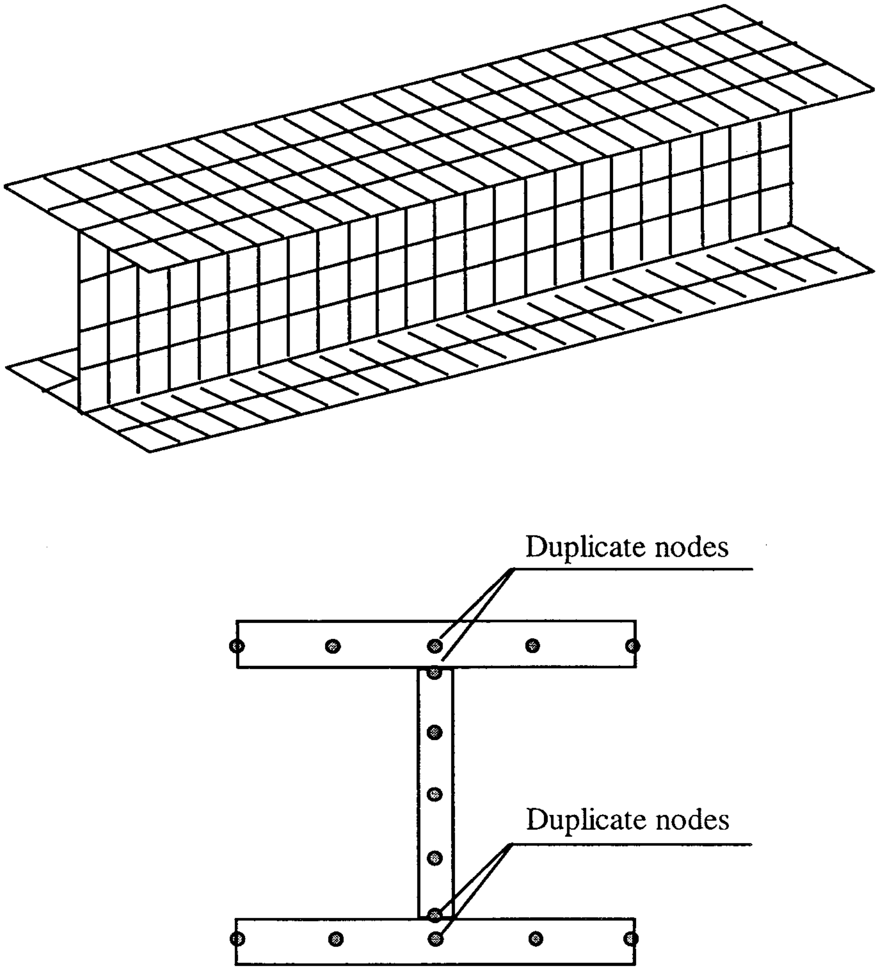

Figure 5.3 Finite Element Model

when subjected to longitudinal compression. The generalized stress-strain relationships are revised locally according to the composite damage evaluated after each finite element analysis. The model is automatically updated with a new finite element mesh having reconstituted properties, and the structure is reanalyzed for further deformation and damage. If there is no damage after a load increment, the structure is considered to be in equilibrium, and an additional load increment is applied, leading to possible damage growth, accumulation, or propagation. Simulation is continued until global structural fracture.

During progressive damage tracking, the following terminology is utilized to describe the various stages of degradation in the composite structure: (1) damage initiation refers to the start of damage induced by loading that the composite structure is designed to carry; (2) damage growth is the progression of damage from the location of damage initiation to other regions; (3) damage accumulation is the increase in the amount of damage in the damaged regions with additional damage modes becoming active; (4) damage propagation is the rapid progression of damage to other regions of the structure; and (5) structural fracture is the ultimate disintegration of the specimen.

5.3 Carbon-Fiber Reinforced Plastic I-Beams

Computational simulation examples in the present paper consist of composite I-beams for which experimental results are available from the published literature. Three types of I-beams from Takayanagi et al. (1994) were simulated. The reported I-beams were fabricated from Toray F3060 (T300/ 3601) prepreg cured at 180°C. The stacking sequences of the I-beams are shown in Table 5.1, and a schematic view of an I-beam is shown in Figure 5.2. The layup for the web and the inside flange was a ±45° angle-ply for all three specimens. The number of plies for the web was 16. The number of plies for the inside flange was eight in all cases. Three different layup schemes for the outside flange were considered. The layup for specimen A was unidirectional (UD), the layup for specimen B was quasi-isotropic (QI), and the layup for specimen C was angle plied (AP) (see Table 5.1 for the precise definitions of UD, QI, and AP laminate configurations). Table 5.2 shows the dimensions for the cross sections of the I-beams with reference to Figure 5.2(b).

Table 5.1 Laminate Stacking Sequence of the CFRP I-Beams

Specimen	Flange		Web
	Outside	Inside	
A	UD: $[0]_8$	AP:$[+45/-45]_4$	AP:$[(\pm 45)_4]_s$
B	QI: $[45/0/-45/90]_2$	AP:$[+45/-45]_4$	AP:$[(\pm 45)_4]_s$
C	AP: $[+45/-45]_4$	AP:$[+45/-45]_4$	AP:$[(\pm 45)_4]_s$

Table 5.2 Dimensions of the Cross-Sections of the CFRP I-Beams

Specimen	b (mm)	b_w (mm)	t_f (mm)	t_w (mm)
A	27.56	2.48	2.10	60.17
B	28.32	2.24	2.00	60.17
C	28.36	2.46	2.06	60.17

A finite element model of the I-beam is shown in Figure 5.3. Mindlin type thick composite shell elements were utilized to represent the through-the-thickness laminates. The upper and lower flanges were uniformly divided into 200 elements each. The web was divided into 250 uniform sized elements. Duplicate nodes were used to represent the connection of the web to the flanges. Figure 5.3 shows the duplicate nodes at a typical section of the I-beam. In the computational model, each pair of duplicate nodes is described by assigning a slave-master relationship that is implemented by eliminating the degrees of freedom of the slave node from the stiffness equations and adding the stiffness contributions from the slave node to those of the master node. During computational simulation of damage progression, if one of the nodes of a duplicate node pair was fractured, the associated duplicate node relationship was terminated.

5.4 Fiber and Matrix Properties Calibration

To enable constituent level damage tracking in the computational simulation, it was necessary to identify the matrix/fiber constituent properties and stress limits. Takayanagi et al. (1994) gave the ply properties, but did not provide explicit information on fiber and matrix properties. The composite mechanics module of this code (Murthy and Chamis 1986) was used to calibrate the fiber and matrix properties so that the computed ply properties matched those of the T300/3601 composite given by Takayanagi et al. (1994). The resident databank of the composite mechanics code provided properties of similar fibers and matrices. Properties of T300 from the databank were used as the initial values of fiber T300, which was used in this study; properties of matrix 3501 (since matrix 3601 was not included in the ICAN databank) were used as initial values for matrix 3601. Using the properties from the databank as initial trial values, ply properties and composite properties were identified via a least squares error sum minimization method.

Ply properties computed by the composite mechanics module were compared with those experimentally observed by Takayanagi et al. (1994). If the differences between the computed and observed ply properties was greater than acceptable, the fiber and matrix properties were revised, and ply properties were recomputed until the actual ply properties were matched with sufficient accuracy. However, because of the natural complexity of the composite material, as well as the uncertainty and variability of experimental observations, it was not possible to obtain computed ply properties that were exactly the same as those experimentally observed. In the present study, the difference between the computed properties and experimental observations was minimized in the root-mean-square relative error sense. The root-mean-square relative error Ω was defined as

$$\Omega=\sqrt{\frac{1}{n}\sum_{i=1}^{n}\left(\frac{P_i^{observed}-P_i^{computed}}{P_i^{observed}}\right)^2}$$

where $P_i^{observed}$ = value of composite property (such as E_{11}, E_{22}, G_{12}, etc.) from experiment; $P_i^{computed}$ = value of same property computed by composite mechanics module; and n = number of composite ply properties observed.

The smaller the value of Ω, the better the agreement between the computed and observed ply properties, and therefore more accurately identified are the fiber and matrix constituent properties. The fiber and matrix properties identified by minimizing Ω are given in Tables 5.3 and 5.4, respectively.

Based on the fiber and matrix properties given in Tables 5.3 and 5.4, the composite properties were computed by the composite mechanics code. Tables 5.5, 5.6, and 5.7 show comparisons of computed and observed composite properties as well as the associated percent relative error Ω.

Table 5.3: Fiber Properties

Parameter	Value
Number of fibers per end	*3000*
Fiber diameter	*0.00762 mm(0.300E-3 in)*
Fiber Density	*1771 kg/m^3 (0.064lb/in^3)*
Longitudinal normal modulus	*197 GPa(28.5E+6 psi)*
Transverse normal modulus	*17.2 GPa(2.5E+6 psi)*
Poisson's ratio ν_{12}	*0.20*
Poisson's ratio ν_{23}	*0.25*
Shear modulus G_{12}	*8.96 Gpa (1.3E+6 Psi)*
Shear modulus G_{23}	*4.82 Gpa (0.7E+6 Psi)*
Longitudinal thermal expansion coefficient	*-0.99E-6°C (-0.55E-6°F)*
Transverse thermal expansion coefficient	*1.01E-6°C (0.56E-5°F)*
Longitudinal heat conductivity	*43.4 J-m/hr/m^2 /°C (580BTU-in/hr/in^2/°F)*
Transverse heat conductivity	*4.34 J-m/hr/m^2 /°C (58BTU-in/hr/in^2/°F)*
Heat capacity	*712 J/kg/°C (0.17 BTU / lb/°F)*
Tensile capacity	*2.41 Gpa (350 ksi)*
Compressive strength	*2.07 GPa (300 ksi)*

able 5.4: Matrix properties:

Parameter	Value
Matrix density	*1265 kg/m^3 (0.0457 lb/in^3)*
Normal modulus	*3.79 GPa ~(550ksi)*
Poisson's ratio	*0.34*
Coefficient of thermal expansion	*0.72E-4/°C (0.4E-4/°F)*
Heat conductivity	*1.25BTU-in/hr/in^2 /°F*
Heat capacity	*0.25 BTU/lb/°F*
Tensile strength	*114 MPa (16.5 ksi)*
Compressive strength	*423 MPa(61.3ksi)*
Shear strength	*148 MPa (21.4ksi)*
Allowable tensile strain	*0.02*
Allowable compressive strain	*0.05*
Allowable shear strain	*0.04*
Allowable torsional	*0.04*
Void conductivity	*16.8 J-m/hr/m^2 /°C (0.225BTU-in/hr/in^2/°F)*
Glass transition temperature	*216°C (420°F)*

Table 5.5 Elastic Constants of the Laminates

Type of Laminate		$E_{11}(GPa)$	$E_{22}(GPa)$	$G_{12}(GPa)$	$\Omega\,(\%)$	$V_f\,(\%)$
UUD	Experimental	100.1	9.12	3.71	5.6	49.8
	Simulated	99.77	8.43	3.49		
QQI	Experimental	40.6	40.6	14.9	4.1	49.4
	Simulated	38.6	38.6	14.7		
AAD	Experimental	11.8	11.8	26.1	4.8	50.3
	Simulated	12.5	12.5	26.3		

Table 5.6 Elastic Constants of the Flange Laminates

Specimen		$E_x\,(GPa)$	$E_y\,(GPa)$	$G_{xy}\,(GPa)$	$\Omega\,(\%)$	$V_f\,(\%)$
AA	Experimental	72.3	13.1	18.6	2.6	62.8
	Simulated	71.2	12.6	18.6		
BB	Experimental	35.5	34.8	27.0	2.6	66.0
	Simulated	35.9	35.9	26.8		
CC	Experimental	15.5	15.5	34.3	2.6	66.1
	Simulated	16.0	16.0	34.3		

Table 5.7 Elastic Constants of the Web Laminates

Specimen		$E_w\,(GPa)$	$G_{wz}\,(GPa)$	$\Omega\,(\%)$	$V_f\,(\%)$
A	Experimental	11.7	25.9	4.24	50.0
	Simulated	12.4	26.1		
B	Experimental	13.8	30.5	2.0	58.7
	Simulated	14.2	30.5		
C	Experimental	12.3	27.1	3.5	52.3
	Simulated	12.9	27.3		

5.5 Results and Analysis

Damage initiation and progression were monitored as the composite I-beam specimens were loaded at midspan. The loading configuration was as shown in Figure 5.2(a). In the computer model, the knife-edge supports were described as follows. For the left end support, bottom flange nodes in contact with the knife-edge support were restrained against translation in the plane of the web (pin supports). Additionally, the bottom flange node immediately under the web was also restrained against translation perpendicular to the plane of the web. For the right end support, all bottom flange nodes in contact with the knife-edge were restrained in the load direction (roller supports). The loading nose was represented by an attached finite element model of a high-strength steel plate that was 20 mm (0.787 in.) thick and 41 mm (1.6 in.) high. The attachment of the steel plate finite elements to the top flange of the beam was described using duplicate node constraints. The load was applied to the top of the loading nose. It was started at 0.20 kN (46 lb) and increased gradually. Specimen A was simulated first. When the load applied on specimen A reached 2.56 kN (575 lb), damage initiation occurred at the midspan of the beam, in the upper flange by matrix tensile failures due to the transverse tensile fracture of the 0° outside plies immediately above the web. Damage grew to adjacent nodes in the transverse direction as the load was increased to 2.74 kN (616 lb). However, the damage mode remained with matrix cracking in the 0° outside plies only. When the load was increased to 6.36 kN (1,430 lb), the upper flange outermost ply under the loading nose developed fiber fractures in the longitudinal compressive failure mode. At 6.81 kN (1,530 lb), ply compressive fiber fractures progressed to the three outermost 0° plies of the top flange. Also, fiber tensile fractures began to occur at the bottom flange at midspan, immediately under the web, in the outermost 0° plies. At 7.65 kN (1,720 lb), all eight plies of the outer top flange experienced compressive failures under the load. At the bottom flange, tensile failures grew to the outermost four plies. At 7.96 kN (1,790 lb) loading, ply compressive fractures grew into through-the-thickness laminate cracks of the upper flange at midspan. First, laminate cracking began at the edges of the top flange; second, the center flange under the loading nose developed cracking; and third, the intermediate nodes between the center and the edges of the top flange were cracked. In the bottom flange, fiber tensile failures progressed across the flange width in the outermost three plies. Damage in the center nodes of the bottom flange remained the same with four fractured plies. As the load was further increased gradually, a damage stabilization stage was entered when the additional damage growth was limited to the accumulation of damage in the previously experienced modes. At 8.99 kN (2,020 lb), two distinct laminate compressive fracture zones were formed on both sides of the loading nose in the top flange. In the bottom flange, 0° ply fiber tensile fractures grew into the five outermost 0° plies under the web, and grew into the four outermost 0° plies at nodes not located directly under the web. Fiber tensile fractures in the flange plies directly under the web were extended for 11 nodes along the beam axis, centered at midspan. Approximately half the clear span length of the beam was affected by tensile fiber fractures in the center of the flange directly under the web. When the load was increased further, compressive laminate cracking began to grow rapidly in the upper flange, and fiber tensile fractures propagated along the beam axis in the bottom flange under the web, causing the total collapse of the beam. Figure 5.4

shows the beam finite element model immediately before collapse when some of the finite elements of the top and bottom flanges have been deleted due to the compressive fracturing of the top flange and tensile fracturing of the bottom flange. The simulated ultimate structural collapse mode was consistent with experimental observations reported in Takayanagi et al. (1994). However, the ultimate collapse mode is merely the final result of complex damage initiation, growth, and propagation characteristics that are determined via computational simulation. The fracture-resistant design of a laminated fiber composite beam requires a thorough evaluation of the damage progression characteristics, as well as the ultimate collapse load and the collapse mode.

Figure 5.5 shows the relationship between load and deflection. The deflection coordinate plotted as the abscissa in Figure 5.5 represents the relative deflection of point A with respect to point B (see Figure 5.2). Experimental data, as well as the modified beam theory and composite beam theory results, shown in Figure 5.5 are from Takayanagi et al. (1994). Simulated displacements via the present method follow composite beam theory results very closely up to a load level of approximately 7 kN. It is noteworthy that the extensive matrix cracking and limited ply compressive failures that occurred prior to reaching the 7 kN load level did not affect the apparent structural response significantly under the monotonically increasing static loading. At 7.65 kN, when the outermost eight 0° plies of the compression flange fractured, a substantial change occurred in the structural response that was observable in the load-deflection relationship. As the peak loading was approached, the simulated load-deflection relationship became more nonlinear compared to the experimentally observed load-deflection curve reported by Takayanagi et al. (1994). This difference may be explained as the effect of additional constraints imposed on the upper flange by the loading yoke, which did not allow the free deformation of the fractured top flange when the loading was increased during testing. Nevertheless, the simulated peak load agrees well with that observed experimentally.

In general, overall structural damage includes ply damage and also through-the-thickness fracture of the composite laminate. Varied and complex composite damage mechanisms are simulated via evaluation of the individual ply failure modes and associated degradation of laminate properties. The type of damage growth and the sequence of damage progression depend on the composite structure, loading, and material properties. A scalar damage variable, derived from the total volume of the composite material affected by the various damage mechanisms, is also evaluated as an indicator of the level of overall damage induced by loading. This scalar damage variable is useful for assessing the overall degradation of a given structure under a prescribed loading condition. The rate of increase in the overall damage during composite degradation may be used as a measure of structural propensity for fracture. The procedure by which the overall damage variable is computed is given by Minnetyan et al. (1990).

Figure 5.6 shows the relationship between load and the damage energy release rate (DERR). The DERR is defined globally as the work done by applied forces, per unit damage produced during structural degradation. The DERR can be used to evaluate structural resistance against damage propagation at different stages of loading. A high DERR level indicates the dominance of global structural characteristics in damage progression. On the other hand, a low DERR level indicates the importance of local material properties on damage progression. The DERR usually starts at a high level at damage initiation. It is gradually lowered during damage growth and accumulation. Near the peak load, DERR rates begin to increase again as the damage propagation stage is entered. The minimum DERR level signals the completion of the damage tolerant structural response stage. From Figure 5.6, the 8.10 kN load corresponding to the minimum value of the DERR indicates that the maximum load for damage tolerance was 8.10 kN (1,820 lb). At 8.10 kN loading, there was some damage stabilization after the formation of through-the-thickness cracks in the top flange. Subsequent to the 8.10 kN load corresponding to minimum DERR, damage propagated more rapidly as the peak load was reached.

Table 5.8 Relative Deflections under 4KN Loading

Specimen	W_{obs} (mm)	W_{MBT} (mm)	W_{CBT} (mm)	W_{COD} (mm)
A	0.384	0.359	0.348	0.346
B	0.616	0.621	0.613	0.631
C	1.136	1.189	1.184	1.163

Table 5.9 Peak Loads of CFRP Beams

Specimen	Failure Mode	Peak Load (KN)	
		Simulation	Experiment
A	Compression flange	9.54	9.20
B	Upper web	13.11	12.78
C	Lateral bucking	11.41	11.82

Figure 5.7 shows the relationship between load and damage. Damage started at 2.56 kN

(575 lb) loading. The amount of damage increased greatly after the load level of 8.10 kN was reached. When the load reached 9.52 kN (2,140 lb), the simulated specimen collapsed as the damage level reached 13.02%. The corresponding experimental collapse load was 9.20 kN (2,068 lb). The experimentally observed peak load was about 3% lower than the simulated peak load.

For specimen B, damage was initiated at the midspan of the top and bottom flanges simultaneously due to matrix tensile failures by the ply transverse tensile failure mode. The damage initiation load was 3.42 kN (776 lb). Damage propagated to 99 nodes as the loading increased to 3.97 kN (893 lb). When the load reached 12.32 kN (2,770 lb), most nodes were damaged and a through-the-thickness crack occurred at the upper middle part of the web due to ply compressive failures, as the reduced number of 0° flange plies caused a larger share of the load to be carried by the web rather than by the flanges. Subsequently, damage propagated to the middle of the upper flange and caused the I-beam to break completely. Figure 5.8 shows the simulated and experimentally observed load-deflection relationships for specimen B. From Figure 5.8, it may be noted that for specimen B the simulated relative deflections between points A and B are in very good agreement with the experimental results. The improved agreement of the simulated results with experimental data for specimen B may be explained by the fact that the quasi-isotropic outside flange laminate of specimen B is less critical than the web, and therefore is less sensitive to the loading and boundary conditions compared to the unidirectional laminate at the outer flange of specimen A.

Due to the lack of 0° plies in the flanges, specimen C was susceptible to large vertical deflections and lateral buckling. A finite element structural stability analysis for specimen

C indicated that lateral buckling would occur under a 11.41 kN (2,565 lb) load. The experimentally observed buckling load for specimen C was 11.82 kN (2,658 lb). Computational simulation indicated that stress-induced composite damage did not occur prior to reaching the buckling of the beam. Specimen C was considerably more flexible compared to specimens A and B. The relative deflections between points A and B (see Figure 5.2), for specimens A, B, and C, under a load of 4 kN, obtained via computational simulation (W_{MBT}), modified beam theory ($W_{CBT,}$), composite beam theory ($W_{CBT,}$), and experimentally observed data (W_{obs}), are shown in Table 5.8.

Table 5.9 shows the peak loads obtained by computational simulation and experimental data from Takayanagi et al. (1994) for the three specimens. For all three specimens, the maximum difference between the simulated peak load and corresponding experimental failure observations was less than 3.5%. From the simulated and observed fracture modes, it can be concluded that for specimen A the peak load may be increased by adding 90° plies to the top flange to prevent the transverse tensile fracture of the 0° plies. For specimen B, additional 0° plies in the flange would reduce the stress concentration in the web and thus increase the peak load. For specimen C it would be necessary to add 0° plies into the flanges to prevent lateral buckling.

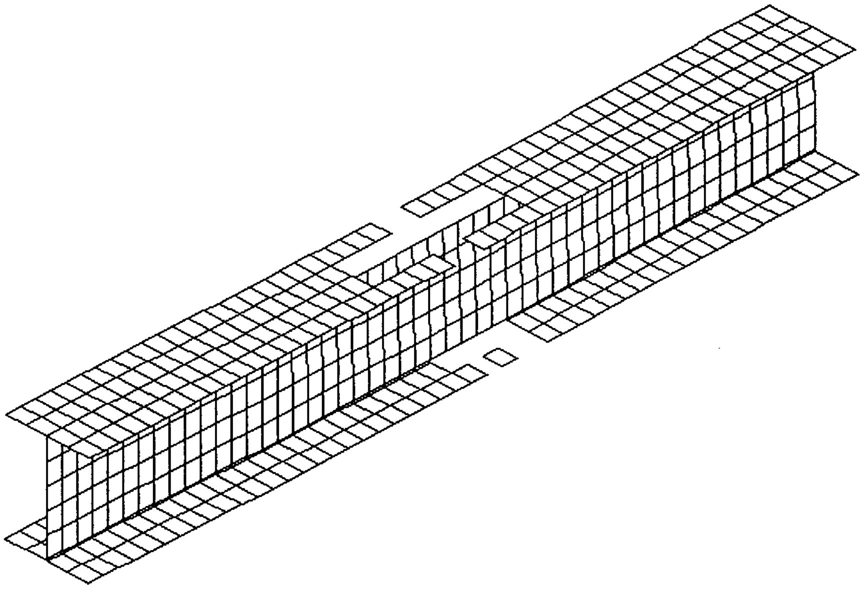

Figure 5.4 Finite Element Model of Specimen A at Collapse

5.6 Conclusions

In light of the damage propagation evaluation of the CFRP I-beams and from the general perspective of the integrated computational evaluation method, the following conclusions are drawn:

1. The assessment and design of CFRP structural shapes may be improved by an evaluation of the composite damage initiation and damage propagation mechanisms.

2. In general, composite structures demand a detailed understanding of the stress states

and material degradation characteristics for effective design.

3. Computational simulation, with the use of established composite mechanics and finite element methods, can be used to simulate the various stages of degradation in a composite structure, such as damage initiation, damage growth, damage accumulation, damage propagation, and structural fracture.

4. Computational simulation is based on constituent level material properties. However, even if the fiber and matrix properties are not explicitly defined, they can be determined from the given composite ply properties using a least-squares minimization procedure.

5. Significant design parameters such as composite constituent stiffness, strength, and effective ply configurations may be identified with the help of a composite mechanics module and computational simulation.

6. The demonstrated procedure is flexible and applicable to all types of constituent materials, structural geometry, and loading. Hybrid composites and homogeneous materials, as well as binary composites can be simulated.

7. The present computational simulation procedure provides a new general methodology to investigate damage propagation and progressive fracture for any structure.

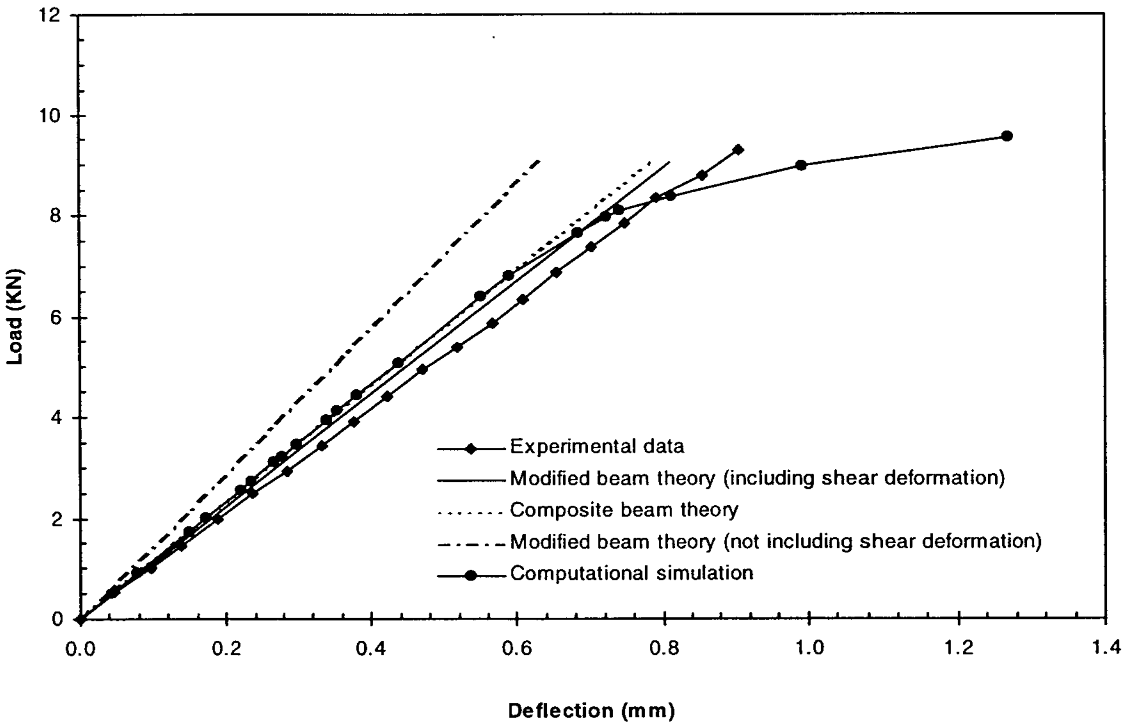

Figure 5.5 Relative Deflection of Specimen A under Loading

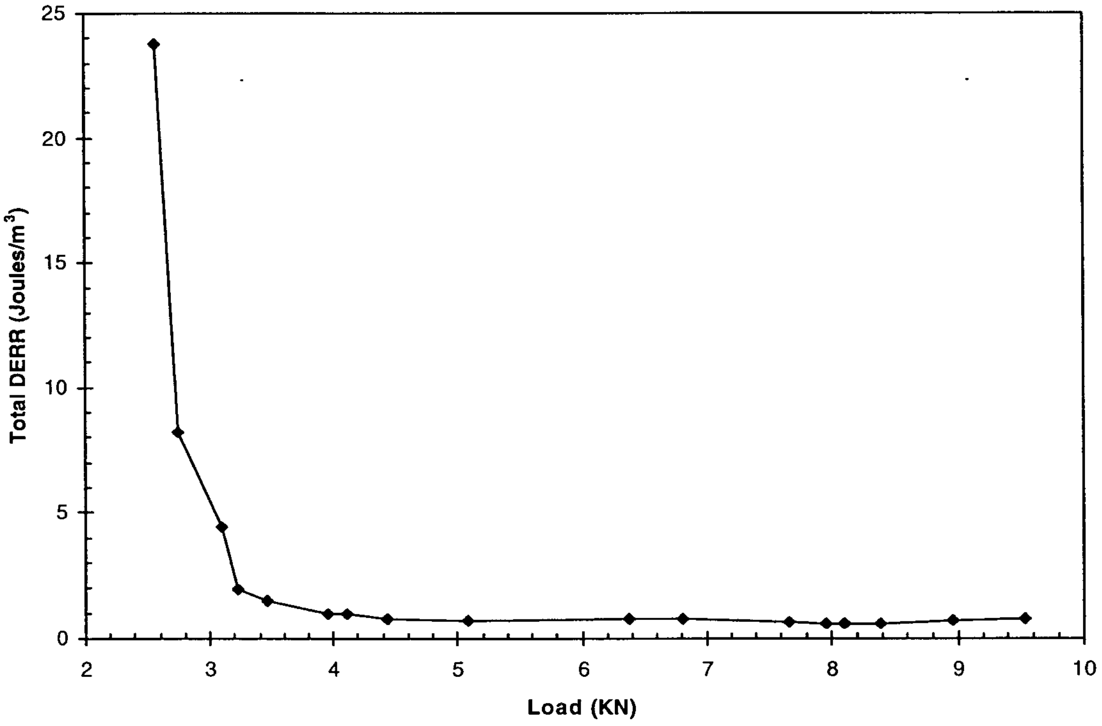

Figure 5.6 Damage Energy Release Rates of Specimen A under Loading

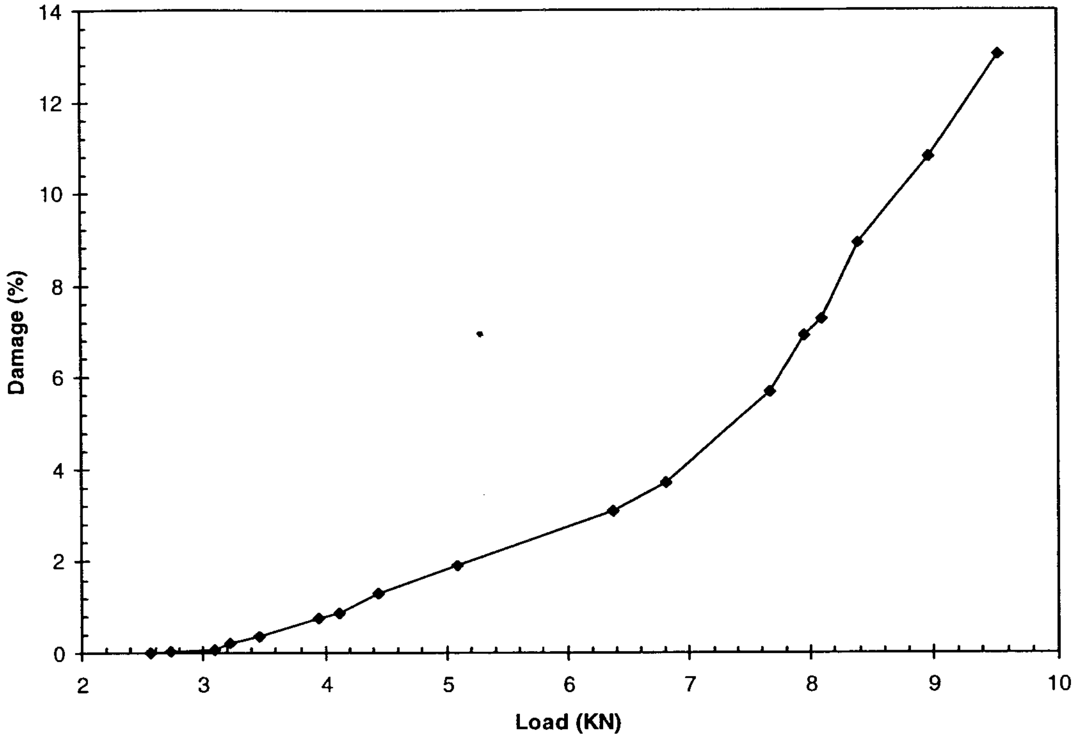

Figure 5.7 Damage Progression of Specimen A under Loading

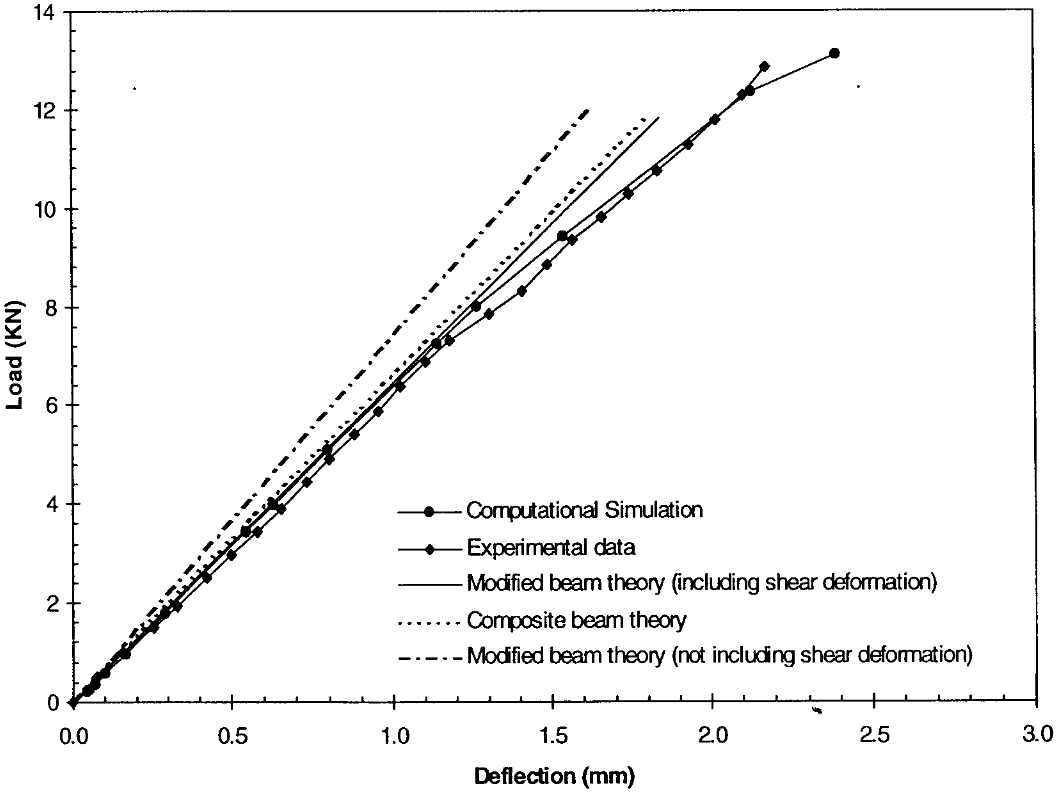

Figure 5.8 Relative Deflection of Specimen B Under Loading

Chapter 6

Computational Simulation of Progressive Fracture in Stitched J-Stiffened Composite Shear Panels in the Postbuckling Range

6.1 Introduction

Advanced composite structures, such as three-dimensional woven and stitched stiffened composite laminates are used in many aerospace applications such as aircraft fuselage and wing structures. Stitching or other through the thickness reinforcement greatly reduces the driving force for propagation of the delamination crack. The stitching creates closing traction acting across the laminate thickness that limits damage extension. However, it is important that the proportion of the through the thickness reinforcement is minimized to avoid significant degradation of the in-plane stiffness and strength properties.

The design evaluation of composite structures requires an assessment of their safety and durability under service loads and possible overload conditions. However, the architecture of a three-dimensionally reinforced composite is complex and, therefore, the parameters controlling its mechanical properties are numerous. Mechanical testing to characterize all the effects of composite architecture could be an economically unrealistic proposition. It is therefore crucial to develop experimentally verified analytical models to predict the load carrying capacity, damage tolerance, safety, and reliability of composite structures. An integrated computer code was developed in this paper for the purpose of evaluating stiffened composite panel progressive fracture in the post-buckled range.

An important feature of computational simulation is the assessment of damage stability or damage tolerance of a structure under loading. At any stage of damage progression, if there is a high level of structural resistance to damage progression under the service loading, the structure is stable with regard to fracture. The corresponding state of structural damage is referred to as stable damage. On the other hand, if damage progression does not encounter significant structural resistance, it corresponds to an unstable damage state. Unstable damage progression is characterized by very large increases in the amount of damage due to small increases in loading, whereas during stable damage progression the amount of increase in damage is consistent with the increase in loading.

Internal damage in composites is often initiated as cracking due to normal stress transverse to fiber orientation. Further degradation is in the form of additional cracking, delamination, and fiber fractures that may lead to structural fracture. The novelty of this paper is that various stages of degradation, from damage initiation to structural collapse of stitched laminates are simulated for the first time. The present computational method has previously been used for the investigation of the behavior of conventional laminated composite structures, including the effects of composite degradation on structural response (Minnetyan et al 1991), composite structures global fracture toughness (Minnetyan et al 1990), effect of the hygrothermal environment on durability (Minnetyan et al 1992-1), damage progression in composite shells subjected to internal pressure (Minnetyan et al 1992-2), the behavior of discontinuously stiffened composite panels under loading (Gotsis et al 1996), damage propagation in thick composite shells under external pressure (Minnetyan and Chamis 1997), damage and fracture progression in CFRP I-beams with three different lay-ups (Huang and Minnetyan 1998).

6.2 Methodology

The computational simulation tool presented in this paper is an integrated computer code consisting of three modules: composite mechanics, finite element analysis, and damage progression modeling. The overall evaluation of composite structural durability is carried out in the damage progression module that keeps track of composite degradation for the entire structure. The damage progression module relies on the composite mechanics module for micromechanics and macromechanics, and calls a finite element analysis module to obtain generalized stresses and displacements for the composite structure.

6.2.1 Evaluation of Elastic Constants

Elastic constants are essential for stress analysis of composites. The stiffness averaging method that was developed by Kregers and Melbardis (1978) is widely used to predict the deformation characteristics of a composite with three-dimensional reinforcement from the known mechanical properties of its components. However, utility of the stiffness averaging method is limited to the prediction of overall stiffness properties of a structure for elastic analysis. Stiffness averaging does not retain the information on the spatial configurations of fiber reinforcements. Therefore, the effects of damage and degradation cannot be directly taken into account for a specific ply and the results of structural analysis cannot be decomposed to the micromechanics level for detailed analysis of damage progression. In this paper, the stiffness averaging method and classical laminate theory are combined together to predict the properties for 3-D reinforced composites. For stitched laminates, each ply consists of not only in-plane fibers, but also through-the-thickness stitching fibers. Accordingly, each ply is divided into two subvolumes. The first subvolume consists of only in-plane fibers and the second consists of only the stitching fibers. The properties of each subvolume in its local coordinate system are computed from the properties of fiber and matrix, based on the classic intraply composite micromechanics theory (Chamis and Sinclair 1979), and then transformed to structural directions. The ply properties are obtained by adding contribution of each subvolume based on the stiffness averaging method:

$$[E_C] = \frac{1}{V}\sum_{i=1}^{N} V_i\,[R_i]^T\,[E_i]\,[R_i]$$

Where E_C is the composite ply stiffness. V_i is the calculated volume of the *i-th* subvolume, N is the number of subvolumes. E_i is the stiffness for the *i-th* subvolume, R_i is the coordinate transformation matrix for the *i-th* subvolume. After computation of the layer properties from the properties of subvolumes, properties of the entire stitched laminate are obtained by using laminate theory as one would obtain laminate properties for unstitched composites.

6.2.2 Finite Element Analysis

After the micromechanics analysis module generates the elastic properties for the stitched composite, a finite element analysis module is called to analyze the entire structural response. In general, the type of finite element model used depends on the complexity of the structure and the availability of computer resources. There are two possible choices for the analysis of composite structures. One is using anisotropic three-dimensional solid elements such as hexahedral or brick elements that accept the computed three dimensional composite properties directly. However, the modeling of a practical composite structure with three-dimensional elements requires huge computer resources and it is usually impractical for analyzing real structures. The second option is to use anisotropic shell elements that use the composite plate/shell element properties. Anisotropic plate or shell elements represent through-the-thickness properties of the stitched composite and are more efficient than three-dimensional elements. Therefore, implementation in this paper is focussed on the use of plate/shell elements in the finite element analysis module. The finite element module accepts the force-deformation relations computed by the composite macromechanics module, and carries out a stress analysis to generate the generalized stresses *Nx, Ny, Nxy, Mx, My, Mxy, Qxz, Qyz* for each node. The generalized stresses are supplied back to the composite mechanics module for the computation of local ply/stitch stresses and failure analysis.

6.2.3 Failure Criteria

Progressive damage and fracture simulations are carried out by imposing failure criteria locally within each subvolume with reference to the local coordinate orientations in the material directions. At each individual load step, stresses in stitching and in-plane subvolumes that can be obtained through the composite microstress analysis are assessed according to distinct failure criteria. The first twelve modes of failure are associated with the positive and negative limits of the six local stress components in the material directions as follows:

$$S_{\ell 11C} < \sigma_{\ell 11} < S_{\ell 11T}$$

$$S_{\ell 22C} < \sigma_{\ell 22} < S_{\ell 22T}$$

$$S_{\ell 33C} < \sigma_{\ell 33} < S_{\ell 33T}$$

$$S_{\ell 12(-)} < \sigma_{\ell 12} < S_{\ell 12(+)}$$

$$S_{\ell 23(-)} < \sigma_{\ell 23} < S_{\ell 23(+)}$$

$$S_{\ell 13(-)} < \sigma_{\ell 13} < S_{\ell 13(+)}$$

The thirteenth failure mode is a combined stress or modified distortion energy (MDE) failure criterion that is obtained by modifying the usual distortion energy failure criterion. The modification takes into account the significant differences in the stress limits of the longitudinal and transverse directions of an orthotropic composite ply. Each component of ply stress is normalized with respect to its limiting strength. No relationship is assumed between normal and shear strengths. The MDE failure criterion has been demonstrated to be a good predictor of combined stress failure in composites. It may be considered as a variation of the Tsai-Hill theory (Tsai 1968). The MDE failure criterion (Chamis 1969) can be expressed as:

$$\left(\frac{\sigma_{\ell 11\alpha}}{S_{\ell 11\alpha}}\right)^2+\left(\frac{\sigma_{\ell 22\beta}}{S_{\ell 22\beta}}\right)^2-K_{\ell 12\alpha\beta}\frac{\alpha_{\ell 11\alpha}}{S_{\ell 11\alpha}}\frac{\sigma_{l22\beta}}{S_{l22\beta}}+\left(\frac{\sigma_{\ell 12S}}{S_{\ell 12S}}\right)^2<1$$

Where α and β indicate tensile or compressive stresses, $S_{\ell 11\alpha}$ is the local longitudinal strength in tension or compression, $S_{\ell 22\alpha}$ is the transverse strength in tension or compression, and the directional interaction factor $K_{\ell 12\alpha\beta}$ is defined as:

$$K_{\ell 12\alpha\beta}=\frac{(1+4\upsilon_{12}-\upsilon_{13})E_{22}+(1-\upsilon_{23})E_{11}}{[E_{11}E_{22}(2+\upsilon_{12}+\upsilon_{13})(2+\upsilon_{21}+\upsilon_{23})]^{1/2}}$$

The directional interaction factor reduces to unity for homogeneous isotropic materials.

6.2.4 Simulation of Damage Progression

After each finite element stress analysis, failure criteria are used to evaluate possible failure within each subvolume of each ply at each node of the composite structure. Once the damage modes at each node are assessed, a damage index is created to record the damage information for each damaged node. The damage index contains the node number, the ply number, and the list of damage criteria that have become activated. When a new failure occurs at a subvolume, the damage index is updated correspondingly. The properties of each domain are degraded according to their damage index.

If there is no damage after a load increment, the structure is considered to be in equilibrium and an additional load increment is applied. If any damage occurs, the composite properties affected by the damage are degraded, the computational model is reconstituted with updated finite element mesh and material properties, and the structure is reanalyzed under the same load increment. After reanalyzing, if there is any additional damage, the properties are degraded again and the structure is reanalyzed again. This cycle continues until no further damage occurs.

The damage progression module keeps a detailed account of composite degradation for the entire structure. It also acts as the master executive module that directs the composite mechanics module to perform micromechanics and macromechanics analysis/synthesis functions, and calls the finite element module with thick shell analysis capability to model stitched laminated composites for global structural response.

6.2.5 Damage Energy Release Rate

The measure of global fracture toughness is defined in terms of the Total Energy Release Rate (TERR) that is equal to the amount of damage energy expanded for the creation of unit damage volume in the composite structure. The magnitude of TERR varies during progressive degradation of the composite structure under loading, reflecting the changes in the fracture toughness of the composite. Computation of TERR during progressive fracture is needed in order to evaluate the composite fracture toughness and the degree of imminence of failure.

TERR is computed as the ratio of damage energy to the corresponding damage volume that is generated:

TERR=Damage Energy/Damage Volume

Assuming locally linear elastic properties prior to damage, the damage energy can be computed as follows:

$$Damage\,Energy = \sum_i \sum_j \left(0.5S_j^2 / E_j\right) V_i$$

Where S_j is the local composite strength associated with the damage mode, E_j is the elastic modulus corresponding to S_j, and V_i is the volume of damage. Typically, at the stage of damage initiation, there is a high rate of energy release that dissipates a significant portion of the strain energy stored in the composite structure. After the first burst of energy release, TERR usually drops down to a lower level, indicating the significant reduction in fracture stability of the damaged composite under the applied loading. TERR usually reaches its peak value as global structural failure occurs.

6.3 J-Stiffened Composite Panels

The panels simulated in this paper contain two J-shaped stiffeners as shown in Figure 6.1. The experimental results for these panels were adopted from the literature (Yeh and Chen 1996). The panels were made of AS-4/3501-6 carbon/epoxy unidirectional fabric. The fabric consisted of a wide sheet of unidirectional tows of fibers based together with polyester thread to keep it from unraveling. Twelve plies of the skin were laid up to form a 1.83 mm (0.072 in.) thick quasi-isotropic $[0,90,45,0,-45,90]_s$ laminate, each ply had approximately the same thickness. The "J" shaped stiffeners were constructed with the same lay-up except for the flanges that were only half the thickness of the basic laminate. The skin panel and the stiffeners were stitched together with Kevlar and fiberglass threads.

Yeh & Chen (1996) tested two panel specimens with aluminum doublers bonded onto edges. Panel #1 is shown in Figure 6.1(a) and Panel #2 is shown in Figure 6.1(b). In order to simulate these specimens, a finite element model shown in Figure 6.2 was used. Mindlin type thick composite shell elements were utilized to represent the skin panel and stiffeners. The aluminum doublers were modeled with rigid elements.

6.4 Fiber and Matrix Properties Calibration

The first step in this simulation was to identify details of the fiber and matrix properties. Since Yeh & Chen (1996) only gave ply properties, and did not provide explicit information on fiber and matrix properties, the composite mechanics module (Murthy and Chamis 1986) was used to calibrate the fiber and matrix properties so that the computed ply properties matched those of the AS-4/3501-6 composite tested by Yeh & Chen. The properties for AS-4 and 3501 provided by the resident databank of the composite mechanics code (Murthy and Chamis 1986) were used as the initial values of AS-4 fiber and 3501-6 matrix respectively. Ply properties computed by the composite mechanics module were compared with the experimental monolayer values provided by Yeh & Chen. The difference between the computed properties and experimental observation was minimized in the root-mean-square relative error sense. The root-mean-square relation error was defined as:

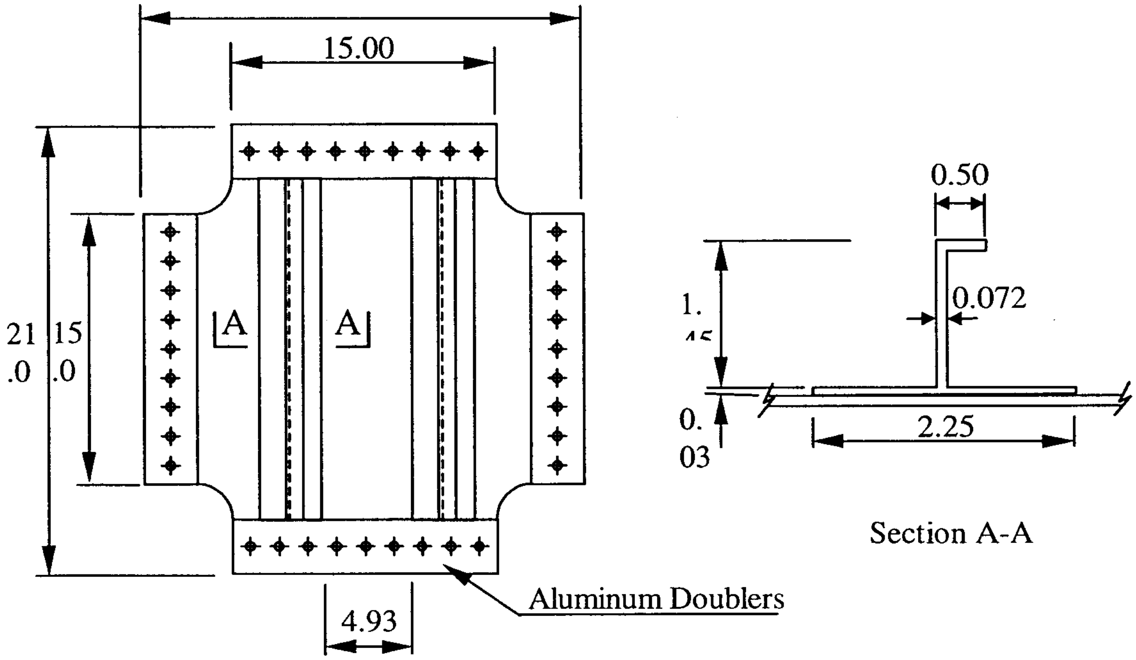

(a). Panel #1

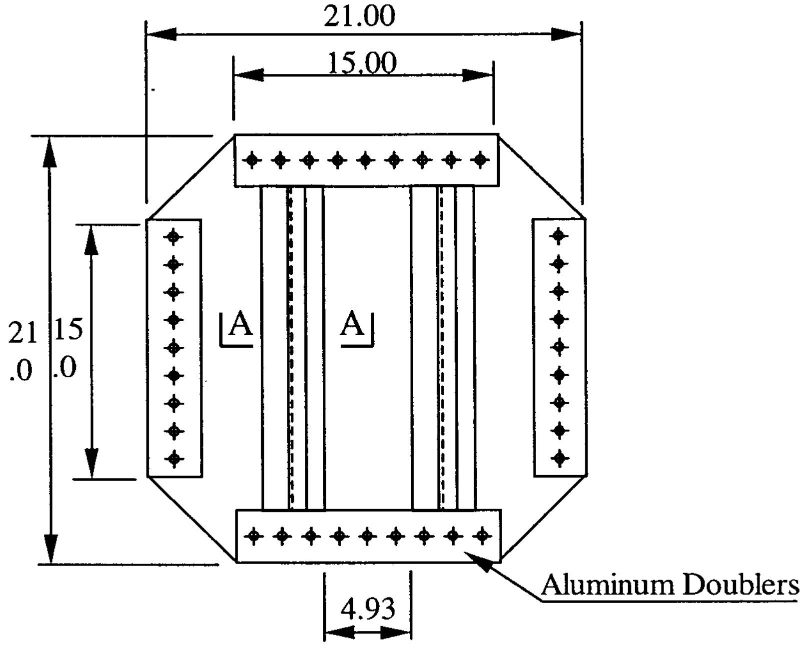

(b). Panel #2

Figure 6.1. Sketch of Panels

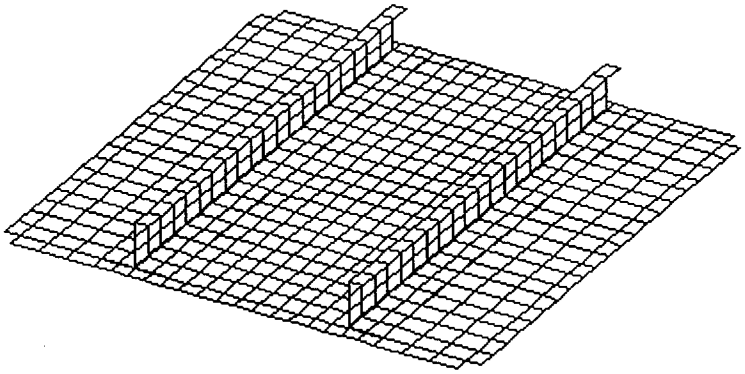

Figure 6.2. Finite Element Model and Loading Condition

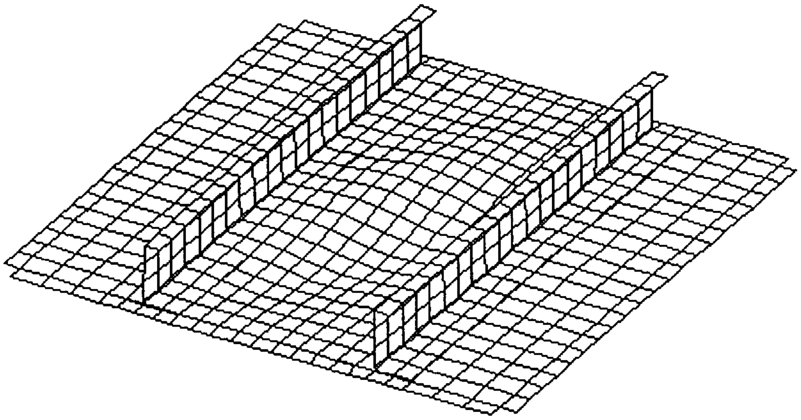

Figure 6.3. Panel Buckling Mode

$$\Omega=\sqrt{\frac{1}{n}\sum_{i=1}^{n}\left(\frac{P_i^{computed}-P_i^{experiment}}{P_i^{experiment}}\right)^2}$$

Where $P_i^{experiment}$ is the value of composite property (such as E_{11}, E_{22}, G_{12}, etc.) from experiment. $P_i^{computed}$ is the value of the same property computed by the composite mechanics module. N is the number of composite ply properties observed.

It is obvious that the smaller the value of Ω the more accurate the fiber and matrix properties. However, because of the natural complexity of the composite material, as well as the uncertainty and variability of experimental observations, it was not possible to obtain computed ply properties exactly the same as those experimentally observed. Based on the fiber and matrix properties given in Tables 6.1 and 6.2, the composite properties computed by the composite mechanics module are shown in Tables 6.3 and 6.4. The value of Ω for the monolayer properties is 0.0272. This means that the overall difference between experimental and simulated ply properties is less than 3 percent.

Table 6.1: Fiber Properties

	AS4	Kevlar
Number of fibers per end	*10000*	*580*
Fiber diameter *(in)*	*0.0003*	*0.00046*
Fiber Density *(lb/in^3)*	*0.063*	*0.053*
Longitudinal normal modulus *(10^6 psi)*	*31.2*	*22.0*
Transverse normal modulus *(10^6 psi)*	*2.82*	*0.60*
Poisson's ratio μ_{12}	*0.27*	*0.35*
Poisson's ratio μ_{23}	*0.30*	*0.35*
Shear modulus G_{12} *(10^6 psi)*	*10.0*	*0.42*
Shear modulus G_{23} *(10^6 psi)*	*10.0*	*0.22*
Longitudinal thermal expansion coefficient *(10^{-6}/°F)*	*0.550*	*2.20*
Transverse thermal expansion coefficient *(10^{-6}/°F)*	*0.560*	*30.0*
Longitudinal heat conductivity *(BTU-in/hr/in^2/°F)*	*4.03*	*1.70*
Transverse heat conductivity *(BTU-in/hr/in^2/°F)*	*4.03*	*1.70*
Heat capacity *(BTU/lb/°F)*	*0.17*	*0.25*
Tensile strength *(ksi)*	*320*	*400*
Compressive strength *(ksi)*	*295*	*75*

Table 6.2. 3501-6 Matrix properties

Matrix density *(lb/in$^{3)}$*	*0.0457*
Normal modulus *(ksi)*	*600*
Poisson's ratio	*0.400*
Coefficient of thermal expansion *(10^{-4}/°F)*	*0.4*
Heat conductivity *(10^{-3} BTU-in/hr/in^2/°F)*	*8.681*
Heat capacity *(BTU/lb/°F)*	*0.250*
Tensile strength *(ksi)*	*4.2*
Compressive strength *(ksi)*	*3.68*
Shear strength *(ksi)*	*14.0*
Allowable tensile strain	*0.02*
Allowable compressive strain	*0.05*
Allowable shear strain	*0.04*
Allowable torsional strain	*0.04*
Void conductivity *(BTU-in/hr/in^2/°F)*	*0.225*
Glass transition temperature *(°F)*	*420*

Table 6.3. Monolayer properties and allowables for AS4/3501-6 unidirectional fabric

	Experiment	Simulation
longitudinal modulus E_L *(psi)*	17.5 x 10^6	17.43 x 10^6
transverse modulus E_T *(psi)*	1.45 x 106	1.42 x 106
shear modulus G_{LT} *(psi)*	0.51 x 106	0.51 x 106
poisson's ratio ν_{LT}	0.34	0.33
longitudinal tension strength S_{Lt} *(psi)*	176,000	176,000
longitudinal compression strength S_{Lc} *(psi)*	162,750	162,200
transverse tension strength S_{Tt} *(psi)*	3,493	3,566
transverse compression strength S_{Tc} *(psi)*	31,388	31,250
shear strength S_{sh} *(psi)*	11,547	11,890

6.5 Results and Discussion

Figure 6.2 shows the finite element model used in the simulation of these panels. The model is loaded by applied tension loading in the diagonal direction at one corner of the panel, and constrained in X, Y, and Z directions at the opposite corner. First, the simulation under a monotonically increasing static loading was performed, without considering lateral buckling of the skin. Since experimental data indicated that local buckling of the skin occurred prior to reaching the peak load, a linear buckling analysis was conducted next. Buckling analysis showed that the initial buckling load was 8275 lb. That is very close to the experimental results. According to Yeh and Chen's experiments (1996), initial buckling load for panel #1 was approximately 7500lb and for panel #2 was approximately 8500 lb. In order to study the effect of lay-up configuration on the peak load, four different lay-ups described in Table 6.4 were simulated in the present study. Since Yeh and Chen gave experimental results for the [0/90/45/0/-45/90] layup, the simulated details of damage progression for this lay-up are presented in the next section. Only a summary of the simulation results will be presented for panels with other lay-ups.

6.5.1 Analysis Without Considering Lateral Buckling of the Skin

In order to study how buckling can affect damage progression, first the stiffened panel with $[0/90/45/0/-45/90]_s$ lay-up was analyzed without considering the lateral buckling effect. The load applied to the panel was started at 445 N (100 lbs) and then increased gradually. When the load increased to 133 kN (29900 lbs), damage occurred at the edges of the stiffener due to the transverse compression failure of some 0-degree plies (plies 9,12,13,16). These damaged nodes are indicated by an "a" in Figure 6.4. When the load increased to 139 kN (31300 lbs), damage occurred at another end of the edge of the stiffeners, indicated as "b" nodes in Figure 6.4. The "b" nodes were also damaged due to compression failures in the 0-degree plies. When the load was increased to 152 kN (34200 lbs), the damaged nodes extended to the middle from the ends along the edges of the stiffeners and 90-degree plies started to damage due to shear failure, as indicated by the "c' nodes in Figure 6.4. When the load reached 165 kN (37000 lbs), there were more nodes damaged, indicated as "d" nodes in Figure 6.4. 165 kN was the maximum equilibrium load before the panel collapsed. When load reached 169 kN (37900 lbs), some nodes shown in Figure 6.4 as "x" nodes started to fracture and nodal fractures immediately extended to adjacent nodes along the edges of the J-stiffeners. Even though the load was not increased any more, the fracture line continued to extend causing the collapse of the entire structure.

Table 6.4. Laminate properties for panels with different lay-up

	$[0/90/45/0/-45/90]_S$		$[45/-45/90/45/0/-45]_S$	$[0]_{12}$	$[0/90/0/90/0/90]_S$
	Experiment	simulation			
E_X (10^6 psi)	7.765	7.78	5.40	17.43	9.497
E_Y (10^6 psi)	7.272	7.78	5.40	1.42	9.497
G_{XY}(10^6 psi)	1.95	1.85	3.186	0.51	0.51

Table 6.5. Initial damage and peak loads for panel with different lay-up

Lay-up	Initial damage load (lb)	Maximum equilibrium load (lb)	Load causing structure collapse(lb)	Average Experimental failure load(lb)
$[0/90/45/0/-45/90]_s$	12800	27600	27800	27500
$[45/-45/90/45/0/-45]_s$	9685	26000	26300	-
$[0/90]_{6s}$	3780	8740	8810	-
$[0]_{12}$	850	6570	6600	-

6.5.2 Postbuckling Analysis

Since the initial local buckling load is much less than the peak load, post-buckling analysis is necessary for a realistic simulation of the stiffened panel. In order to do postbuckling analysis, buckling analysis was conducted before progressive fracture to obtain the buckling load. Subsequently, damage progression was simulated as follows: If the applied load was less than the buckling load, then a regular FEM analysis was conducted for the evaluation of composite stresses. After the applied load exceeded the buckling load, the buckling mode as shown in Figure 6.3 was imposed onto the structural geometry for FEM analysis. The load was started at 445 N (100 lbs). When the load increased to 36.8 kN (8275 lbs), local buckling occurred, therefore the buckling mode as shown in Figure 6.3 was used for the FEM analysis increments afterwards. When load was increased to 56.9 kN (12800 lbs), the "a" node shown in Figure 6.5 started to sustain damage due to the transverse compression failure of the outmost 0-degree ply. When the load increased to 66.7 kN (15000 lbs), damage extended to the edges of the stiffeners and other nodes (see "b" nodes in Figure 6.5). As the load was increased, damage extended to more nodes. When the load increased to 123 kN (27600 lbs), 90-degree plies were damaged in the shear failure mode. However, no node had yet experienced a through-the-thickness laminate fracture. The positions of nodes damaged at this stage are indicated as "c" nodes in Figure 6.5. When the load was increased to 124 kN (27800 lbs), through-the-thickness laminate fracture occurred at some nodes indicated as "x" nodes in Figure 6.5. Through-the-thickness fracture extended to adjacent nodes very quickly, resulting in structural fracture. Therefore the peak load was 27600 lbs. This was very close to the experimental peak load. According to Yeh & Chen (1996), the experimental peak load for Panel #1 was 119 kN (26800 lbs). and for Panel #2 was 125 kN (28200 lbs). The average experimental peak load was 122 kN (27500 lbs). Experimental and simulated relationships between the applied load and the corresponding diagonal deflection are shown in Figure 6.6.

Figure 6.7 shows the relationship between applied load and produced damage volume. Damage initiation occurred at 56.9 kN (12800 lbs). After the load reached 109 kN (24500 lbs), the amount of damage increased greatly. When the load reached the 123 kN (27600 lbs), 5.84 percent of the panel was damaged. After that, the panel entered an unstable damage propagation state. When the simulated load was increased to 124 kN (27800 lbs), the damage volume increased rapidly until peak structural failure occurred. Figure 6.8 shows the relationship between damage energy and load. Similar to the damage volume depicted in Figure 6.7, damage energy also increased rapidly after the load reached 109 kN (24500 lbs).

6.5.3 Analysis of Panels with other lay-ups

In order to study how the laminate configuration affects the peak load, simulations of panels with other lay-ups were also included in this study. All the panels had the same size, same thickness and same stiffeners. The three additional simulated panels had the laminate configurations of $[45/-45/90/45/0/-45]_s$, $[0/90]_{6s}$, $[0]_{12}$. The laminate properties for these panels are shown in Table 6.4. Tables 6.4 and 6.5 show the initial damage load, peak load, and initial buckling load. From these results it can be seen that the lay-up configuration has a significant effect on the peak load. Similar to the panel with a lay-up $[0/90/45/0/-45/90]_s$, the panel with a lay-up of $[45/-45/90/45/0/-45]_s$ was locally buckled before its collapse. After local buckling, the load was able to increase quite a bit. The peak load was more than three times the initial buckling load. For the panels with a cross-ply lay-up of $[0/90]_{6s}$, the peak load was just a little larger than the initial buckling load. This should not be interpreted to mean that buckling has a much more significant effect on the peak load for the cross ply panel than for the panels with 45-degree plies. As a matter of fact, even when the initial buckling effect was not taken into account, the peak load for the cross ply panel was only 42.1 kN (9470 lbs). Therefore the 45-degree plies play an important role in increasing peak loads. For the panel with unidirectional lay-up, the initial buckling load was larger than the peak load, therefore the unidirectional panel collapsed before buckling. Figure 6.9 shows the load-deflection relationships for the panels with different ply layup configurations.

6.6 Conclusions

1. A Computational simulation tool developed for the analysis of conventional laminated composite structures (Minnetyan et al, 1992, 1995) was extended to the analysis of composite-stiffened-stitched-shear panels.

2. Postbuckling effects have a significant influence on the peak collapse load of quasiisotropic stiffened shear panels.

3. Computational simulation without considering the postbuckling mode overpredicts the collapse load by approximately 35 percent. The stiffness is overpredicted by 7.6 percent.

4. It was found that ply configuration significantly affects the strength of stitched composite panels under shear loading.

5. Damage volume and/or damage energy can be used to evaluate the overall degradation stage of a structure.

6. Computational simulation provides an effective means for parametric design investigations of stiffened and stitched composite structures.

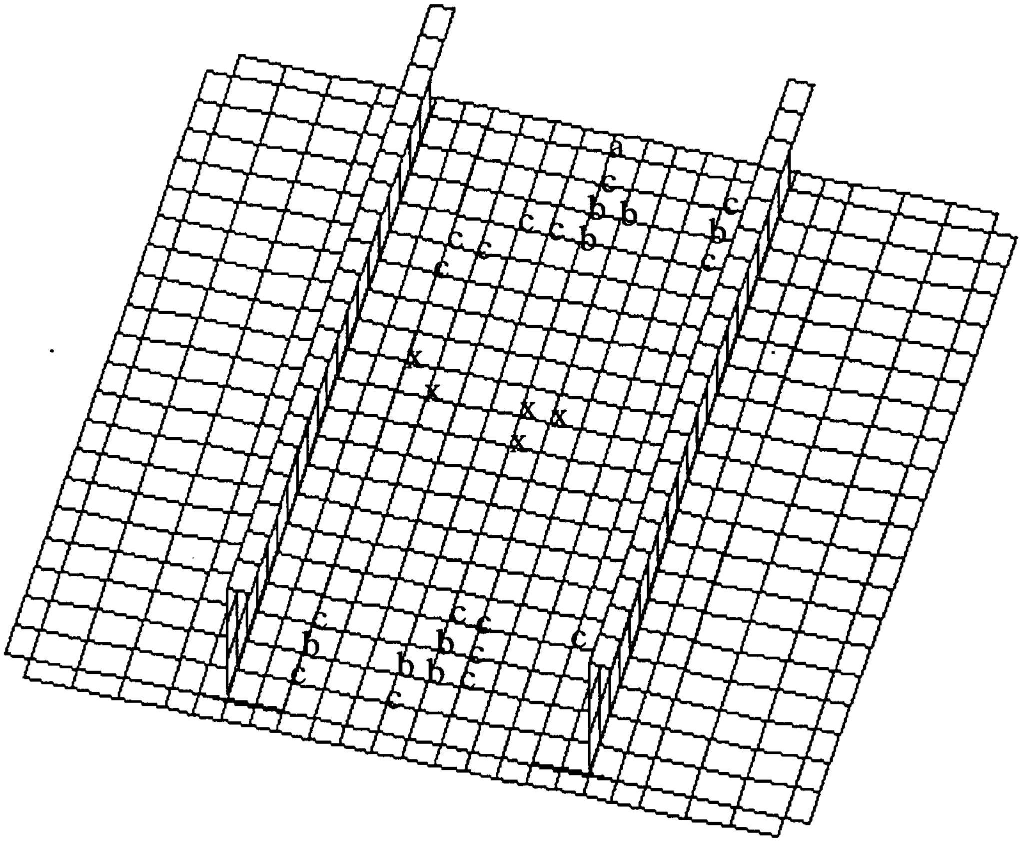

Note: Initial damage load for nodes a: 12800lb, b: 15000lb, c: 27600lb,
x indicates the nodes first cracked under loading 37900lb.

Figure 6.4. Damage Node Indication for Panel with Ply Configuration $[0/90/45/0/-45/90]_S$ with Postbuckling Analysis

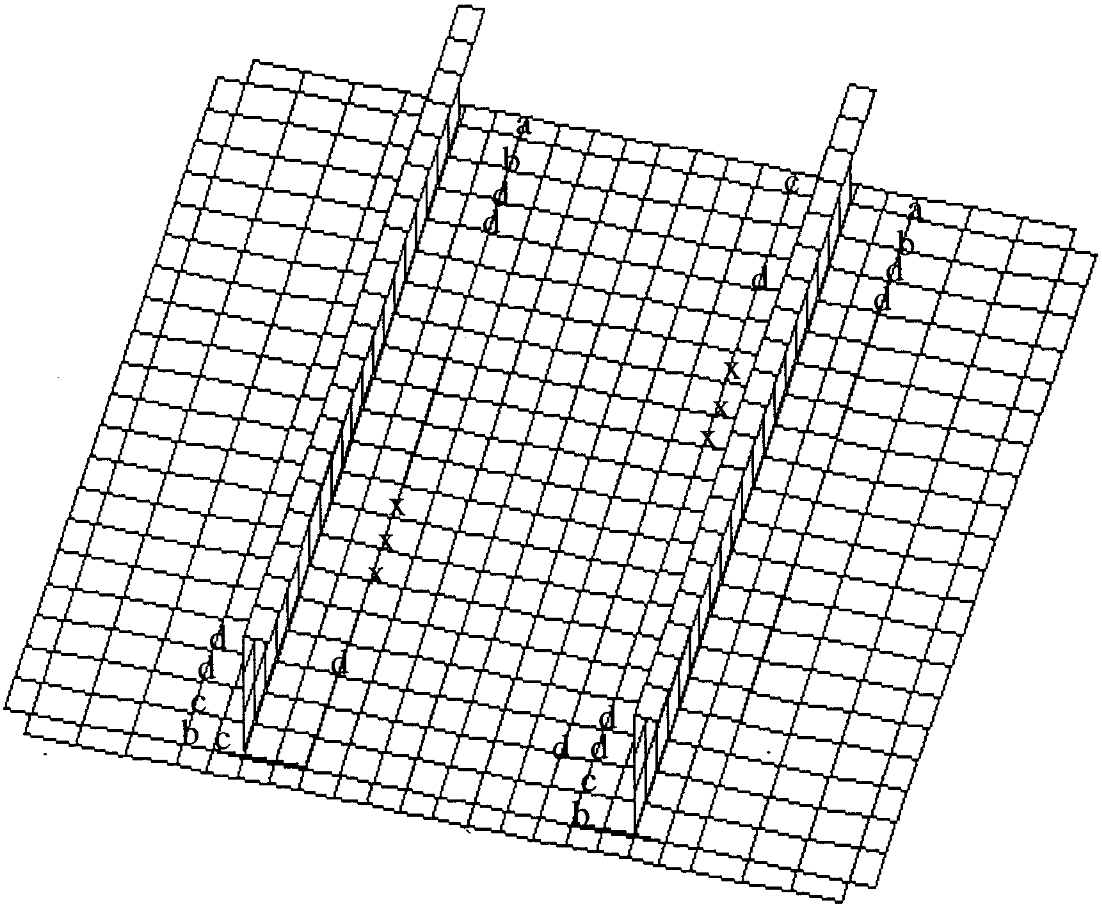

Note: Initial damage load for nodes a: 29900lb, b: 31300lb, c: 34200lb, d: 37000lb, x indicated the nodes first cracked under loading 37900lb

Figure 6.5. Damage Node Indication for Panel with Ply Configuration $[0/90/45/0/-45/90]_S$ without Postbuckling Analysis

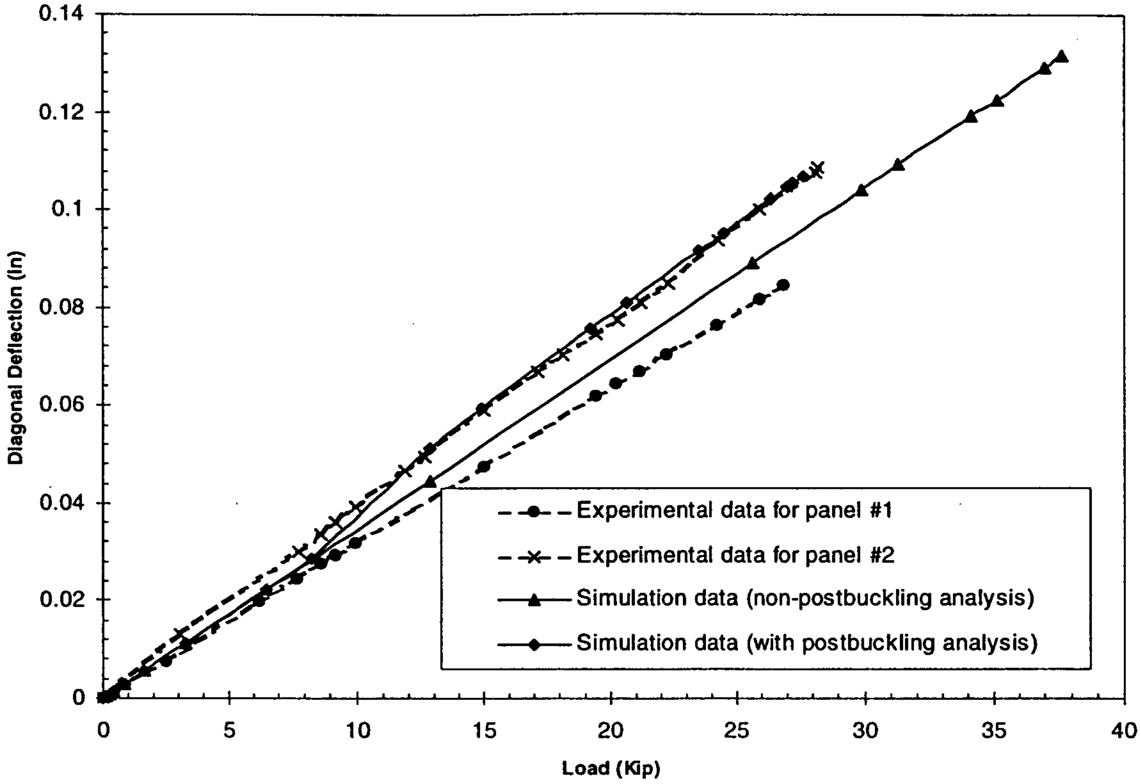

Figure 6.6. Diagonal Deflection for Panel with Ply Configuration [0/90/45/0/-45/90]s

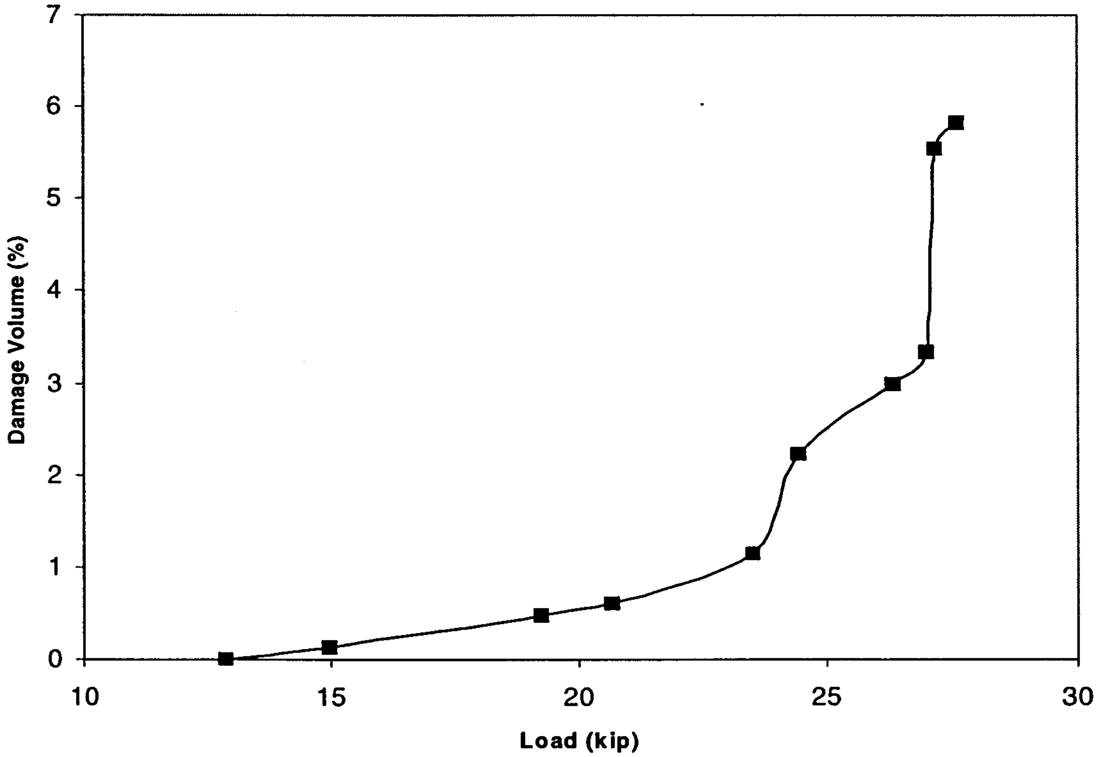

Figure 6.7. Damage Progression of Panel with Ply Configuration [0/90/45/0/-45/90]s

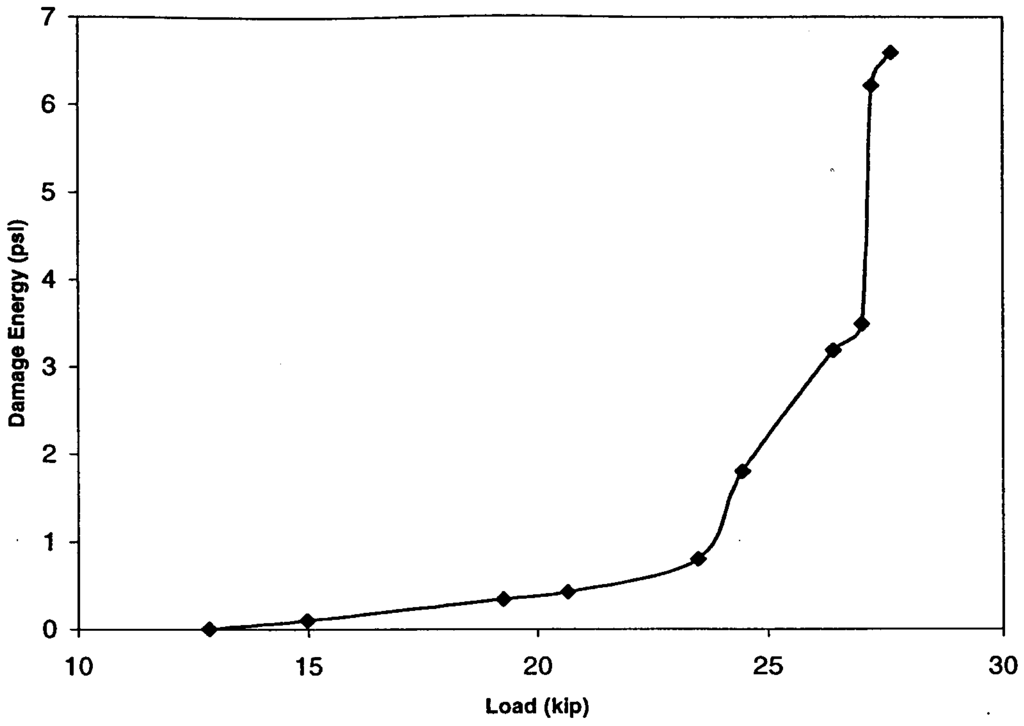

Figure 6.8. Damage Energy of Panel with Ply Configuration $[0/90/45/0/-45/90]_S$

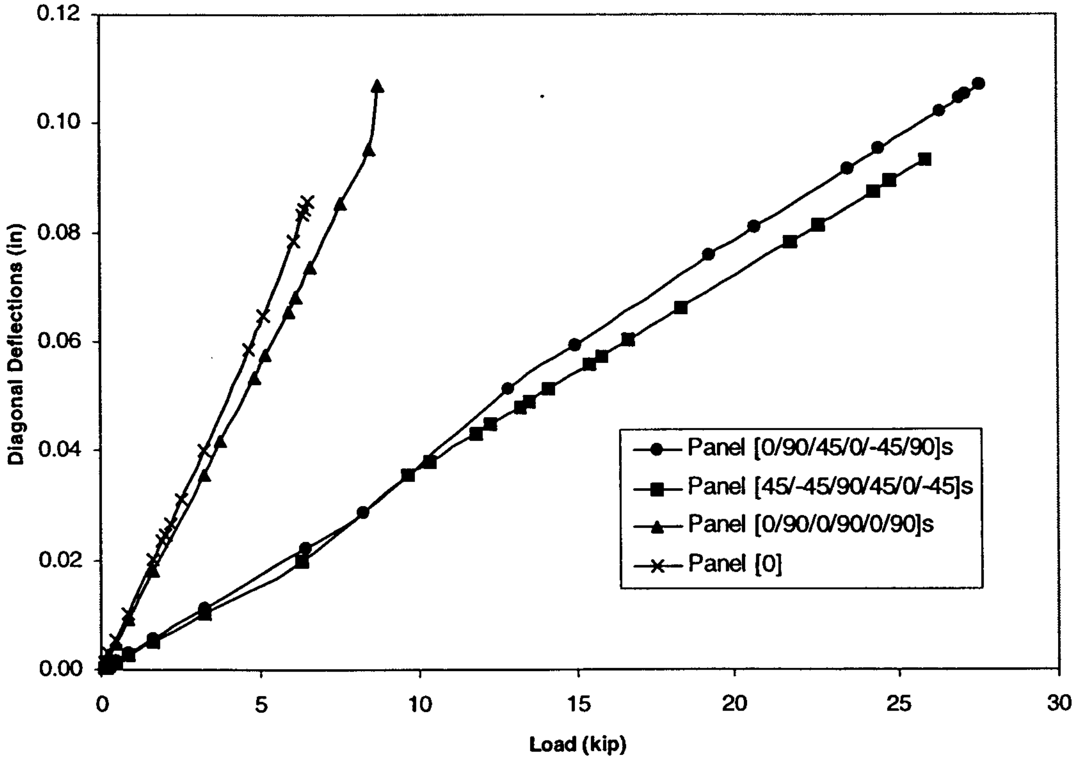

Figure 6.9. Diagonal Deflection for Panels with Different Ply Configuration

Chapter 7

Computational Simulation of Progressive Fracture in Ceramic Matrix Composites

7.1 Introduction

Ceramic matrix composites (CMC) are currently a subject of great deal of research interest due to the requirement of new high temperature materials for use in high-speed engine structural components and other applications. Continuous-fiber reinforced ceramic matrix composites offer a great deal of promise in this area and hence considerable effort is being devoted for their development. They offer several advantages such as high specific stiffness and strength, high toughness as compared to monolithic ceramics, environmental stability and wear resistance for both room and elevated temperature applications. Ceramic matrix composites are reinforced primarily for enhancing the toughness as the matrices in these composites are brittle and fail at relatively low strain levels. It is also desirable to have a weak fiber/matrix interface in these composites to enable such toughening mechanisms as fiber debonding, fiber bridging, fiber pullout, crack deflection etc. to eliminate catastrophic failures. However, for the full potential of these materials to be attained, research will have to provide insights into accurate micro-mechanical characterization of ceramic matrix composites. This chapter will develop computational tools to simulate the progressive fracture in ceramic matrix composite structures.

7.2 Micro- and Macro-mechanical Characterization of Ceramic Matrix Composites

Prediction of properties of ceramic matrix composites is based on a computational method developed to specifically simulate aspects unique to ceramic matrix composites (Mital and Murthy 1996). The method incorporates a slice-by-slice substructuring technique that has many advantages including a more accurate micro-mechanical representation of interfacial conditions, both around the fiber and through-the-thickness and provides a greater detail of stress distribution within a ply.

A multilevel substructuring technique, which includes a unique fiber substructuring concept, is used for the analysis of continuous fiber reinforced ceramic matrix composites. This technique has four levels of substructuring-from laminate to ply, to subply, and then to fiber. The fiber is substructured into several slices and the micromechanics equations are applied at the slice level. Although the basic philosophy can be applied to the analysis of any continuous fiber reinforced composite, the emphasis is on the development of a method to specifically analyze and simulate aspects unique to ceramic matrix composites. The aspects of interest include varying degrees of interfacial bond around the fiber circumference and accounting for the fiber breaks and local matrix cracking which may lead to rapid degradation of interphase at higher temperatures due to oxidation. In addition, the multilevel substructuring technique can account for different fiber shapes and integrate the effect of all of these aspects on composite properties/ response and, in turn, provide a greater detail in stress distribution.

Composite micromechanics equations are used to determine the equivalent elastic properties of a composite material in terms of the elastic properties of the fiber and matrix constituent materials. The properties of interest are composite moduli, Poisson's ratios, thermal expansion coefficients, thermal conductivity, heat capacity, etc., and various composite strengths. The micromechanics equations are derived for a representative volume element (RVE), sometimes referred to as a "Unit cell" which is the smallest region over which the stresses and strains are assumed to be macroscopically uniform. The unit cell consists of fiber, matrix, and possibly an interphase treated as a separate constituent. The geometry of the unit cell depends upon the chosen array pattern for the fibers, e.g., square, hexagonal or any other kind of repeating geometry. Equivalent properties for the unit cell or RVE are then derived based on the constituent properties using a mechanics of materials approach. This approach is based on certain assumptions, in addition to a chosen array pattern. The assumptions are: (a) all the constituents are subjected to the same strain in the fiber direction in the case of a unidirectional composite, and (b) the same transverse stress is applied to all constituents in the direction transverse to the fiber. These are standard assumptions used for the derivation of micromechanics equations, but they are not mathematically rigorous. A mathematically rigorous solution that ensures the displacement continuity across the fiber and matrix boundary can be obtained through the use of theory of elasticity.

Prior to fiber substructuring the unit cell may consist of three distinct regions A, B, and C (figure 7.1A). The region A consists of pure matrix, the region B consists of matrix and interphase, and region C consists of fiber, matrix, and interphase. The interphase is treated as a distinct region with distinct mechanical and thermal properties. Thus, it can represent a reaction zone formed due to the chemical reaction between fiber and matrix or a separate layer provided intentionally to prevent such a reaction. The different regions facilitate representation of nonuniformity in the local stress distribution.

This approach has been taken one step further for the analysis of ceramic matrix composites. Although the same square fiber array pattern is assumed, the unit cell is further subdivided into several slices. The equations of micromechanics are derived for slices, i.e., slice equivalent properties are computed based on the properties of the fiber, matrix, and interphase. The fiber substructuring and slice geometry are shown in figure 7.1B. The derivations of the micromechanics are provided in detail by Murthy and Chamis (1992). For example, if k_f, k_m and k_i are fiber, matrix, and interphase volume ratios respectively, then for a typical slice

$$k_f = \frac{d_f}{s}; \quad k_m = 2\frac{d_m}{s}; \quad k_i = 2\frac{d_i}{s}$$

Where s is the width of unit cell, d_f is the width of fiber, d_m is the width of matrix, d_i is the width of interface.

The equivalent longitudinal slice modulus is given by,

$$E_{l11} = k_f\ E_{f11} + k_m\ E_{m11} + k_i E_{i11}$$

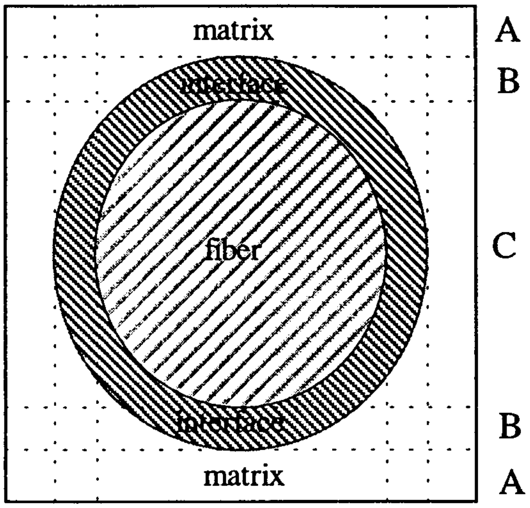

A). Unit cell square array concepts of ceramics composite

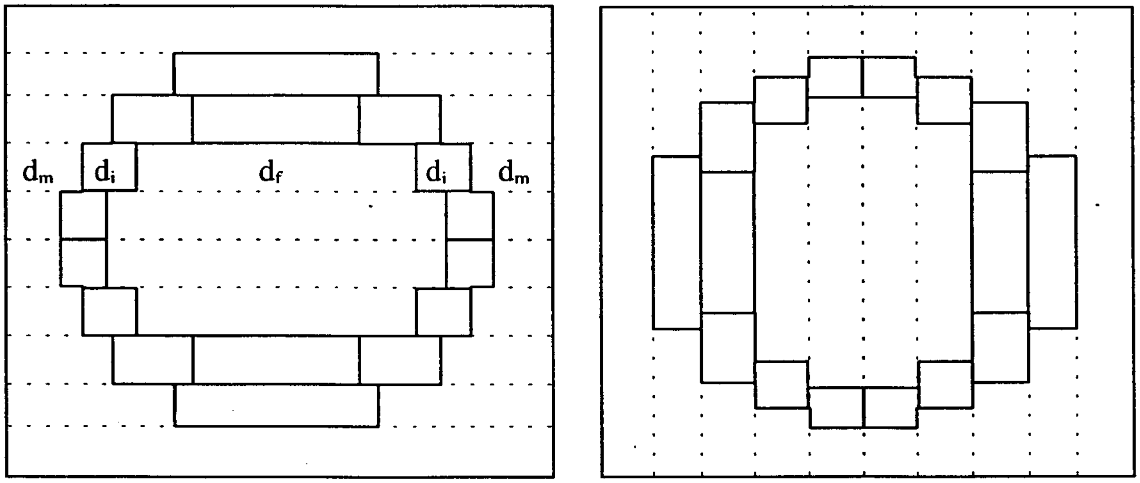

B). Horizontal slicing

C). Vertical slicing

Figure 7.1 Substructuring for ceramics composite micromechanics

The transverse modulus in the 2-2 direction is given by,

$$E_{l22} = \frac{E_{f22}\, E_{m22}\, E_{i22}}{k_f\, E_{m22}\, E_{i22} + k_m\, E_{f22}\, E_{i22} + k_i\, E_{f22}\, E_{m22}}$$

and the longitudinal thermal expansion coefficient is given by,

$$\alpha_{l11} = \frac{k_f \alpha_{f11} E_{f11} + k_m \alpha_{m11} E_{m11} + k_i \alpha_{i11} E_{i11}}{E_{l11}}$$

Similarly, other mechanical and thermal properties are expressed in terms of the constituent properties. Once the equivalent slice properties are obtained, the equivalent properties of the unit cell or RVE are obtained by using laminate theory in an analogous manner as one would obtain laminate properties from ply properties. It should also be mentioned that 2-2 or horizontal slicing is used to compute 1-1 and 2-2 slice properties, while 3-3 or vertical slicing is used to compute slice properties in the 3-3 direction.

To obtain the equivalent properties of a unit cell or RVE, the slice properties are integrated by using classical laminate theory. If there is only one fiber through the ply thickness, then the ply equivalent properties are identical to the properties of the unit cell or the RVE. If there are a number of fibers through the thickness of a single ply, then the unit cell properties have to be integrated by using the laminate theories again to obtain the ply properties. Laminate or composite properties are obtained from the individual ply properties by using macromechanics theories. For braided or woven composites, properties of the out-of-plane fiber reinforcements can be rotated into the laminate structural axes based on coordinate transformations and integrated into the entire structure via the zone-by-zone stiffness averaging method presented in chapter 3.

After the laminate properties are computed, the next step is to obtain the laminate response due to externally applied loads. The flowchart to outline these procedures is shown in figure 7.2. The left side of the chart shows synthesis of the properties from slice to laminate level. The right hand side of the flowchart shows the decomposition of the response from laminate to ply, to slice, and then to constituent microstress levels.

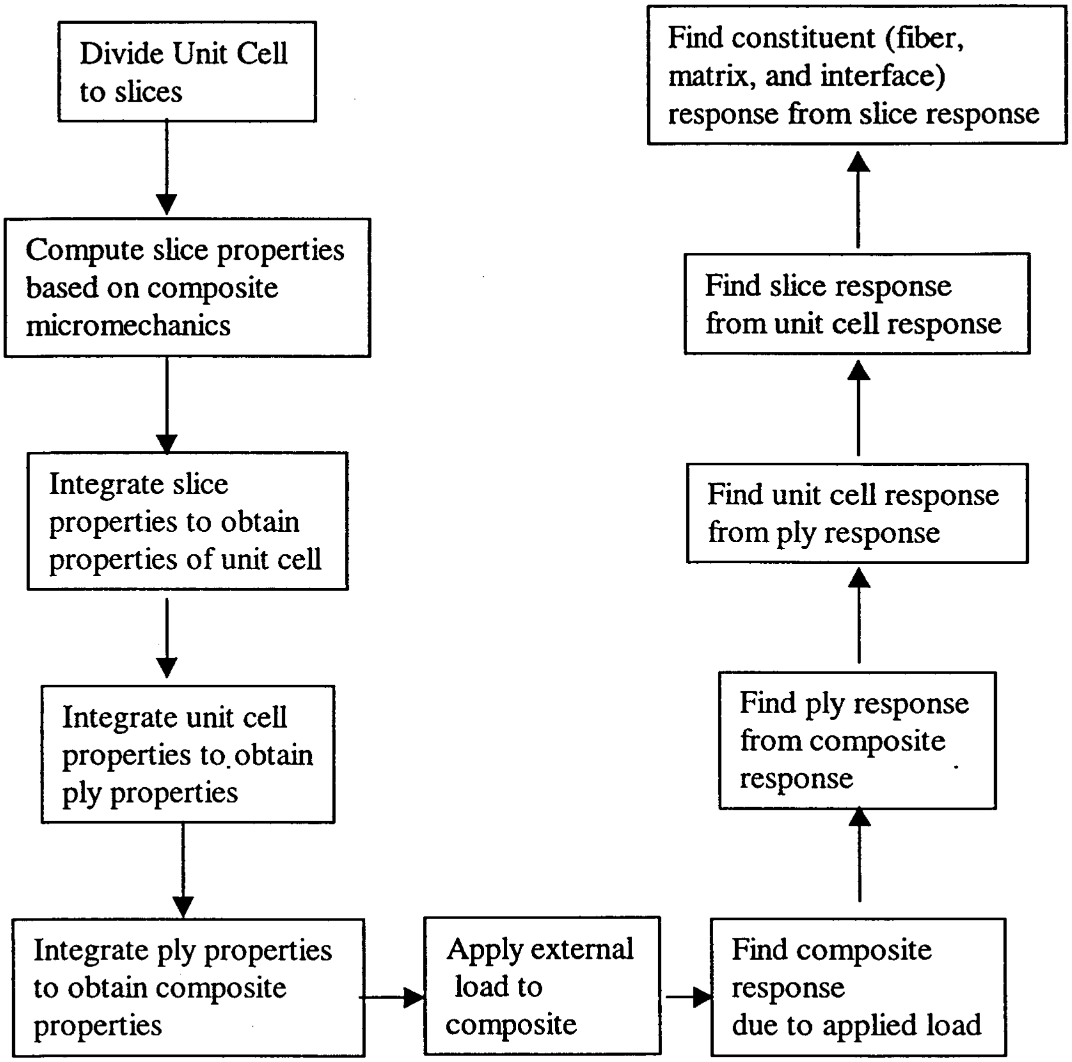

Figure 7.2 Integrated analysis procedure for ceramic matrix composites

7.3 Failure Criteria for Ceramic Matrix Composites

Failure criteria are essential for predicting progressive fracture in composites. Ceramic matrix composites consist of fiber, matrix, and interface. Fracture initiation in composites is usually caused by fiber breaking, matrix cracking, and/or interface failure. Therefore, in order to predict composite failure, we need to predict constituent failures. The failure criteria associated with stress limits can be expressed for fiber stresses as follows:

$$\begin{gathered}
S_{f11C} < \sigma_{f11} < S_{f11T} \\
S_{f22C} < \sigma_{f22} < S_{f22T} \\
S_{f33C} < \sigma_{f33} < S_{f33T} \\
S_{f12S(-)} < \tau_{f12} < S_{f12S(+)} \\
S_{f23S(-)} < \tau_{f23} < S_{f23S(+)} \\
S_{f13S(-)} < \tau_{f13} < S_{f13S(+)}
\end{gathered}$$

Where

S_{f11T} -- Longitudinal tensile strength of fiber,

S_{f11C} -- Longitudinal compressive strength of fiber,

S_{f22T} -- Transverse tensile strength (Y direction) of fiber,

S_{f22C} -- Transverse compressive strength (Y direction) of fiber,

S_{f33T} -- Transverse tensile strength (Z direction) of fiber,

S_{f33C} -- Transverse compressive strength (Z direction) of fiber,

S_{f12S} -- XY plane shear strength of fiber,

S_{f13S} -- XZ plane shear strength of fiber,

S_{f23S} -- YZ plane shear strength of fiber

Failure criteria for matrix and interface can be written similarly.

7.4 Progressive Fracture Simulation

An integrated computer code is developed to simulate progressive fracture in fiber reinforced ceramic matrix composite materials. As such it facilitates the evaluation of ceramic matrix composite structures with regard to damage tolerance and durability by simulating the various stages of degradation, from damage initiation to complete failure. This code contains three modules: CMC (Ceramic Matrix Composite micro-mechanics and macromechanics) module, FEM (Finite Element Method) module, and PFA (Progressive Fracture Analysis) module. Figure 7-3 shows schematic flowchart of this code.

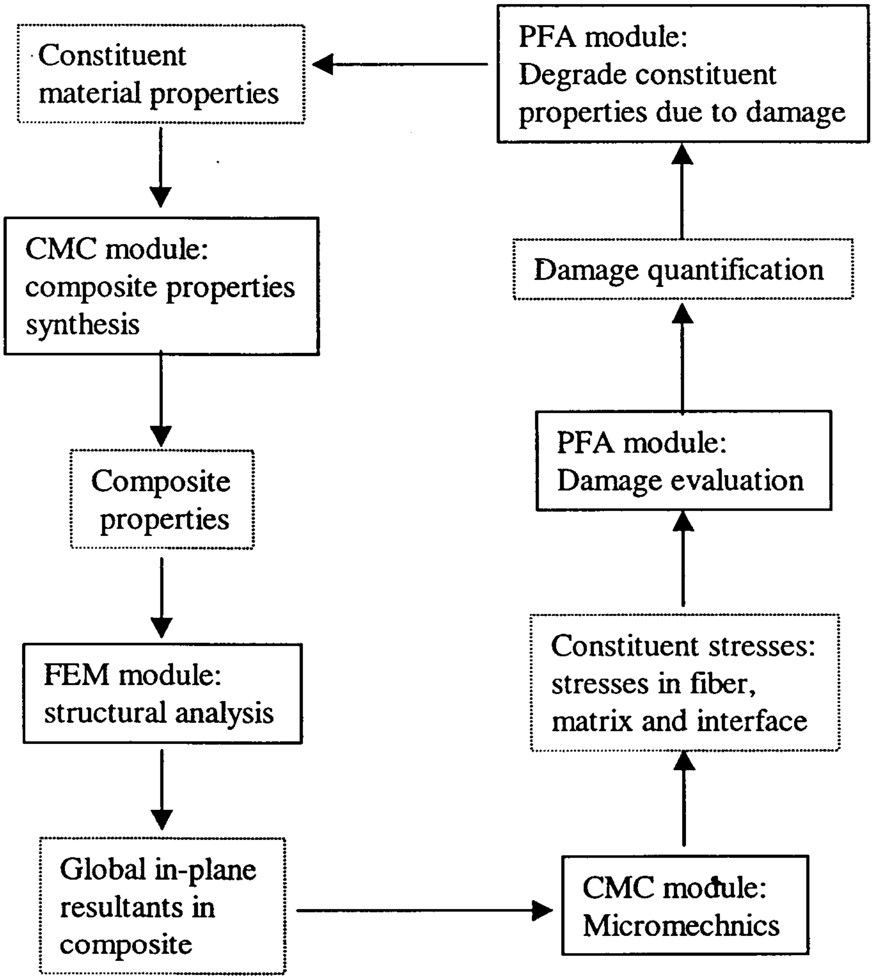

Figure 7.3 Ceramic Matrix Composite Progressive Simulation Cycle

The CMC module is based on software developed to specifically simulate aspects unique to ceramic matrix composites (Mital and Murthy 1996). It incorporates a fiber substructuring technique that provides: 1) accurate micromechanical representation of interfacial conditions, both around the fiber and through-the-thickness, and 2) greater detail of stress distribution within a ply. This module generates the properties (A, B, D matrix) of ceramic matrix composites from properties of the constituents (fiber, matrix, and fiber-matrix interface). The generated structural properties are used in the FEM module. CMC module can also be used to determine constituent level stresses, such as fiber, matrix and interface stresses.

The FEM module performs finite element analysis to determine the generalized stresses over the entire ceramic matrix composite structure. These generalized stresses are referred back to the CMC module for iterative determinations of composite microstresses.

The PFA module keeps a detailed account of composite degradation over the entire structure and also acts as an executive control module to direct the CMC module to perform micromechanics, macromechanics analysis, and synthesis functions. The damage progression module also calls FEM module with anisotropic thick shell analysis capability to model laminated composites for global structural response.

After each finite element analysis, the CMC module is called to compute constituent stresses. These stresses are compared to failure criteria for evaluation of possible fiber, matrix, and interface failure in each ply at each node of the ceramic composite structure. Once the state of damage at each node is assessed, a damage index is created to record the damage information at each damaged node. The damage index contains the node number, the ply number, and the list of damage criteria that have become activated. Fibers, matrices, and interfaces are each assigned their own damage index to record the corresponding damage information. When a new failure occurs in a fiber, matrix, or interface, its damage index is updated. The properties of fibers, matrices and interfaces are degraded according to their damage index. For example, if a fiber is damaged due to longitudinal tensile failure criteria, its corresponding modulus (E_{11}) is degraded to almost zero.

If there is no damage after a load increment, the structure is considered to be in equilibrium and an additional load increment is applied to start the next analysis cycle. At each cycle, the process of checking the failure criteria, updating the finite element mesh, and updating the material properties is repeated with possible damage growth and propagation. Consecutive analysis cycles are continued until structural collapse is simulated.

In order to evaluate the composite fracture toughness, computation of a damage energy release rate (DERR) during progressive fracture is needed. DERR is defined as the ratio of incremental damage energy to the corresponding incremental damage volume that is generated,

$$DamageEnergy = \sum_i \sum_j \left(0.5 S_{F_j}^2 / E_{F_j}\right) V_{F_i} + \sum_i \sum_j \left(0.5 S_{M_j}^2 / E_{M_j}\right) V_{M_i} + \sum_i \sum_j \left(0.5 S_{I_j}^2 / E_{I_j}\right) V_{I_i}$$

Where

S_{Fj} is the fiber strength, j can be 11, 22, 33, 12, 23, 13.

E_{Fj} is the fiber modulus, j can be 11, 22, 33, 12, 23, 13.

V_{Fj} is the volume corresponding to the failed fiber.

S_{Mj} is the matrix strength, j can be 11, 22, 33, 12, 23, 13.

E_{Mj} is the matrix modulus, j can be 11, 22, 33, 12, 23, 13.

V_{Mi} is the volume corresponding to the failed matrix.

S_{Ij} is the interface strength, j can be 11, 22, 33, 12, 23, 13.

S_{Ij} is the interface modulus, j can be 11, 22, 33, 12, 23, 13.

V_{Ij} is the volume corresponding to the failed interface.

The damage energy release rate is defined as:

$$\text{DERR} = \text{Damage Energy} / \text{Damage Volume}$$

7.5 Examples and Discussion

In order to demonstrate the capability to simulate progressive fracture of ceramic matrix composites, seven NICALON/1723 CMC specimens tested by Coker and Ashbaugh (1992) were simulated. These test specimens were cut from two composite panels, 88C23 and 89C03, as described by Coker and Ashbaugh (1992). The composite was cross-plied with a $[(0/90)_3]_S$ lay-up. The specimen specifications are defined in figure 7.4 and the dimensions for the specimen geometry are presented in table 7.1. The fiber volume fractions for these specimens depended on the size and location of the sample area, and varied from 42 to 48 percent. The average fiber volume fraction of 45% was taken as the fiber volume fraction for simulations in this chapter. The properties for fibers, matrices, and interfaces are shown in tables 7.2, 7.3, and 7.4. The thickness of interface is assumed to be 2 percent of fiber diameter.

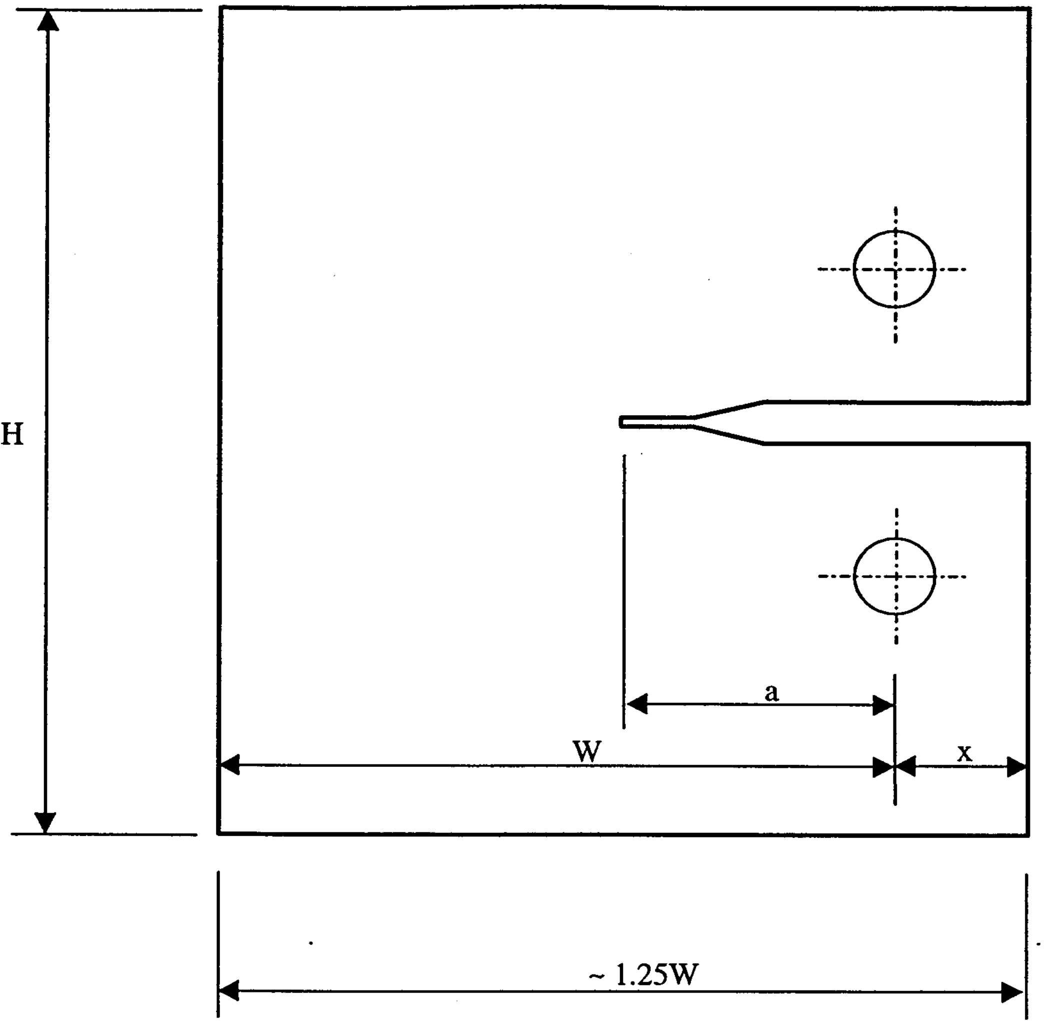

B: Thickness
W: Distance between load line and back face
H: Half height of specimen
a: Distance between load line and notch tip
x: Distance between load line and front face

Figure 7.4 Definition of Specimen Dimensions

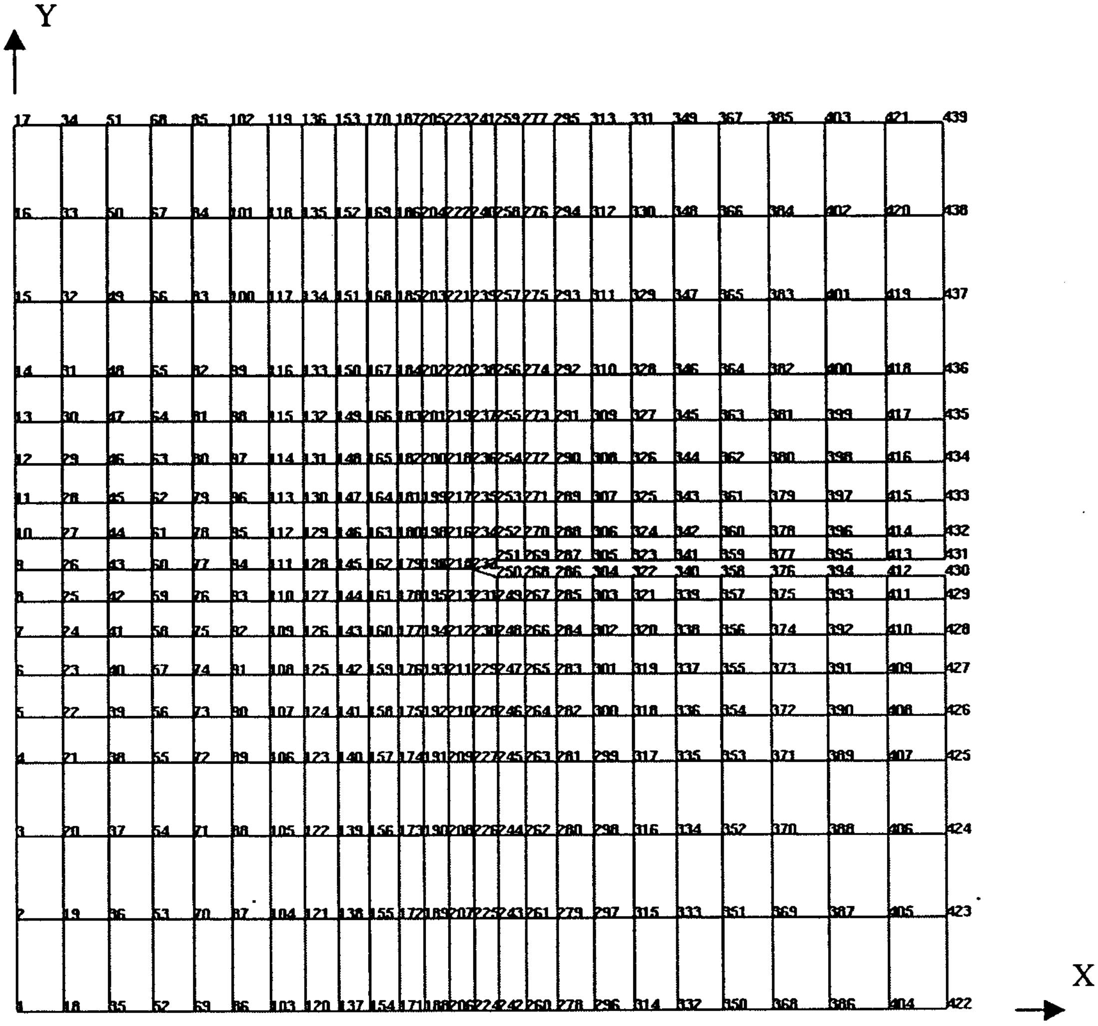

Figure 7.5 Finite Element Model

Table 7.1 Specimen Dimensions

Specimen No.	B (mm)	W (mm)	H (mm)	X (mm)	a (mm)
89C03-2	3.12	19.97	11.96	5.14	10.43
89C03-4	3.03	19.96	11.97	5.30	10.39
89C03-5	3.08	20.04	11.94	5.09	9.96
89C03-7	3.14	20.17	11.95	4.95	10.25
89C03-8	2.96	19.81	12.03	5.26	9.91
89C03-10	3.10	40.03	23.95	10.04	19.86
88C23-7	2.57	40.06	23.92	10.11	19.95

Table 7.2 NICALON fiber properties

Normal modulus (11)	2.900E+07 (psi)
Normal modulus (22)	2.900E+07 (psi)
Poisson's ratio (12)	0.300
Poisson's ratio (23)	0.300
Shear modulus (12)	1.120E+07 (psi)
Shear modulus (23)	1.120E+07 (psi)
Thermal Expansion Coefficient (11)	0.210E-05 (in/in/F)
Thermal Expansion Coefficient (22)	0.230E-05 (in/in/F)
Thermal conductivity (11)	0.208E+01 (BTU/hour/F/in)
Thermal conductivity (22)	0.340E+00 (BTU/hour/F/in)
Heat capacity	0.246E+00 (BTU/lb)
Tension strength (11)	0.350E+06 (psi)
Compression strength (11)	0.350E+06 (psi)
Tension strength (22)	0.350E+06 (psi)
Compression strength (22)	0.350E+06 (psi)
Torsion strength (12)	0.240E+06 (psi)
Torsion strength (23)	0.240E+06 (psi)

Table 7.3 1723 Glass-Matrix properties

Normal modulus	0.127E+08 (psi)
Poisson's ratio	0.220
Thermal Expansion Coefficient	0.240E-05 (in/in/F)
Thermal conductivity	1.167 (BTU/hour/F/in)
Heat capacity	0.1563 (BTU/lb)
Tension strength	10000.0 (psi)
Compression strength	15000.0 (psi)
Shear strength	8000 (psi)

Table 7.4 Interface properties

Normal modulus	1.590E+06 (psi)
Poisson's ratio	0.150
Thermal Expansion Coefficient	0.240E-05 (in/in/F)
Thermal conductivity	1.20 (BTU/hour/F/in)
Heat capacity	0.120 (BTU/lb)
Tension strength	0.800E+04 (psi)
Compression strength	0.145E+05 (psi)
Shear strength	0.800E+04 (psi)

A computational model of the specimen contains 439 nodes and 384 elements as shown in Figure 7-5. The pin holes were not modeled in the finite element representation of the specimen to enable nodal support and loading. The finite element model was configured to have a node point at the center of each pin hole. One of the load points (node 371) was restrained in all degrees of freedom except for θ_Z. The other load point (node 382) was restrained only in D_X, D_Z, θ_X, θ_Y directions, but allowed motion in Y direction and rotation about the Z-axis. A concentrated tensile load was applied at node 382 in the Y direction. The load was increased gradually.

Since all the specimens had similar fracture propagation characteristics, only one specimen, 89C03-10, is discussed in detail here. For specimen 89C03-10, the load started from 44N (10lb.). When the load was under 262N (59 lb.), there was no damage in the specimen. As the load increased to 262N (59lb.), the matrix in ply 4 started to fracture at the notch tip (node 179) due to transverse tension. With the additional increase of the loading, matrix fractures expanded to other plies. When the load increased to 333N (75lb.), fibers in plies 1,2,4,6,7,9,10 at node 179 were damaged due to longitudinal compressive failures. When the load increased to 475N (107 lb.), damage expanded to adjacent nodes, 162, 178, 179, 180. When the load increased to 853N (192 lb.), damage propagated to nodes 127 - 129, 143 - 147, 160 - 164, 177 - 181. When the load increased to 1044N (235lb.), nodes 196 and 197 were completely fractured, and partial-thickness damage was propagated to 54 nodes. When the load increased to 1471N (331lb.), damage expanded to 82 nodes, but still only two nodes, 196 and 197, were completely fractured. The 331 lb. load was the maximum equilibrium load. After this load, the specimen entered an unstable fracture propagation stage. The load could not be increased above 331 lbs without fracturing the specimen. When the load was increased to 1475 N (332 lbs.), the specimen broke into two pieces. Figure 7-6 shows the finite element model immediately before the structural fracture of this specimen. Figure 7.7 shows damage energy release rates with loading. After damage initiation, low points in the DERR indicate reduced structural resistance against damage propagation. On the other hand, high points in the DERR correspond to structural resistance stages against damage progression. Figure 7.7 indicates that the specimen demonstrates significant resistance to damage initiation at approximately 0.3 kN and also resists damage propagation at a load of 1.3 kN. This resistance is confirmed by figure 7.9 where damage progression rate is smaller at this load. Figure 7.8 shows the total damage energy release rates. The total DERR is defined as the ratio of the sum of all damage energies to the total damage volume, accumulated from damage initiation to the simulated load level. The total DERR presents a smoother overall picture of structural fracture resistance characteristics of a specimen. Figure 7.9 shows the percent damage volume versus loading. A steep increase in the damage level indicates the occurrence of critical damage processes.

Table 7.5 shows peak loads for both test and simulation. The test results were provided by Coker et al (1992). From Table 7.5, it can be seen that simulation results agree with test results very well except for specimens 89C03-7 and 89C03-8. From table 7.1, it can be seen that the geometry and size of these specimens are close to those of specimens 89C03-2, 89C03-4, and 89C03-5. Therefore it seems the peak loads for these specimens should also be close as the simulation shows. Test results for specimen 89C03-7 and 89C03-8 give peak loads that seem too low. This may be explained as the scattering of test data. Compared to PMC materials, the properties and peak load of continuous fiber reinforced CMC structures are more difficult to predict since CMC materials behave in a brittle fashion that increases the uncertainties of the failure load levels. Test results for CMC structures usually show more scattering than those of PMC structures. Small variations in the fiber and matrix constituent proprieties may cause a significant change in the structural fracture load. Therefore, more accurate representations of the composite constituent materials are required for CMC micromechanics analysis.

Figures 7.10 through 7.16 show load-displacement relationships for the seven specimens. The displacements shown in these figures are the crack mouth opening displacements (CMOD). It should be noted that, simulations are load-controlled, whereas experimental results are from displacement-controlled tests. For the load-controlled simulations, the load is increased gradually until the specimen is completely failed. During a load controlled simulation there is no unloading process that is taken into account. Therefore, after the load reaches its peak value, no additional load can be applied to the specimen and the specimen fractures or collapses very quickly. However, during a displacement-controlled test, the displacement increases gradually instead of the load. When the specimen reaches its maximum strength, the load also reaches its maximum value-or the peak load. After the peak load, global structural stiffness degrades significantly. Accordingly, the load which can be measured as a reaction under the imposed displacement is decreased. The unloading process after the peak load can be plotted in a load-displacement relationship for a displacement controlled test.

Table 7.5 Peak Loads

Specimen	Test peak loads (KN)	Simulation peak loads (KN)	Relative Error (%)
89C03-2	0.799	0.813	1.7
89C03-4	0.822	0.800	2.6
89C03-5	0.865	0.892	3.1
89C03-7	0.631	0.862	36.6
89C03-8	0.741	0.866	16.8
89C03-10	1.226	1.191	2.8
88C23-7	1.457	1.471	1.0

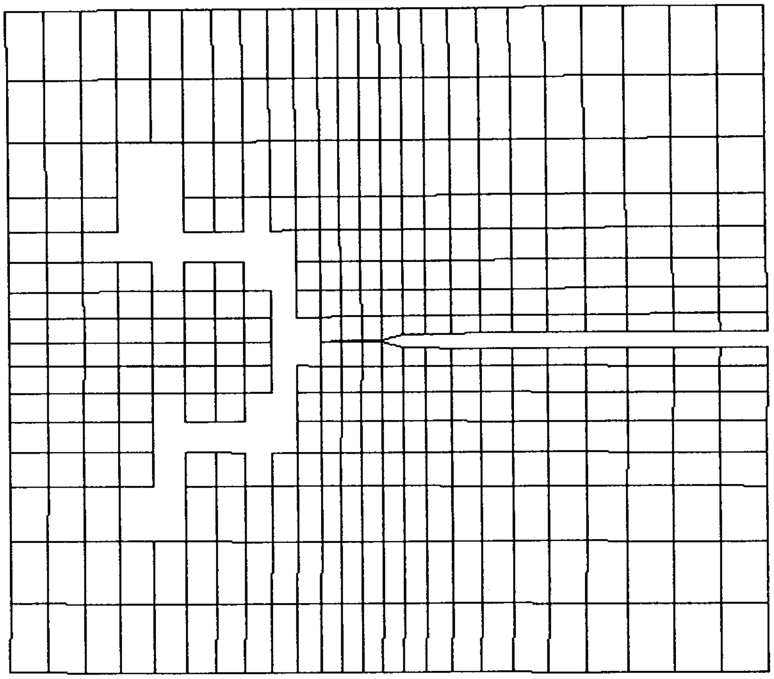

Figure 7.6 Finite Element Model of Specimen C03-10 at Collapse

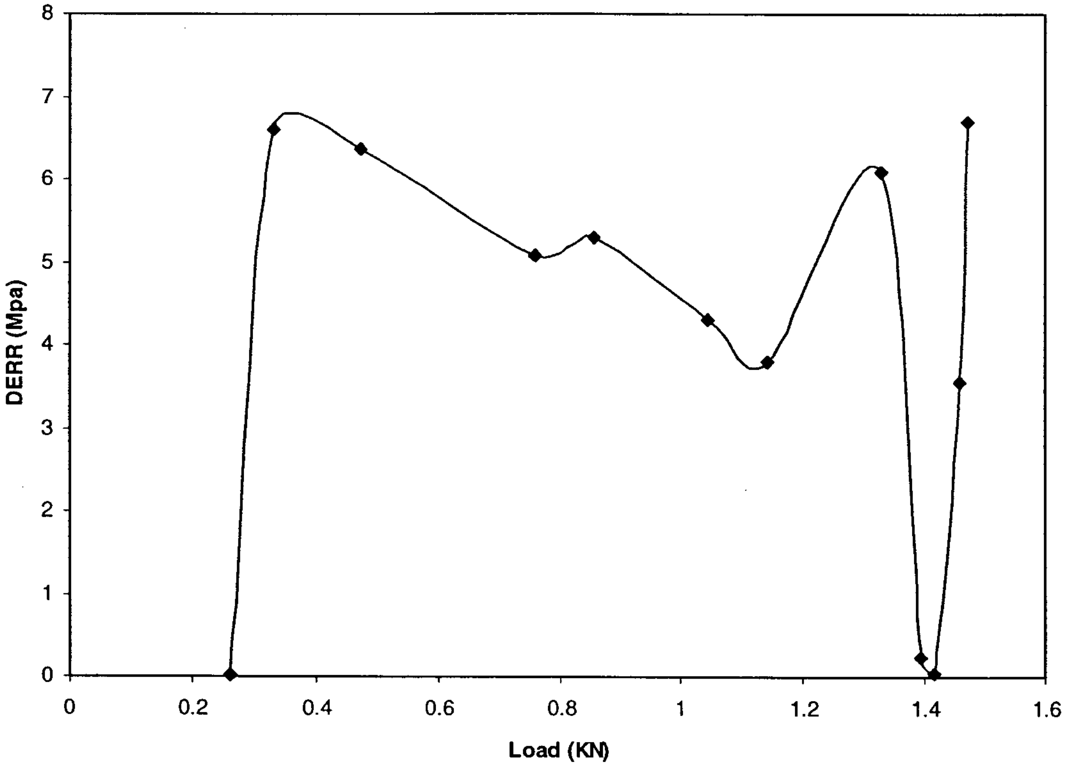

Figure 7.7 Damage Energy Release Rate with Loading for Specimen 89C03-10

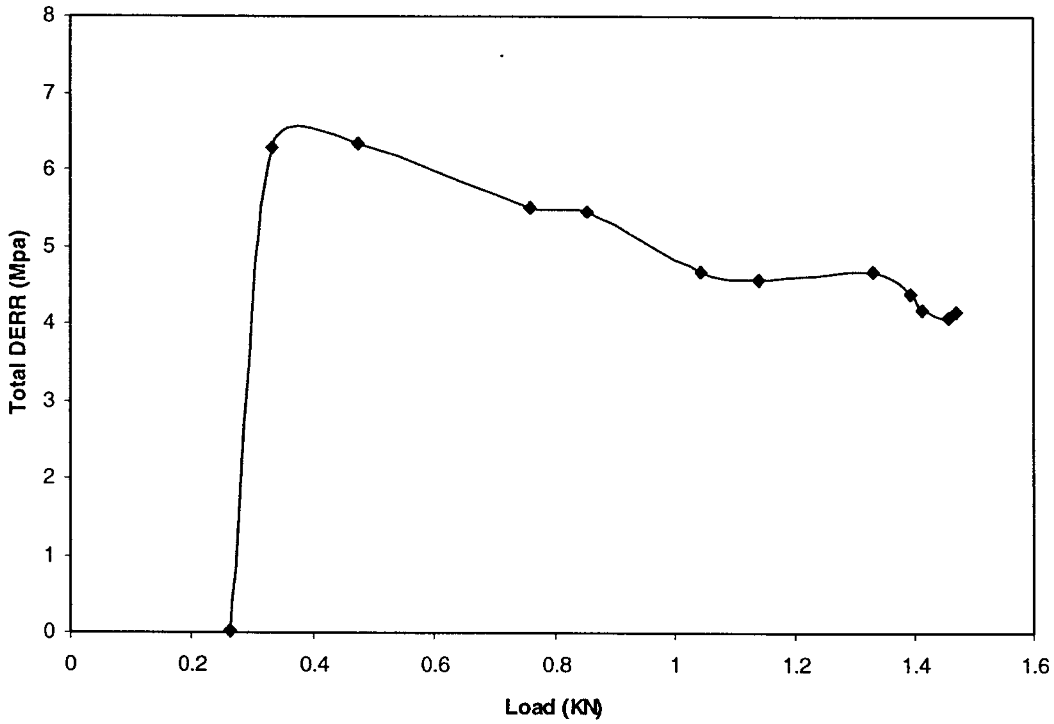

Figure 7.8 Total Damage Energy Release Rate with Loading for Specimen 89C03-10

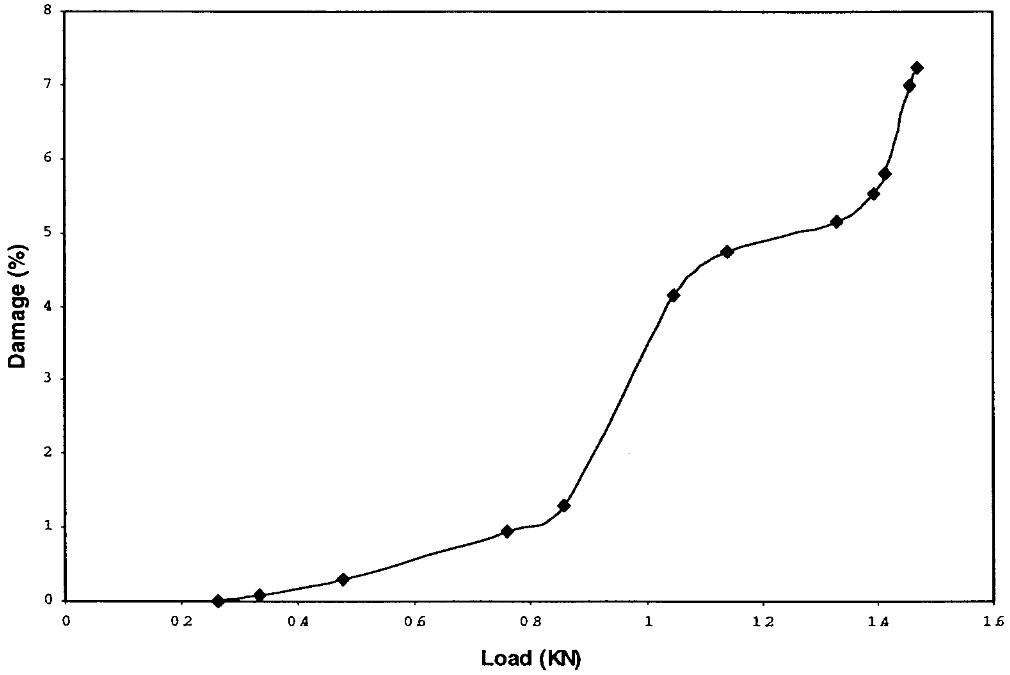

Figure 7.9 Damage Propagation with Load for Specimen 89C03-10

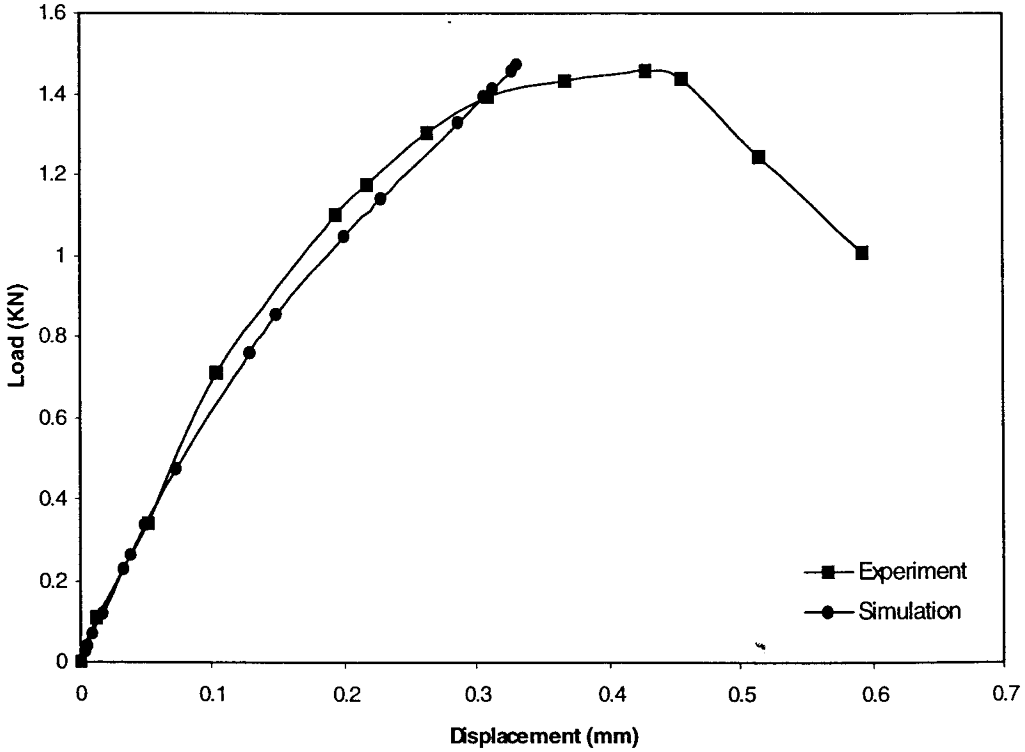

Figure 7.10 Load Displacement Relationship of Specimen 89C03-10

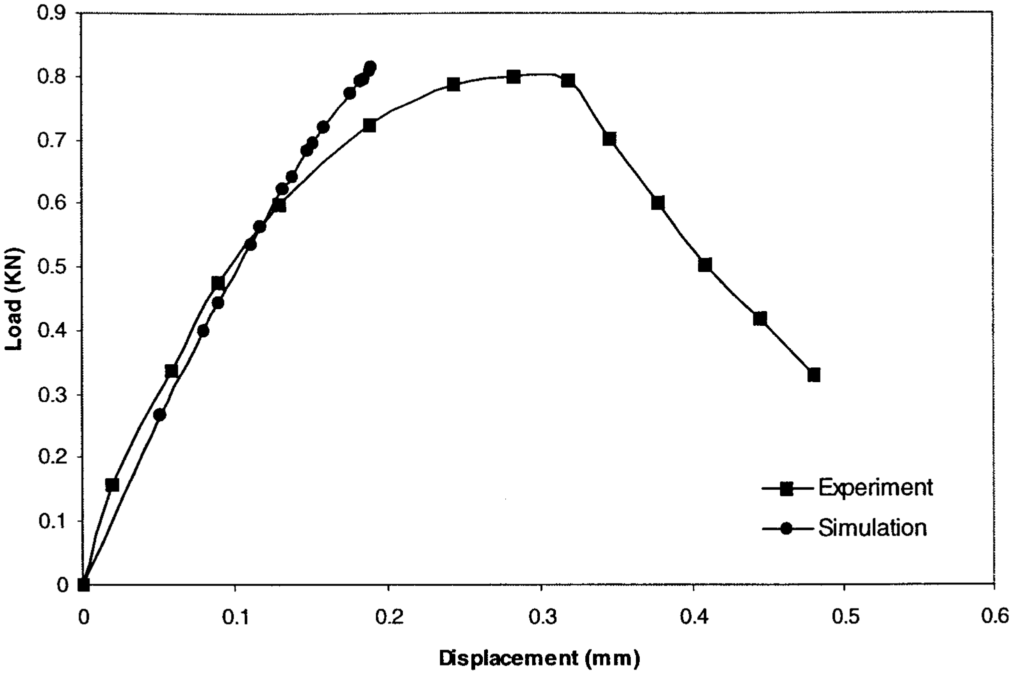

Figure 7.11 Load Displacement Relationship of Specimen 89C03-2

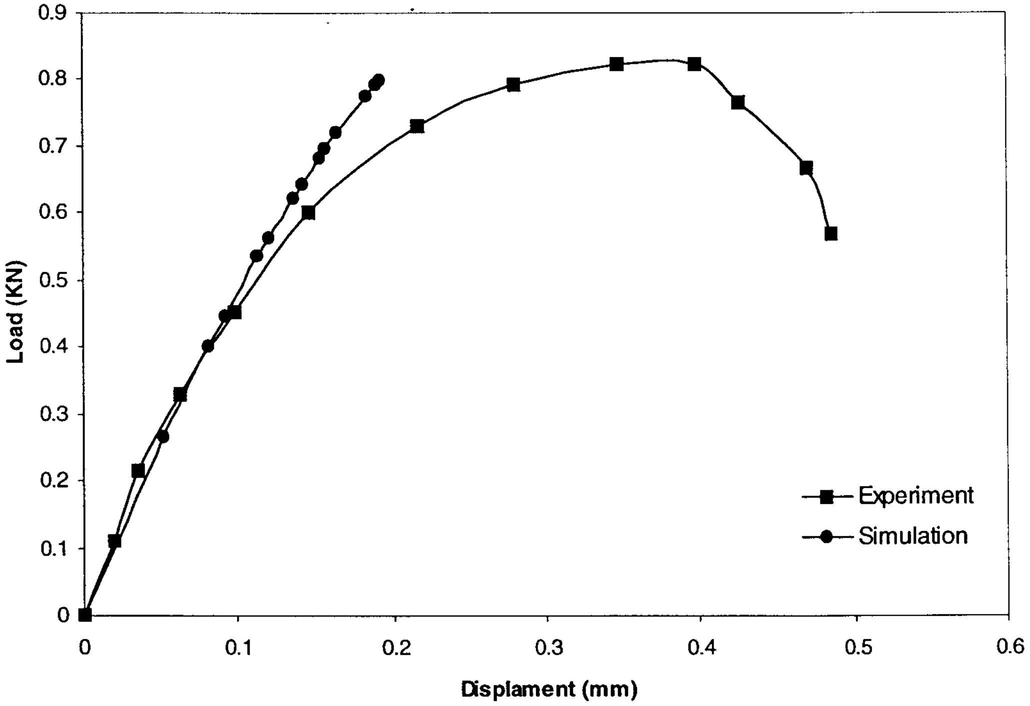

Figure 7.12 Load Displacement Relationship of Specimen 89C03-4

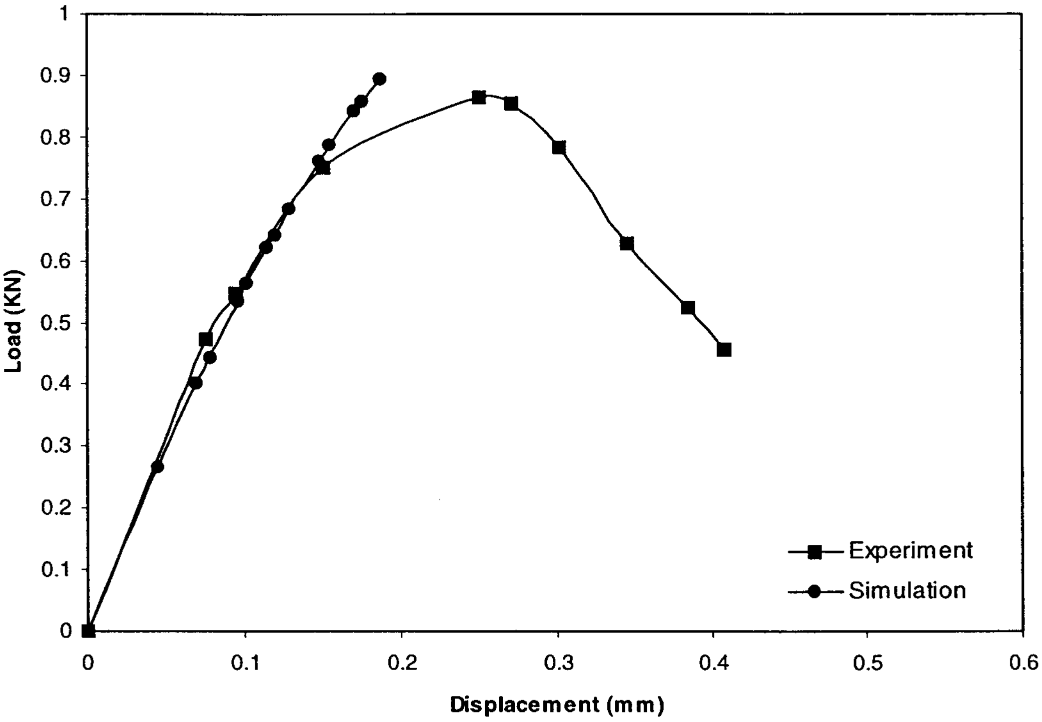

Figure 7.13 Load Displacement Relationship of Specimen 89C03-5

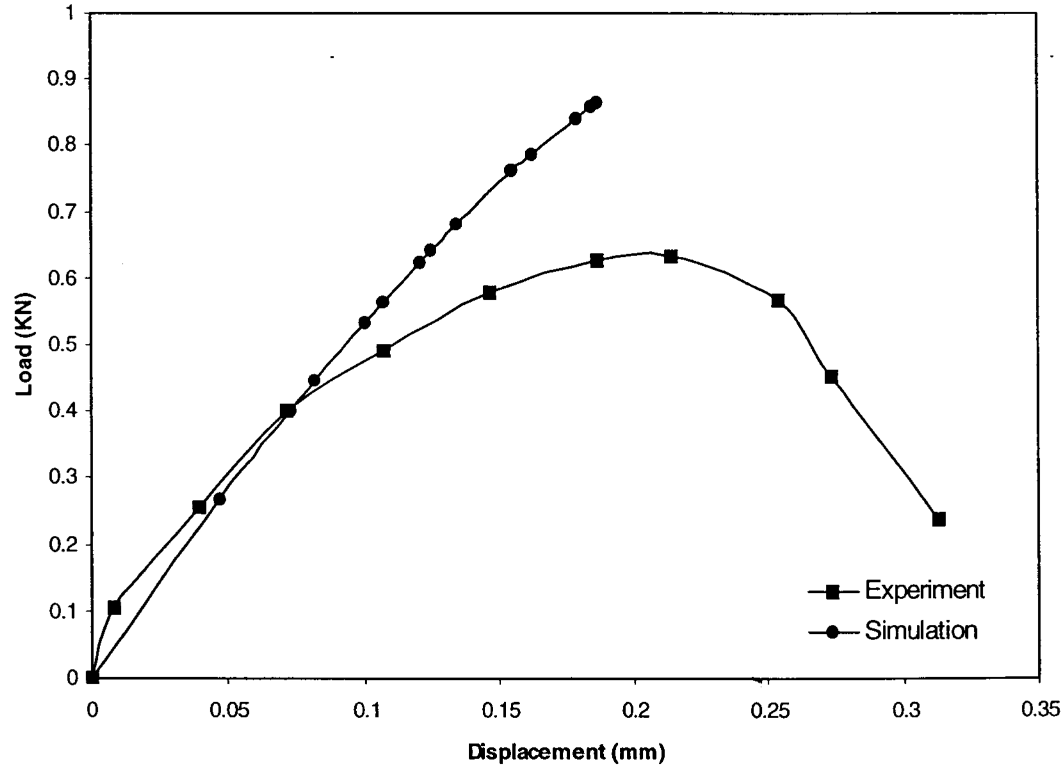

Figure 7.14 Load Displacement Relationship of Specimen 89C03-7

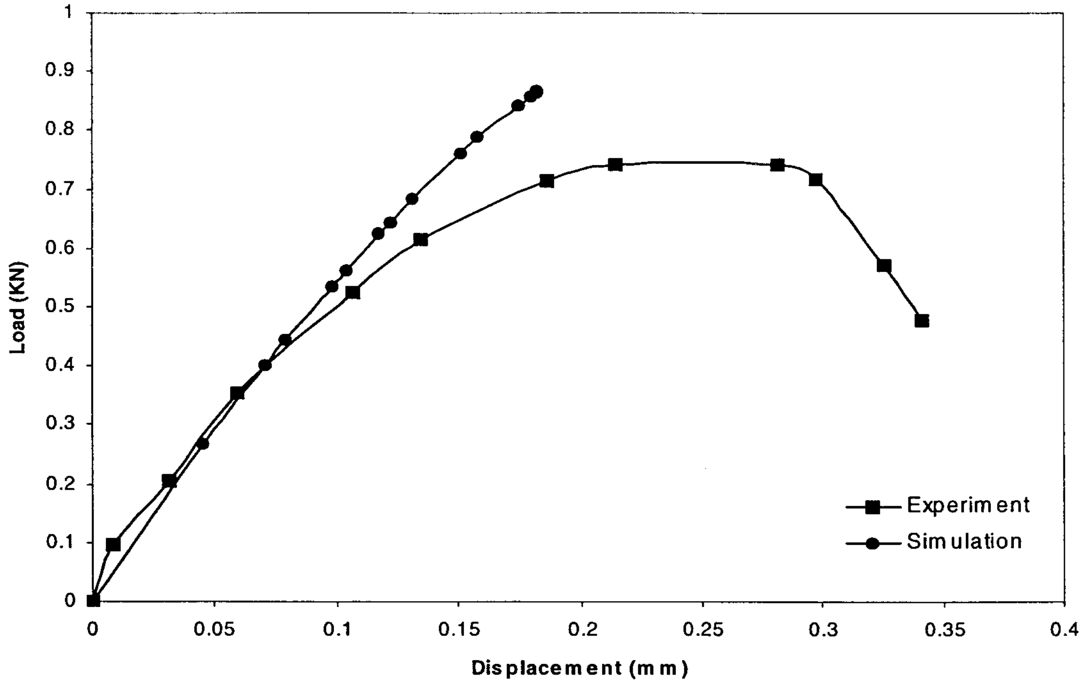

Figure 7.15 Load Displacement Relationship of Specimen 89C03-8

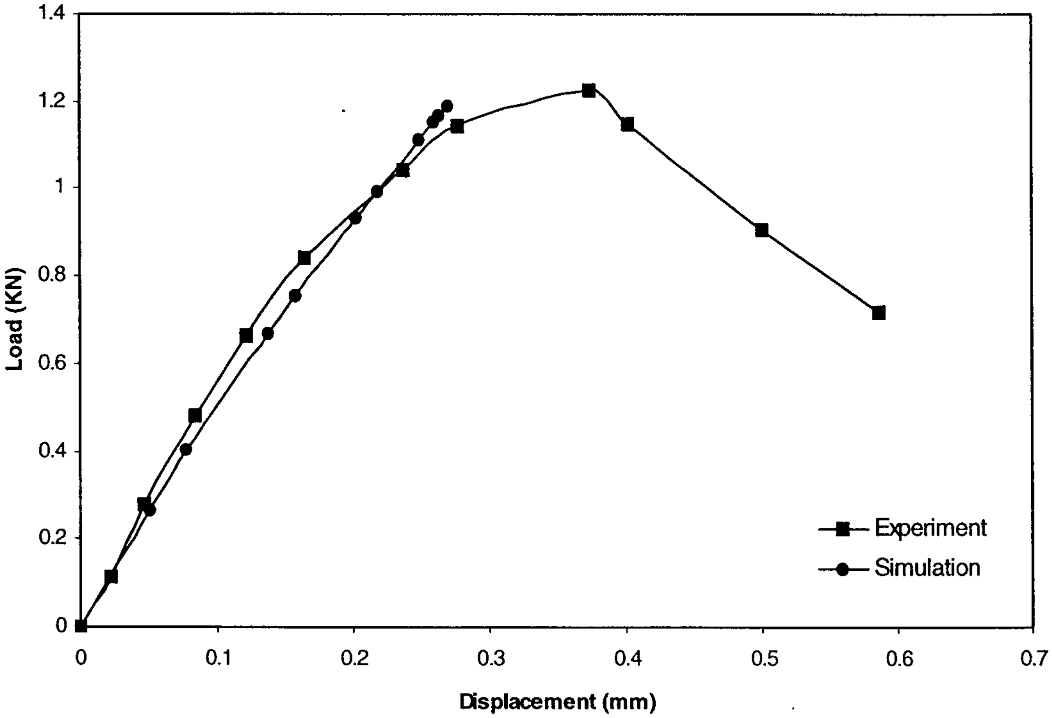

Figure 7.16 Load Displacement Relationship of Specimen 89C23-7

7.6 Conclusion

The significant results from this investigation in which computational simulation was used to evaluate damage growth and propagation to fracture for SiC/1723 ceramic matrix composite specimens are as follows:

1. Computational simulation, with the use of established composite mechanics and finite element modules, can be used to predict the influence of an existing notch, as well as loading, on the progressive fracture of ceramic matrix fiber composite specimens.
2. Computational simulation adequately tracks the damage growth and subsequent propagation to fracture for composite compact tension specimens.
3. Computational simulation can be used prior to testing to identify locations and modes of composite damage that need be monitored by proper instrumentation and inspection of the specimen during a laboratory experiment.
4. Interpretation of experimental data can be facilitated significantly by detailed results from a computational simulation.
5. Computational simulation provides detailed information on damage initiation and progression mechanisms, as well as identifying sensitive material parameters affecting structural fracture.
6. The demonstrated procedure is flexible and applicable to all types of constituent materials, structural geometry, and loading. Hybrid composite structures composites containing homogeneous materials such as metallic layers, as well as binary composites can be simulated.

7. Fracture toughness parameters such as the structural fracture load are identifiable for any specimen or structure by the demonstrated method.

8. Computational simulation represents a new global approach that may be used for progressive damage and fracture assessment in design investigations.

Chapter 8

Conclusion

Predictions of damage growth, and propagation to fracture are needed to evaluate damage tolerance, safety, and reliability of composite structures. Damage stability is influenced by constituent material properties and global factors, such as structural geometry and boundary conditions. The interaction of these factors, further complicated by the numerous possibilities of material combinations, composite geometry, fiber orientations, and loading conditions, renders the assessment of composite damage progression very complex. This complexity makes it very expensive and time consuming to identify and isolate all significant parameters from tests. Computerized simulation can reduce experimental testing requirements and shorten the design time dramatically. This research provided a computational tool for the purpose of progressive fracture and damage tolerance assessment for three-dimensionally reinforced fiber composite structures. The demonstrated, and verified computer software code was developed by enhancing an existing software code, CODSTRAN, with mathematical models and associated software codes that provide the capability to predict the effects of mechanical and thermal loads for the three dimensional polymer/ceramic matrix composite structures. The tasks carried out to accomplish this effort were as follows:

1. A mathematical model and associated software code were developed to evaluate elastic properties and stress limits of three dimensionally reinforced fiber composites.

2. A mathematical model and associated software code were developed to computationally simulate thermo-mechanical loading of three-dimensional woven composite structures.
3. A mathematical model and associated software code were developed to predict damage initiation, propagation, and final failure under mechanical/ thermal loads for composite structures.
4. A mathematical model and associated software code were developed to predict material properties (strength, modulus) degradation relative to service conditions.
5. The developed software simulation results were compared with existing experimental test results to validate evaluation of durability and robustness of the computational approach for three dimensionally reinforced fiber composites.

A significant feature of this research is that it takes into account simulation of crack propagation in 3D polymer/ceramic matrix materials. This can not be accomplished by the use of conventional FEM analysis and laminate theory since classical laminate theory does not consider through the thickness aspects of out-of-plane fiber reinforcements in composite materials, and FEM analysis does not consider degradation of material properties under loading. Further work can be carried out to improve and enhance the current research in the following areas:

1. Progressive damage and fracture of a composite structure subjected to cyclic loading.
2. Prediction of property degradation for composite structures due to thermal loading.
3. Prediction of creep rapture of composite structures.
4. Probabilistic simulation of fracture to quantify reliability of composite structures.

Appendix A: Constituent Material Properties

The following properties were used in the composite material databank to represent the fiber and matrix constituents:

ASW4 Graphite Fiber Properties:
Number of fibers per end = *10000*
Fiber diameter = 0*.00762 mm (0.300E-3 in)*
Fiber Density = *4.04E-7 Kg/m^3 (0.063 lb/in^3)*
Longitudinal normal modulus = *235 GPa (34.08E+6 psi)*
Transverse normal modulus = *17.0 GPa (2.47E+6 psi)*
Poisson's ratio (μ_{12}) = *0.25*
Poisson's ratio (μ_{23}) = *0.27*
Shear modulus (G_{12}) = *55.1 GPa (7.98E+6 psi)*
Shear modulus (G_{23}) = *6.90 GPa (1.00E+6 psi)*
Longitudinal thermal expansion coefficient = *-1.0E-6/°C (-0.55E-6/°F)*
Transverse thermal expansion coefficient = *1.0E-5/°C (0.56E-5/°F)*
Longitudinal heat conductivity = 0*.302 J-m/hr/m^2/°C (4.03 BTU-in/hr/in^2/°F)*
Transverse heat conductivity = *0.0302 J-m/hr/m^2/°C (0.403 BTU-in/hr/in^2/°F)*
Heat capacity = 712 *J/Kg/°C (0.17 BTU/lb/°F)*
Tensile strength = *3,723 MPa (540 ksi)*
Compressive strength = *3,351 MPa (486 ksi)*

SGLW Glass Fiber Properties:
Number of fibers per end = *204*
Fiber diameter = 0*.00914 mm (0.360E-3 in)*
Fiber Density = *5.77E-7 Kg/m^3 (0.090 lb/in^3)*
Longitudinal normal modulus = *84.8 GPa (12.3E+6 psi)*
Transverse normal modulus = *84.8 GPa (12.3E+6 psi)*

Poisson's ratio $(\mu_{12}) = 0.22$

Poisson's ratio $(\mu_{23}) = 0.22$

Shear modulus $(G_{12}) = 34.8$ *GPa (5.04E+6 psi)*

Shear modulus $(G_{23}) = 34.8$*GPa (5.04E+6 psi)*

Longitudinal thermal expansion coefficient = 0.*504E-5/°C (0.280E-5/°F)*

Transverse thermal expansion coefficient = 0.*504E-5/°C (0.280E-5/°F)*

Longitudinal heat conductivity = *3.90E-3 J-m/hr/*m^2*/°C (5.208E-2 BTU-in/hr/*in^2*/°F)*

Transverse heat conductivity = *3.90E-3 J-m/hr/*m^2*/°C (5.208E-2 BTU-in/hr/*in^2*/°F)*

Heat capacity = *712 J/Kg/°C (0.17 BTU/lb/°F)*

Tensile strength = *2482 MPa (360 ksi)*

Compressive strength = *2069 MPa (300 ksi)*

Dow Tactix 138 Epoxy resin with H41 hardener Matrix Properties:

Matrix density = *3.35E-7 Kg/*m^3 *(0.0450 lb/*in^3*)*
Normal modulus = *2.99 GPa (435 ksi)*
Poisson's ratio = *0.300*
Coefficient of thermal expansion = *0.72E-4/°C (0.40E-4/°F)*
Heat conductivity = *8.681E-3 BTU-in/hr/*in^2*/°F*
Heat capacity = 0.*25 BTU/lb/°F*
Tensile strength = *85.0 MPa (12.3 ksi)*
Compressive strength = *423 MPa (61.3 ksi)*
Shear strength = *147 MPa (8.17 ksi)*
Allowable tensile strain = *0.02*
Allowable compressive strain = *0.05*
Allowable shear strain = 0.*04*
Allowable torsional strain = 0.*04*
Void conductivity = *16.8 J-m/hr/*m^2*/°C (0.225 BTU-in/hr/*in^2*/°F)*
Glass transition temperature = *216°C (420°F)*

Appendix B: Comparison of Composite Properties Computed by the 3-D Composite Mechanics (3D-CM) with Cox (1995) and Experimental Data

The following properties are computed by the 3-D Composite Mechanics (3D-CM):

Exx= Elastic modulus in stuffer direction
Eyy= Elastic modulus in filler direction
Ezz= Elastic modulus in normal direction
Gyz= Shear modulus in the filler-normal plane
Gzx= Shear modulus in the stuffer-normal plane
Gxy= Shear modulus in the stuffer-filler plane
NUxy= Poisson's ratio in the stuffer-filler plane
NUyz= Poisson's ratio in the filler-normal plane
NUxz= Poisson's ratio in the stuffer-normal plane
SWxxTf= Tensile strength in the stuffer direction based on fiber stress
SWxxTm= Tensile strength in the stuffer direction based on matrix stress
SWxxCf= Compressive strength in the stuffer direction based on fiber stress
SWxxCm= Compressive strength in the stuffer direction based on matrix stress
SWyyTf= Tensile strength in the filler direction based on fiber stress
SWyyTm= Tensile strength in the filler direction based on matrix stress
SWyyCf= Compressive strength in the filler direction based on fiber stress
SWyyCm= Compressive strength in the filler direction based on matrix stress
SWzzTf= Tensile strength in the normal direction based on fiber stress
SWzzTm= Tensile strength in the normal direction based on matrix stress
SWzzCf= Compressive strength in the normal direction based on fiber stress
SWzzCm= Compressive strength in the normal direction based on matrix stress
SWyzS= Shear strength in the filler-normal plane
SWzxS= Shear strength in the stuffer-normal plane
SWxyS= Shear strength in the stuffer-filler plane

Specimen 1 (LL1) Woven Composite

Property	3D-CM	Cox	Experiment
Exx (GPa)	31.18	36.8	30+/-6
Eyy (GPa)	32.09	38.7	
Ezz (GPa)	8.22	9.0	5.7
Gyz (GPa)	2.2	2.1	
Gzx (GPa)	4.64	6.0	
Gxy (GPa)	2.63	2.3	
Nuxy	0.0468	0.023	0.024
NUyz	0.353	0.216	
NUxz	0.494	0.207	0.22
SWxxTf(GPa)	0.631		
SWxxTm(GPa)	0.0558		
SWxxCf (GPa)	0.5679		
SWxxCm(GPa)	0.1954		
SWyyTf (GPa)	0.5435		
SWyyTm(GPa)	0.3959		
SWyyCf (GPa)	0.4892		
SWyyCm(GPa)	0.1973		
SWzzTf (GPa)	0.1284		
SWzzTm(GPa)	0.0821		
SWzzCf(GPa)	0.1156		
SWzzCm(GPa)	0.3259		
SWyzS (GPa)	0.1152		
SWzxS(GPa)	0.2071		
SWxyS (GPa)	0.1208		

Specimen 2 (LL2) Woven Composite

Property	3D-CM	Cox	Experiment
Exx (GPa)	32.79	34.9	28.5
Eyy (GPa)	42.05	47.6	
Ezz (GPa)	8.06	7.0	5.9
Gyz (GPa)	2.44	2.2	
Gzx (GPa)	3.10	3.2	
Gxy (GPa)	2.89	2.4	
NUxy	0.040	0.027	0.11
NUyz	0.376	0.310	
NUxz	0.460	0.457	0.50
SWxxT(GPa)	0.5833		
SWxxT(GPa)	0.0513		
SWxxCf (GPa)	0.5208		
SWxxCm (GPa)	0.2078		
SWyyTf (GPa)	0.7446		
SWyyTm (GPa)	0.3297		
SWyyCf (GPa)	0.6701		
SWyyCm (GPa)	0.1643		
SWzzTf (GPa)	0.0620		
SWzzTm (GPa)	0.0759		
SWzzCf (GPa)	0.0517		
SWzzCm (GPa)	0.3302		
SWyzS (GPa)	0.1102		
SWzxS (GPa)	0.1473		
SWxyS (GPa)	0.1179		

Specimen 3(LT1) Woven Composite

Property	3D-CM	Cox	Experiment
Exx (GPa)	42.21	47.3	27
Eyy (GPa)	52.98	59.5	
Ezz (GPa)	9.27	9.4	8.0
Gyz (GPa)	2.78	2.7	
Gzx (GPa)	4.53	5.6	
Gxy (GPa)	3.38	3.0	
NUxy	0.0325	0.02	0.048
NUyz	0.342	0.243	
NUxz	0.470	0.541	0.375
SWxxTf (GPa)	0.7608		
SWxxTm (GPa)	0.0511		
SWxxCf (GPa)	0.6027		
SWxxCm (GPa)	0.2069		
SWyyTf (GPa)	0.8744		
SWyyTm (GPa)	0.0345		
SWyyCf (GPa)	0.6927		
SWyyCm (GPa)	0.1722		
SWzzTf (GPa)	0.0998		
SWzzTm (GPa)	0.0777		
SWzzCf (GPa)	0.0790		
SWzzCm (GPa)	0.3392		
SWyzS (GPa)	0.1100		
SWzxS (GPa)	0.1751		
SWxyS (GPa)	0.1208		

Specimen 4(LT2) Woven Composite

Property	3D-CM	Cox	Experiment
Exx (GPa)	42.68	43.5	39
Eyy (GPa)	50.56	51.6	
Ezz (GPa)	8.54	7.0	7.9
Gyz (GPa)	2.69	2.4	
Gzx (GPa)	3.15	3.1	
Gxy (GPa)	3.31	2.6	
NUxy	0.036	0.027	0.021
NUyz	0.379	0.325	
NUxz	0.436	0.37	0.37
SWxxTf (GPa)	0.7377		
SWxxTm (GPa)	0.0466		
SWxxCf (GPa)	0.6012		
SWxxCm (GPa)	0.1969		
SWyyTf (GPa)	0.8363		
SWyyTm (GPa)	0.0346		
SWyyCf (GPa)	0.6805		
SWyyCm (GPa)	0.1727		
SWzzTf (GPa)	0.0544		
SWzzTm (GPa)	0.0748		
SWzzCf (GPa)	0.0453		
SWzzCm (GPa)	0.3374		
SWyzS (GPa)	0.1083		
SWzxS (GPa)	0.1426		
SWxyS (GPa)	0.1187		

Specimen 5(L-O) Woven Composite

Property	3D-CM	Cox	Experiment
Exx (GPa)	47.34	51.9	30+/-2
Eyy (GPa)	57.50	63.9	45.5+/-1.5
Ezz (GPa)	13.97	13.7	7.0+/-1
Gyz (GPa)	2.91	2.7	
Gzx (GPa)	2.73	2.8	
Gxy (GPa)	3.51	3.1	
NUxy	0.0446	0.034	0.053
NUyz	0.236	0.183	
NUxz	0.242	0.184	0.49
SWxxTf (GPa)	0.7499		
SWxxTm (GPa)	0.0409		
SWxxCf (GPa)	0.5759		
SWxxCm (GPa)	0.2037		
SWyyTf (GPa)	0.9423		
SWyyTm (GPa)	0.0334		
SWyyCf (GPa)	0.7238		
SWyyCm (GPa)	0.1664		
SWzzTf (GPa)	0.1079		
SWzzTm (GPa)	0.0658		
SWzzCf (GPa)	0.0828		
SWzzCm (GPa)	0.3282		
SWyzS (GPa)	0.1048		
SWzxS (GPa)	0.1040		
SWxyS (GPa)	0.1162		

Specimen 6(HL1) Woven Composite

Property	3D-CM	Cox	Experiment
Exx (GPa)	87.31	91.5	85+/-8
Eyy (GPa)	54.34	56.2	43.8
Ezz (GPa)	12.58	12.1	16+/-2
Gyz (GPa)	4.47	4.1	
Gzx (GPa)	6.75	7.1	
Gxy (GPa)	5.99	5.4	6.2
NUxy	0.0437	0.034	0.061
NUyz	0.324	0.286	
NUxz	0.422	0.456	
SWxxTf (GPa)	1.1430		
SWxxTm (GPa)	0.0357		
SWxxCf (GPa)	0.9021		
SWxxCm (GPa)	0.1462		
SWyyTf (GPa)	0.7848		
SWyyTm (GPa)	0.0486		
SWyyCf (GPa)	0.4919		
SWyyCm (GPa)	0.2424		
SWzzTf (GPa)	0.0842		
SWzzTm (GPa)	0.0789		
SWzzCf (GPa)	0.0528		
SWzzCm (GPa)	0.3618		
SWyzS (GPa)	0.1130		
SWzxS (GPa)	0.1565		
SWxyS (GPa)	0.1264		

Specimen 7(HL2) Woven Composite

Property	3D-CM	Cox	Experiment
Exx (GPa)	75.32	81.2	80
Eyy (GPa)	51.69	55	42.3
Ezz (GPa)	11.21	10.2	14.0
Gyz (GPa)	3.61	3.6	
Gzx (GPa)	5.26	5.3	
Gxy (GPa)	5.16	4.6	5.8
NUxy	0.0439	0.035	0.13
NUyz	0.354	0.298	
NUxz	0.420	0.425	0.45+/-0.05
SWxxTf (GPa)	1.2495		
SWxxTm (GPa)	0.0335		
SWxxCf (GPa)	0.8527		
SWxxCm (GPa)	0.1479		
SWyyTf (GPa)	0.7776		
SWyyTm (GPa)	0.0451		
SWyyCf (GPa)	0.5307		
SWyyCm (GPa)	0.2250		
SWzzTf (GPa)	0.0466		
SWzzTm (GPa)	0.0754		
SWzzCf (GPa)	0.0318		
SWzzCm (GPa)	0.3567		
SWyzS (GPa)	0.1102		
SWzxS (GPa)	0.1364		
SWxyS (GPa)	0.1221		

Specimen 8(HT1) Woven Composite

Property	3D-CM	Cox	Experiment
Exx (GPa)	84.24	88.6	79
Eyy (GPa)	52.48	54.4	42.5
Ezz (GPa)	12.80	12.8	13.8
Gyz (GPa)	3.99	4.0	
Gzx (GPa)	7.12	7.8	
Gxy (GPa)	5.84	5.3	5.6
NUxy	0.0444	0.033	0.054
NUyz	0.316	0.248	
NUxz	0.430	0.486	
SWxxTf (GPa)	1.415		
SWxxTm (GPa)	0.0386		
SWxxCf (GPa)	0.8948		
SWxxCm (GPa)	0.1499		
SWyyTf (GPa)	0.7554		
SWyyTm (GPa)	0.0492		
SWyyCf (GPa)	0.4777		
SWyyCm (GPa)	0.2451		
SWzzTf (GPa)	0.1118		
SWzzTm (GPa)	0.0806		
SWzzCf (GPa)	0.0707		
SWzzCm (GPa)	0.3591		
SWyzS (GPa)	0.1142		
SWzxS (GPa)	0.1724		
SWxyS (GPa)	0.1271		

Specimen 9(HT2) Woven Composite

Property	3D-CM	Cox	Experiment
Exx (GPa)	80.26	85.1	72
Eyy (GPa)	54.91	57.6	45.8
Ezz (GPa)	11.92	11.2	13.9
Gyz (GPa)	3.88	3.9	
Gzx (GPa)	5.98	6.2	
Gxy (GPa)	5.59	5.0	5.7
NUxy	0.0423	0.033	0.097
NUyz	0.337	0.280	
NUxz	0.422	0.443	
SWxxTf (GPa)	1.323		
SWxxTm (GPa)	0.0355		
SWxxCf (GPa)	0.8602		
SWxxCm (GPa)	0.1514		
SWyyTf (GPa)	0.8133		
SWyyTm (GPa)	0.0460		
SWyyCf (GPa)	0.5285		
SWyyCm (GPa)	0.2293		
SWzzTf (GPa)	0.0650		
SWzzTm (GPa)	0.0772		
SWzzCf (GPa)	0.0422		
SWzzCm (GPa)	0.3592		
SWyzS (GPa)	0.1114		
SWzxS (GPa)	0.1462		
SWxyS (GPa)	0.1243		

Specimen 10(HO1) Woven Composite

Property	3D-CM	Cox	Experiment
Exx (GPa)	89.08	93.1	88
Eyy (GPa)	53.71	56.4	39.9
Ezz (GPa)	16.14	17.3	15.4
Gyz (GPa)	3.41	4.1	
Gzx (GPa)	4.12	4.7	
Gxy (GPa)	4.89	5.4	5.0
NUxy	0.0539	0.051	0.055
NUyz	0.230	0.192	
NUxz	0.221	0.190	
SWxxTf (GPa)	1.405		
SWxxTm (GPa)	0.0284		
SWxxCf (GPa)	0.8815		
SWxxCm (GPa)	0.1416		
SWyyTf (GPa)	0.7835		
SWyyTm (GPa)	0.0481		
SWyyCf (GPa)	0.4913		
SWyyCm (GPa)	0.2400		
SWzzTf (GPa)	0.1129		
SWzzTm (GPa)	0.0694		
SWzzCf (GPa)	0.0708		
SWzzCm (GPa)	0.3460		
SWyzS (GPa)	0.1058		
SWzxS (GPa)	0.1049		
SWxyS (GPa)	0.1222		

Specimen 11(HO2) Woven Composite

Property	3D-CM	Cox	Experiment
Exx (GPa)	80.54	83.8	69+/-5
Eyy (GPa)	52.68	55.9	41.6
Ezz (GPa)	17.97	20.4	22.3
Gyz (GPa)	3.30	4.0	
Gzx (GPa)	3.84	4.4	
Gxy (GPa)	4.52	4.9	
NUxy	0.0559	0.052	0.07
NUyz	0.203	0.158	
NUxz	0.196	0.157	
SWxxTf (GPa)	1.2761		
SWxxTm (GPa)	0.0305		
SWxxCf (GPa)	0.8275		
SWxxCm (GPa)	0.1523		
SWyyTf (GPa)	0.7793		
SWyyTm (GPa)	0.0468		
SWyyCf (GPa)	0.5053		
SWyyCm (GPa)	0.2335		
SWzzTf (GPa)	0.1523		
SWzzTm (GPa)	0.0674		
SWzzCf (GPa)	0.0988		
SWzzCm (GPa)	0.3360		
SWyzS (GPa)	0.1057		
SWzxS (GPa)	0.1045		
SWxyS (GPa)	0.1207		

Chapter 9

References

Bhandarkar, S., A. Dasgupta, M. Pecht and D. Barker. 1991. "Non-Linear Thermo-Mechanical Properties of Fabric Reinforced Printed Wiring Boards", Proceedings of the 5th International SAMPE Electronics Conference, Vol. 5, Los Angeles, CA, June 18-20, Society for the Advancement of Material and Process Engineering, pp. 248-257.

Blackketter, D. M., Walrath, D. E. and Hansen, A. C. 1993. "Modeling Damage in a Plain Weave Fabric-Reinforced Composite Materials," Journal of Composites Technology & Research, Vol. 15, No 2, pp136-142.

Bogdanovich, A. E., Pastore, C. M. and Birger, A. B.1993. "Three-Dimensional Deformation and Failure Analysis of Textile Reinforced Composite Structures," Composites Design, A. Miravete, Ed., Madrid: Proceedings of the Ninth International Conference on Composite Materials (ICCM/9).

Byun, J.H., Whitney, T.J., Du, G.W. and Chou, T.W. 1991. "Analytical Characterization of Two-Step Braided Composites," Journal of Composite Materials, Vol. 25, pp1599-1618.

Chamis, C. C., Murthy, P. L. N., and Minnetyan, L. (1996). "Progressive fracture of polymer matrix composite structures.:" Theoretical and Appl. Fracture Mech., 25(1), 1-15.

Chamis, C. C., Murthy, P.L.N. and Minnetyan, L. 1992. "Progressive Fracture of Polymer Matrix Composites Structures: A New Approach," NASA TM-105574, January, pp.22.

Chamis, C.C. (1969) "Failure Criteria for Filamentary Composites,'' Composite Materials Testing and Design: ASTM STP 460, American Society for Testing and Materials, Philadelphia, pp 336-351

Chamis, C.C., and Sinclair, J.H. (1979). "Micromechanics of Intraply Hybrid Composites: Elastic and Thermal Properties," NASA TM-79253

Coker, D., and Ashbough, N.E., "Characterization of Fracture in $[0/90]_{3S}$ SiC/1723 Composites," Report No. WL-TR-91-4119, Materials Directorate, Wright Laboratory, Wright-Patterson AFB, OH, March 1992.

Cox, B.N., and Dadkhah, M.S. 1995. "The Macroscopic Eleasticity of 3D Woven Composites," Journal of Composite Materials, Vol. 29, No 6, pp785-819.

Dadkhah, M.S., Flintoff, J.G., Kniveton, T. and Cox, B.N. 1995. "Simple Models for Triaxially Braided Composites," Composites 26, pp561-577.

Dasgupta, A. and Bhandarkar, S. M. 1994. "Effective Thermomechanical Behavior of Plain-weave Fabric-Reinforced Composites Using Homogenization Theory," Journal of Engineering Materials and Technology, Vol. 116, pp99-105.

Dow, N. F. and V. Ramnath. 1987. "Analysis of Woven Fabrics for Reinforced Composite Materials", NASA CR-178275, April, National Aeronautics and Space Administration, Hampton, VA.

Du, G.W., Chou, T.W. and Popper, P. 1991. "Analysis of Three-Dimensional Textile Preforms for multidirectional reinforcement of Composites," Journal of Material Science, No 26, pp3438-3448.

Florentine, R. "Apparatus for Weaving a Three-Dimensional Article," U.S. Patent 4,312,261, January 26, 1982.

Foye, R. L. 1993. "Approximaating the Stress Field within the Unit Cell of a Fabric Reinforced Composite Using Replacement Elements", NASA CR-191422, Feb., National Aeronautics and Space Administration, Hampton, VA.

Gotsis, P. K., Chamis, C. C., and Minnetyan, L. (1996). "Computational simulation of damage progression of composite thin shells subjected to mechanical loads." Theoretical and Appl. Fracture Mech., 25(2), 211-224.

Hill, R. (1950). The Mathematical Theory of Plasticity, Oxford University Press, Oxford.

Hirai, I., Uchiyama, T., Mizuta Y. and Pilkey, W. 1985. "An Exact Zooming Method," Finite Elements in Analysis and Design, No 1, pp61-69.

Huang, D. and Minnetyan, L., (1998), "Damage Progression in Carbon-Fiber Reinforced Plastic I-Beams," ASCE Journal of Composites for Construction, Vol. 2, No. 1, February, pp. 38-45.

Ishikawa, T. and Chou, T.W. 1983. "Nonlinear Behavior of Woven Fabric Composites," Journal of Composite Materials, 17:Pp399-413.

Jara-Alamonte, C and Knight, C. 1988. "The Specified Boundary Stiffness/Force SBSF Method for Finite Element Subregion Analysis," International Journal for Numerical Methods in Engineering, Vol. 26, pp1567-1578.

Jones, R. M., 1975, Mechanics of Composite Materials, McGraw-Hill Book Co.

Jortner, J. 1986. "A Model for Nonlinear Stress-Strain Behavior of 2D Composites with Brittle Matrices and Wavy Yarns," Advances in Composites Materials and Structures, AMD-Vol. 82, S.S. wang and Y. D. S. Rajapakse, des., Proceedings of the ASME Winter Annual Meeting, Anaheim, CA, Dec. 10-12, New York: The American Society of Mechanical Engineers, pp. 135-146.

Ko, F. 1986. "Tensile Strength and Modulus of a Three-Dimensional Braid Composite", Composite Materials: Testing and Design (Seventh Conference), ASTM STP 893, pp392-403.

Ko, F. K. 1989. "Three-Dimensional Fabrics for Composites", Composite Materials Series, 3, Textile Structural Composites, T.-W. Chou and F. K. Ko, eds., New York: Elsevier, pp. 129-171.

Ko, F. K. and C. M. Pastore. 1985. "Structure and Properties of an Integrated 3-D Fabric for Structural Composites", Recent Advances in Composites in the United States and Japan, ASTM STP 864, J. R. Vinson and M. Taya, eds., Philadelphia: American Society for Testing and Materials, pp. 428-439.

Kostar, T.D. and Chou, T.W. 1994. "Microstructural Design of Advanced Multi-Step Three-Dimensional Braided Preforms," Journal of Composite Materials, Vol. 28, No13. Pp1180-1201.

Kregers, A. F. and Melbardis Y. G. 1978. "Determination of the Deformability of Three-Dimensional Reinforced Composites by the Stiffness Averaging Method," Polymer Mechanics, No. 1 pp3-8.

Kregers, A. F. and Teters G. A. 1979. "Use of Averaging to Determine the Viscoelastic Properties of Spatially Reinforced Composites," Mechanics of Composite Materials, No. 4, pp617-624.

Kregers, A. F., and Melbardis, Y.G. (1978). “Determination of the Deformability of Three-Dimensional Reinforced composite by the Stiffness Averaging Methods,” Polymer Mechanics, No.1 pp3-8.

Kriz, R. D. 1989. "Edge Stresses in Woven Laminates at Low Temperatures," Composite Materials: Fatigue and Fracture, Second Volume, ASTM STP 1012, P.A. Lagace, Ed., American Society for Testing and Materials.

Kriz, R.D.1985. "Influence of Damage on Mechanical Properties of Woven Composites at Low Temperatures", Journal of Composites Technology and Research, 7(2):Pp55-58.

Lekhnitskii, S.G., Theory of Elasticity of an Anisotropic Body, Mir Publishers, Moscow, 1977, p. 42.

Ma, C. L., Yang J.M. and Chou T. W. 1990. "Elastic Stiffness of Three-Dimensional Braided Textile Structural Composites," Composite Materials: Testing and Design (Seventh Conference), ASTM STP 893, pp404-421.

Mao, K. M. and Sun, C. T. 1990. "A Refined Global-Local Finite Element Analysis Method," International Journal for Numerical Methods in Engineering, Vol. 32, pp29-43.

Minnetyan, L. and Murthy, P.L.N. 1992. "Design for Progressive Fracture in Composite Shell Structure," Proceedings of International SAMPE Technical Conference, Toronto, Canada, October 20-22, ppT227-T240.

Minnetyan, L., and Chamis, C. C. 1997. "Progressive fracture of composite cylindrical shells subjected to external pressure." ASTM J. Compos. Technol. and Res., 1 9(2), 65-71.

Minnetyan, L., Chamis, C. C. and Murthy, P.L.N. 1991. "Damage and Fracture in Composite Thin Shells," NASA TM-105289. November.

Minnetyan, L., Chamis, C. C. and Murthy, P.L.N. 1992. "Structural Behavior of Composites with Progressive Fracture," Journal of Reinforced Plastics and Composites, Vol. 11, No 4, pp413-442.

Minnetyan, L., Chamis, C. C. and Murthy, P.L.N. 1992. "Structural Durability of a Composite Pressure Vessel," Journal of Reinforced Plastics and Composites, Vol. 11, No 4, pp1251-1269.

Minnetyan, L., Chamis, C. C. and Murthy, P.L.N. 1992."Structural Durability of a Composite Pressure Vessel," Journal of Reinforced Plastics and Composites, Vol. 11, No 4, pp1251-1269.

Minnetyan, L., Murthy, P.L.N. and Chamis, C. C. 1990. "Composite Structure Global Fracture Toughness via Computational Simulation," Computers & Structures, Vol. 37, No 2, pp175-180.

Minnetyan, L., Murthy, P.L.N. and Chamis, C. C. 1990. "Progression of Damage and Fracture in Composites under Dynamic Loading," NASA TM-103118, April. pp. 16.

Minnetyan, L., Murthy, P.L.N. and Chamis, C. C. 1992. "Progressive Fracture in Composites Subjected to Hygrothermal Environment," International Journal of Damage Mechanics, Vol. 1, No. 1, pp69-70.

Minnetyan, L., Rivers, J. M., Chamis, C. C., and Murthy, P. L. N. 1995. "Discontinuously stiffened composite panel under compressive loading." J. Reinforced Plastics and Compos., 14(1), 85-98.

Minnetyan, L., Rivers. J.M., Chamis, C. C. and Murthy, P.L.N. 1992. "Structural Durability of Stiffened Composite Shells," Proceedings of the 33rd SDM Conference, Dallas, April, pp2879-2886.

Mital, S.K, and Murthy, P.L.N. 1996. “CEMCAN-Ceramic Matrix Composite Analyzer User’s Guide-Version 2.0,” NASA TM 1071187.

Murthy, P.L.N., Chamis, C.C. 1986. “Integrated Composite Analyzer (ICAN): Users and Programmer's Manual,” NASA Technical Paper 2515.

Murthy, P.L.N., and Chamis, C.C.,”Towards the Development of Micromechanics Equations for Ceramic Matrix Composites via Substructuring,” NASA TM-105246, 1992.

Naik, R. A. 1994. "Analysis of Woven and Braided Fabric Reinforced Composites", NASA Contractor Report 194930, June, National Aeronautics and Space Administration, Hampton, VA. Also Presented at the ASTM 12th Symposium on Composite Materials: Testing and Design, Montreal, Canada, May 16-17.

Naik, R. A. 1995. "Failure Analysis of Woven and Braided Fabric Reinforced Composites," Journal of Composite Materials, Vol.29. No.17, pp2334-2363.

Naik, R. A., P. G. Ifju and J. E. Masters. 1994. "Effect of Fiber Architecture Parameters on Deformation Fields and Elastic Moduli of 2-D Braided Composites", Journal of Composite Materials, 28(7):656-681.

Pastore, C. M. and Ko. F. K. 1990. "Modeling of Textile Structural Composites, Part I: Processing-Science Model for Three-Dimensional Braiding," Journal of the Textile Institute, Vol. 81, No 4, pp480-490.

Pastore, C. M. and Gowayed, Y. A. 1994. "A Self-Consistent Fabric Geometry Model: Modification and Application of a Fabric Geometry Model to Predict the Elastic Properties of Textile Composites," Journal of Composites Technology & Research, Vol. 16, No 1, pp32-36.

Pastore, C. M., Bogdanovich, A. E. and Gowayed, Y. A. 1993. "Applications of a Meso-Volume-Based Analysis for Textile Composite Structures," Composite Engineering, Vol.3, No 2, pp181-194.

Pierce, F. T. 1987. "Geometrical Principle Applicable to the Design of Functional Fabrics," Textile Research Journal, Vol.17, No 3, pp123-147.

Stanton, E. L. and Kipp, T.E. 1985. "Nonlinear Mechanics of Two-Dimensional Carbon-carbon Composite Structures and Materials", AIAA Journal, 23(8), pp1278-1284.

Sun, C. T. and Mao. K. M. 1988. "A Global-Local Finite Element Method Suitable for Parallel Computations," Computers and Structures, Vol. 29, pp309-315.

Sun, C. T. and Mao. K. M. 1988. "Elastic-Plastic Crack Analysis Using a Global-Local Approach on a Parallel Computer," Computers and Structures, Vol. 30, pp395-401.

Takayanagi, H., Kemmochi, K., Sembokuya, H., Hojo, M., and Maki, H. 1994. "Shear-lag effect in CFRP I-beams under three-point bending." Experimental Mech., 34(2), 100-107.

Tsai, S. W. 1968. "Strength Theories of Filamentary Structures," in R.T. Schwartz and H.S. Schwartz, Eds., Fundamental Aspects of Fiber Reinforced Plastic Composites, Interscience, New York, Chapter 1.

Vladimir Panc, 1975, Theories of Elastic Plates, Noordhoff International Publishing, Leyden.

Whitcomb, J. D. 1989. "Three-Dimensional Stress Analysis of Plain Weave Composites," NASA TM 101672.

Whitcomb, J. D. 1991. "Iterative Global/Local Finite Element Analysis," Computers & Structures, 40(4).

Whitcomb, J. D. 1994, "Analysis of New Composite Architectutes," NASA Contractor Report 195303.

Whitcomb, J. D. and Woo. K. 1994. "Enhanced Direct Stiffness Method for Finite Element Analysis of Textile Composites," Composite Structures, Vol. 28, pp385-390.

Whitcomb, J., Woo, K. and Gundapaneni, S. 1994. "Macro Finite Element for Analysis of Textile Composites," Journal of Composite Materials, Vol.28, No.7, pp607-618.

Whitney, T.J., and Chou, T.W. 1989. "Modeling of 3-D Angle-Interlock Textile Structural Composites," Journal of Composite Materials, Vol. 23, No6, pp890-911.

Woo, K. and Whitcomb, J. D. 1993. "Macro Finite Element Using Subdomain Integration," Communications of Numerical Methods in Engineering, Vol.9, 937-949.

Woo, K., and Whitcomb, J. 1994. "Global/Local Finite Element Analysis for Textile Composites," Journal of Composite Materials, Vol. 28, No. 14, pp1305-1321.

Woo, K., and Whitcomb, J.D. 1996. "Three-Dimensional Failure Analysis of Plain Weave Textile Composites Using a Global/Local Finite Element Method," Journal of Composite Materials, Vol. 30, No. 9, pp984-1003.

Xu, J., Cox, B.N., McClockton, M.A., and Carter, W.C. 1992, "A Binary Model of Textile Composites: II The Elastic Regime," Acta Metallurgica Materialia, Vol.43, No. 9, pp3511-3524.

Yang, J.M., Ma, C.L. and Chou, T.W. 1986. "Fiber Inclined Model of Three-Dimensional Textile Structural Composites," Journal of Composite Materials, Vol. 20, pp472-484.

Yeh, H.Y. and Chen V. L., 1996. "Experimental Study and Simple Failure Analysis of Stitched J-Stiffened Composite Shear Panels," Journal of Reinforced Plastics and Composites, Vol 15, November 1996. Pp1070-1087

Yoshino, T., Ohtsuka, T. and Noguchi, Y. 1981. "Stress Analysis by Photoelasticity and F.E.M. of plain Woven Glass Fiber Reinforced Plastic Laminates," Composite Materials, K. Kawaata and T. Askaka, Ed., Proceedings of Japan-U.S. Conference, Tokyo.

REPORT DOCUMENTATION PAGE

Form Approved
OMB No. 0704-0188

1. AGENCY USE ONLY (*Leave blank*)	**2. REPORT DATE** October 2005	**3. REPORT TYPE AND DATES COVERED** Final Contractor Report

4. TITLE AND SUBTITLE Computational Simulation of Damage Propagation in Three-Dimensional Woven Composites	**5. FUNDING NUMBERS** WBS–22–066–30–02 NAG3–1101
6. AUTHOR(S) Dade Huang and Levon Minnetyan	
7. PERFORMING ORGANIZATION NAME(S) AND ADDRESS(ES) Clarkson University 8 Clarkson Avenue Potsdam, New York 13699	**8. PERFORMING ORGANIZATION REPORT NUMBER** E–15279
9. SPONSORING/MONITORING AGENCY NAME(S) AND ADDRESS(ES) National Aeronautics and Space Administration Washington, DC 20546–0001	**10. SPONSORING/MONITORING AGENCY REPORT NUMBER** NASA CR—2005–213963

11. SUPPLEMENTARY NOTES

Project Manager, Christos C. Chamis, Research and Technology Directorate, NASA Glenn Research Center, organization code R, 216–433–3252.

12a. DISTRIBUTION/AVAILABILITY STATEMENT Unclassified - Unlimited Subject Category: 24 Available electronically at http://gltrs.grc.nasa.gov This publication is available from the NASA Center for AeroSpace Information, 301–621–0390.	**12b. DISTRIBUTION CODE**

13. ABSTRACT ***(Maximum 200 words)***

Three-dimensional (3D) woven composites have demonstrated multi-directional properties and improved transverse strength, impact resistance, and shear characteristics. The objective of this research is to develop a new model for predicting the elastic constants, hygrothermal effects, thermomechanical response, and stress limits of 3D woven composites; and to develop a computational tool to facilitate the evaluation of 3D woven composite structures with regard to damage tolerance and durability. Fiber orientations of weave and braid patterns are defined with reference to composite structural coordinates. Orthotropic ply properties and stress limits computed via micromechanics are transformed to composite structural coordinates and integrated to obtain the 3D properties. The various stages of degradation, from damage initiation to collapse of structures, in the 3D woven structures are simulated for the first time. Three dimensional woven composite specimens with various woven patterns under different loading conditions, such as tension, compression, bending, and shear are simulated in the validation process of this research. Damage initiation, growth, accumulation, and propagation to fracture are included in these simulations.

14. SUBJECT TERMS Progressive fracture; Structural fracture; Three-dimensional woven composites	**15. NUMBER OF PAGES** 153
	16. PRICE CODE

17. SECURITY CLASSIFICATION OF REPORT Unclassified	**18. SECURITY CLASSIFICATION OF THIS PAGE** Unclassified	**19. SECURITY CLASSIFICATION OF ABSTRACT** Unclassified	**20. LIMITATION OF ABSTRACT**